Quantum Lattice Models from Fusion Categories

Luisa Eck

Balliol College

University of Oxford

A thesis submitted for the degree of

Doctor of Philosophy

Trinity 2025

Acknowledgements

First, I want to thank my supervisor Paul Fendley for his guidance and mentorship. When I started my DPhil, I was intrigued by the colorful diagrams in his topological defects and dualities paper, and we started exploring a particular 1+1d model with such defects. Two years, two papers, and many conversations on fusion categories, spin chains, integrability, and CFT later, those diagrams began to make sense. With his encouragement, I then ventured into 2+1 dimensions. Thanks for giving me the freedom to pursue my own ideas, while also being there to talk whenever I got stuck.

I met Sakura Schäfer-Nameki through the weekly OWSM meetings she organized, which helped make Oxford one of the best places (the best place?) to work on generalized symmetries. I'm grateful for inspiring research discussions and especially for her generous support and advice during my postdoc applications.

My research benefited greatly from discussions with other members of the generalized symmetries community in Oxford, especially Kansei Inamura, Thomas Wasserman, André Henriques, and Steve Simon. I would also like to thank my office mates Riccardo Senese and Saraswat Bhattacharyya for their friendly company and open ear, and the other DPhil students and postdocs of the condensed and soft matter groups for countless coffee breaks, college lunches, and pub trips. Thanks to my former Balliol flatmate Hannah Römer for brightening many days with veggie food, rowing, and formal dinners.

I'm thankful for the financial support from the EPSRC and the Jim and Jane Ramage Scholarship at Balliol College, and for the additional funding from the Theoretical Physics sub-department at Oxford during the final six months.

I was fortunate to be able to travel quite a bit over the last four years, and had many stimulating discussions at conferences, summer schools, and workshops, particularly with Natalia Chepiga, Frank Verstraete, Robert König, Fiona Burnell, and Xie Chen. I also want to thank my undergraduate advisor Sergej Moroz for his support over the years. Many thanks to the Kavli Institute for Theoretical Physics (KITP) for hosting me as a Graduate Fellow in the five months leading up to submitting this thesis, and to the organizers of the Generalized Symmetries program. During my time there, I'm grateful to Dave Aasen for introducing me to Floquet codes, to Dave Penneys for starting a project on symmetry-enriched topological orders with me within an hour of meeting, and to Zhenghan Wang for sparking my interest in 3d CFTs and sustaining it through many engaging discussions.

Beyond academia, I'm especially grateful to my mum Christine Eck for her constant encouragement and belief in me, and for always spoiling me with the most delicious food. Thanks to my sister Katharina Eck for regularly checking in with me even when I'm away, and to her and my dad Thorsten Eck for dragging me into sporty outdoor activities whenever I'm in Munich. Thanks to my grandparents Franz and Traudl Dawidowitsch for watching me grow up (literally), and to Clara Peters, Sara-Viola Kuntz, and Sarah Haiber for their steady friendship.

Finally, I'm very lucky to have my partner Steffen Schneider by my side. Throughout my physics studies, Steffen has always been there to support me, from making numerics more enjoyable and helping with proofreading and typesetting to debating linear algebra problems and lifting my mood with his infectious optimism.

Abstract

Fusion categories offer a systematic framework for constructing quantum lattice models with non-invertible symmetries and dualities. This thesis examines the quantum phases and transitions realized in a specific 1+1d lattice model and develops these ideas further to study 2+1d models with topological order.

After a brief review of fusion categories, anyon chains, and string-nets in Chapter 2, Chapter 3 investigates a model of Rydberg-blockade atoms on the square ladder with at most one excited atom per square. Along an integrable line, it is equivalent to the 1+1d anyon chain built from the $so(3)_2$ fusion category and preserves a non-invertible self-duality symmetry that can be spontaneously broken. A duality mapping to the spin-$\frac{1}{2}$ XXZ chain reveals a critical line governed by the free boson orbifold CFT. A non-invertible remnant of the XXZ chain's $U(1)$ symmetry applies to the full three-parameter space of couplings and distinguishes two different $\mathbb{Z}_3$ ordered phases. Away from integrability, we use perturbation theory and DMRG to explore a rich phase diagram with several density-wave phases separated by critical and first-order transitions.

The second part of this thesis focuses on 2+1d fusion surface models, higher-dimensional extensions of anyon chains built from braided fusion categories. In Chapter 4, we develop systematic generalizations of Kitaev's honeycomb model, which itself can be formulated as a fusion surface model built from the Ising category. These models exhibit categorical 1-form symmetries and have phase diagrams qualitatively similar to Kitaev's, including a weakly coupled chains phase capable of hosting chiral topological order, as demonstrated in a $\mathbb{Z}_3$ symmetric example. Chapter 5 shows that dualities between such models arise by refining the input data with module tensor categories, paralleling the construction of dual 1+1d anyon chains. The resulting 2+1d models support both 0-form and 1-form symmetries and are candidates for realizing symmetry-enriched topological phases. Taken together, these results point towards a broader framework for 2+1d quantum lattice models beyond commuting projectors, with Chapter 6 outlining connections to 3d criticality, quantum scars, and quantum error correction.

Contents

Appendices

1

Introduction

Lattice models underpin much of our theoretical understanding of phases of matter and the transitions between them. A paradigmatic example is the classical Ising model [1, 2], where spins with two possible values (say, up or down) are placed at the sites of a square lattice and interact with their nearest neighbors. At low temperatures, the spins tend to align in one direction, thus modeling ferromagnetic order. In the context of electronic systems, tight-binding models place fermions on a lattice and describe their hopping between adjacent sites, capturing the band structure of crystals.

Because lattice models with discrete degrees of freedom describe systems via finite-dimensional operators – Hamiltonians for quantum models or transfer matrices for classical ones – they are well suited for both analytical and numerical methods. One is often interested in the qualitative behavior of the ground states or low-lying excitations, and how these change under small perturbations of the microscopic parameters. This leads to the notion of a phase: a region in parameter space where the system exhibits qualitatively similar low-energy behavior. Symmetries are usually implemented by local unitary operators that form a group representation and commute with the Hamiltonian or transfer matrix. They constrain the allowed interactions and help organize the phase diagram. For example, the $\mathbb{Z}_2$ spin-flip symmetry of the Ising model is spontaneously broken in the ferromagnetic phase, where it permutes two degenerate ground states, but restored in the paramagnetic phase, which has a unique symmetric ground state.

Many interesting statistical mechanical models admit a larger class of topological defects that commute with the transfer matrix but do not represent a group [3]. The mathematical structure underlying these defects is a fusion category, which comes equipped with a powerful diagrammatic calculus: trivalent graphs encode the fusion of objects and can be evaluated into a complex number invariant under continuous deformations. A prominent example of a topological defect is the Kramers–Wannier duality in the 2d Ising model [4], which relates the low- and high-temperature regimes via a non-invertible mapping that becomes a self-duality at the critical point. The algebra generated by the duality operator and the $\mathbb{Z}_2$ spin-flip symmetry reproduces the fusion rules of the Ising category.

The connection between statistical mechanics, algebraic structures, and graphical calculus became more concrete with the work of Temperley and Lieb [5], who showed that the generators of the transfer matrices in the Potts and six-vertex models satisfy a common algebra, now bearing their name. The Temperley-Lieb algebra also underlies the construction of knot invariants like the Jones polynomial [6–8], and has a graphical presentation in terms of non-intersecting loops [9]. Andrews, Baxter, and Forrester [10] introduced a family of height models whose Boltzmann weights can be expressed in terms of Temperley–Lieb generators as well, and which, in the trigonometric case, implicitly encode the data of the $\mathcal{A}_k$ fusion category.

The trigonometric ABF models, along with the Ising and Potts models [11, 12], have integrable limits whose continuum descriptions are given by rational conformal field theories (CFTs). Both integrability and rational CFTs are deeply connected to braided fusion categories, which provide a consistent diagrammatic calculus for evaluating over- and under-crossings. In rational CFTs, the fusion and braiding of primary fields are governed by modular tensor categories [13], a special class of braided fusion categories with non-degenerate braiding that distinguishes all simple objects. For example, the continuum limit of the critical ABF models is described by a modular tensor category that contains the $\mathcal{A}_k$ fusion category, which is already present in the Boltzmann weights, as a subcategory [3, 13–15]. The topological defects of the lattice model appear as defect lines in the CFT [16, 17]. Meanwhile, the integrability of these models is captured by the Yang–Baxter equation, which imposes a trilinear constraint on the Boltzmann weights and admits a geometric interpretation as the third Reidemeister move—sliding a strand under or over a crossing.

In recent years, 1+1d quantum spin chains built from fusion categories, known as anyon chains, have attracted growing interest [3, 18–22]. Anyon chains can be constructed from any fusion category and can be viewed as the Hamiltonian limit of the corresponding 2d statistical mechanical model. A key example is the family of anyon chains based on the $\mathcal{A}_k$ fusion categories, which arise from the Hamiltonian limit of the associated ABF models. Anyon chains inherit categorical symmetries corresponding to topological defects in the associated 2d classical models. These symmetries are efficiently represented by matrix product operators [23, 24], which are typically non-local and non-invertible. Like conventional symmetries, they constrain the phase diagram by forbidding certain relevant perturbations at criticality and by distinguishing symmetry-breaking patterns in gapped phases. This perspective underlies the “categorical Landau paradigm” [25–28], which seeks to classify both gapped and gapless phases with categorical symmetries using the language of fusion and module categories. Notably, many anyon chains feature constrained Hilbert spaces dictated by the fusion rules of their input category. In some cases, these constraints resemble blockade effects observed in arrays of Rydberg atoms [29–32], which are increasingly recognized as promising platforms for quantum simulation [33, 34].

Fusion categories also appear naturally in the description of 2+1d topological phases, whose ground state degeneracy depends on the topology of the underlying space [35, 36]. The low-energy physics of such topologically ordered phases is given by a topological quantum field theory [37] and the anyonic excitations are mathematically captured by a unitary modular tensor category [38, 39]. Chiral topological orders, which break time-reversal symmetry, have gapless edge modes described by chiral conformal field theories and model the physics of fractional quantum Hall systems [40, 41]. Their gapless edge modes should yield experimentally accessible signatures in conductance measurements, though claims of such signatures in Kitaev candidate materials like α-RuCl$_3$ remain controversial and subject to ongoing debate [42–44].

The intrinsic robustness of topological phases against local perturbations, together with the anyonic statistics of their excitations, makes them highly promising for fault-tolerant quantum computing [45, 46]. The canonical example is Kitaev's toric code [47], a commuting projector model on the square lattice whose anyons are mutually semionic. Building on this, Levin and Wen [48] formulated string-net models defined on trivalent graphs with edge labels drawn from a fusion category. Their commuting projector models capture all non-chiral topological orders, with the anyon content described by the Drinfeld center of the input category. In contrast, finding solvable 2+1d lattice models for chiral topological order remains a challenging problem. Known examples typically require free-fermion constructions, such as Kitaev's honeycomb model [39], rely on coupled-wire constructions with carefully fine-tuned interactions [49], or require infinite-dimensional Hilbert spaces [50].

This thesis approaches the problem from a different angle: using fusion categories as a unifying input to construct tractable lattice models in one and two spatial dimensions. We begin with a 1+1d anyon chain that models a ladder of Rydberg atoms, then build toward 2+1d systems using the fusion surface model construction [51], which extends anyon chains into higher dimensions. These models go beyond commuting-projector Hamiltonians and are capable of realizing chiral and symmetry-enriched topological phases.

The material is organized into six chapters. Following the Introduction, Chapter 2 provides a review of fusion categories and their associated graphical calculus, along with two physical contexts where they naturally arise: 2+1-dimensional Levin-Wen string-net models, which are fixed points for non-chiral topological order, and 1+1-dimensional anyon chains, which come with categorical symmetries and dualities.

Chapter 3 focuses on a specific anyon chain constructed from the $so(3)_2$ fusion category, whose constrained Hilbert space mirrors that of a Rydberg-blockade ladder. We analyze its ordered phases and critical transition using a combination of conformal field theory, perturbation theory, and numerical simulations. Non-invertible symmetries and a duality to the spin-1/2 XXZ chain play a central role in our analysis.

Chapters 4 and 5 form the core of the thesis and discuss phases and symmetries of 2+1d fusion surface models, building on earlier work by Inamura and Ohmori [51]. Chapter 4 discusses fusion surface models built from braided fusion categories, which can be regarded as generalizations of Kitaev's honeycomb model. These models naturally exhibit categorical 1-form symmetries and include a weakly coupled chains phase that can host chiral topological order as we confirm in explicit examples.

Chapter 5 generalizes the framework further by incorporating dualities, understood as gauging of categorical 1-form symmetries. This leads to new dual models that can support independent 0-form symmetries and realize symmetry-enriched topological orders.

Finally, Chapter 6 summarizes the main results and outlines directions for future work, including potential connections to quantum dynamics, quantum error correction, and 3d criticality.

2

Background

Contents

Fusion categories are natural generalizations of finite groups and have many applications in modern quantum many-body physics. A key feature is their diagrammatic calculus that associates topological invariants to trivalent graphs.

In 1+1-dimensional systems, they encode finite global symmetries implemented by topological defects and form the basis for constructing anyon chains—quantum spin chains with constrained Hilbert spaces that are often exactly solvable at special points [3, 18, 21]. Including additional input data in the form of a module category allows one to capture dualities between such chains [23, 24].

In 2+1 dimensions, fusion categories serve as input to the Levin-Wen string-net models [48], which realize non-chiral topological phases whose anyon content corresponds to the Drinfeld center of the input category. Gapped boundary conditions of these string-nets are classified by module categories over the input fusion category.

2.1 Fusion categories and their graphical calculus

This section reviews the essential aspects of fusion categories, following [3, 39, 52]. We introduce their defining data, including the F-symbols that encode associativity, and the graphical calculus that facilitates computations. We also discuss braided fusion categories, which are central to 2+1d topological phases, and give examples ranging from group-based to more exotic categories.

2.1.1 Fusion category data and fusion diagrams

A fusion category $\mathcal{C}$ is specified by three main ingredients. First, a finite set of simple objects $\{\alpha, \beta, \gamma, \dots\}$ including a distinguished identity object $0 \in \mathcal{C}$. Second, fusion rules

$$\alpha \otimes \beta = \oplus_\gamma N_{\alpha\beta}^{\gamma}\, \gamma \ , \tag{2.1}$$

where the fusion coefficients $N_{\alpha\beta}^{\gamma} \in \{0, 1\}$ count the multiplicity of the simple object γ in the tensor product of α and β. The fusion product is associative, and the identity object acts trivially: $\alpha \otimes 0 = 0 \otimes \alpha = \alpha$ for all $\alpha \in \mathcal{C}$. Third, a set of F-symbols introduced below in (2.2), which implement unitary basis changes.

Fusion diagrams are planar trivalent graphs whose edges are labeled by objects in the category. At each trivalent vertex, the labels of its incident edges have to satisfy $N_{\alpha\beta}^{\gamma} \neq 0$. Different fusion diagrams can be transformed into each other via F-moves,

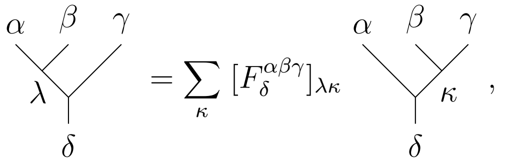

$$= \sum_{\kappa} [F_{\delta}^{\alpha\beta\gamma}]_{\lambda\kappa} \ , \tag{2.2}$$

where the complex coefficients $[F_{\delta}^{\alpha\beta\gamma}]_{\lambda\kappa}$ are known as F-symbols (or associators in mathematical terminology). They must obey the pentagon equations, which capture the associativity of sequential fusion processes.

To evaluate a fusion diagram means to assign it a complex number that does not change under isotopy, i.e., continuous deformations. Moreover, the evaluation is invariant under F-moves (2.2). Two useful identities for computing such evaluations are:

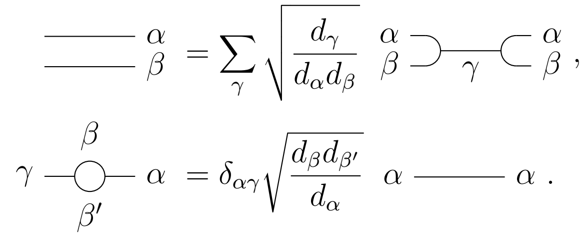

(2.3)

Here, d_α denotes the quantum dimension of the object α, defined as the largest eigenvalue of the matrix $(N_\alpha)^\gamma_\beta = N^\gamma_{\alpha\beta}$. The total quantum dimension of $\mathcal{C}$ is defined as $D^2 = \sum_{\alpha\in\mathcal{C}} d^2_\alpha$.

To simplify the graphical calculus and computations, we impose several technical assumptions: We restrict to multiplicity-free fusion categories, meaning $N^\gamma_{\alpha\beta} \in \{0, 1\}$. All Frobenius-Schur indicators are assumed to be trivial, which ensures that lines can be bent and straightened without ambiguity. The category is unitary, so all F-symbols $[F^{\alpha\beta\gamma}_\delta]_{\lambda\kappa}$ form unitary matrices in the lower indices λ, κ. The fusion diagrams can be rotated freely, since any unitary fusion category admits a pivotal structure. Except in Section 4.5, we work with categories where all objects are self-dual, i.e., $0 \in \alpha \otimes \alpha$. In such categories, fusion lines carry no orientation.

A few examples of fusion categories that will appear later are introduced below:

- For any finite group G, one can define a fusion category Vec^ω_G whose simple objects are labeled by group elements $a \in G$. Fusion is given by group multiplication, and the F-symbols are phase factors $\omega(a, b, c) \in U(1)$ satisfying a 3-cocycle condition on G. The trivial cocycle $\omega = 1$ always provides a valid solution.

- The category $\mathrm{Rep}(G)$ of finite-dimensional representations of a finite group G forms a fusion category. The simple objects are the irreducible representations, with quantum dimensions equal to their vector space dimensions. Fusion is given by the tensor product of representations.

- The Ising category has three simple objects $\{0, 1, \sigma\}$ with fusion rules

  $$\sigma \otimes \sigma = 0 \oplus 1, \quad 1 \otimes 1 = 0, \quad \sigma \otimes 1 = \sigma.$$

  The non-abelian object σ has quantum dimension $d_\sigma = \sqrt{2}$.

- The Fibonacci category has two simple objects $1, \tau$ (with 1 denoting the identity object here), and fusion rule $\tau \otimes \tau = 1 \oplus \tau$. The quantum dimension of τ is the golden ratio, $d_\tau = \frac{1+\sqrt{5}}{2}$.

2.1.2 Braiding

Braided fusion categories include additional structure that allows lines to cross in the graphical calculus. The braiding is encoded in the R-symbols, which are complex phases:

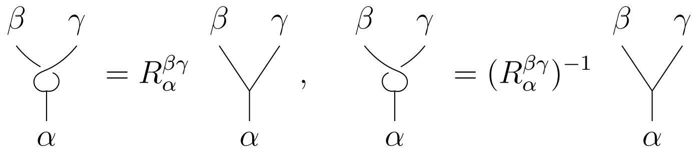

Since all categories considered here are unitary, the inverse braiding is given by the complex conjugate,

$$(R_\alpha^{\beta\gamma})^{-1} = (R_\alpha^{\beta\gamma})^*$$

Compatibility of fusion and braiding follows from the hexagon equations, a set of consistency equations satisfied by the F- and R-symbols. Graphically, this allows strands to slide over fusion vertices:

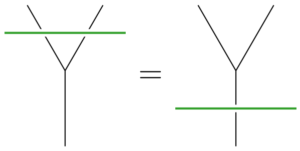

A modular tensor category is a braided tensor category with a non-degenerate topological S-matrix. The S-matrix entry $S_{\alpha\beta}$ is given by a Hopf link between objects α and β:

$$S_{\alpha\beta} = \frac{1}{D}$$

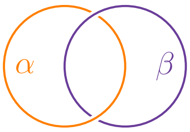

Non-degeneracy means that for each object $\alpha \neq 0$, there exists some β such that the full braiding of β around α is nontrivial, i.e., $R^{\alpha\beta}R^{\beta\alpha} \neq \mathbb{I}$ (where $R^{\alpha\beta}$ is the diagonal matrix with entries $R^{\alpha\beta}_{\gamma}$). This ensures the theory can be consistently defined on closed 2D manifolds, such as the torus. The braiding and fusion of anyons in a $(2+1)$d topologically ordered phase are expected to be captured by a unitary modular tensor category.

2.2 Levin-Wen string-nets

Levin and Wen [48] introduced a class of 2+1d commuting projector models defined on trivalent graphs, which realize doubled topological phases. Their construction is based on the data of a unitary spherical fusion category. When the input category is group-like, the resulting model reduces to Kitaev's quantum double model [47], including familiar examples like the toric code. The string-net framework was subsequently generalized to realize arbitrary non-chiral topological orders $\mathcal{Z}(\mathcal{C})$ that admit gapped boundary conditions, beyond the doubled case $\mathcal{C} \boxtimes \overline{\mathcal{C}}$ [53–57].

2.2.1 Hamiltonian and excitations

The Hilbert space of the string-net model is defined on a trivalent graph—typically a honeycomb lattice—whose edges are labeled by simple objects $\Gamma_e \in \mathcal{C}$:

$$|\{\Gamma_e\}\rangle =$$

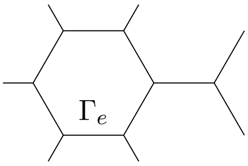

with $\Gamma_e \in \mathcal{C}$.

At this stage, edge labels are unconstrained, so the Hilbert space has dimension $|\mathcal{C}|^{N_e}$, where $|\mathcal{C}|$ denotes the number of simple objects and N_e is the number of edges. The fusion rules are not yet imposed at the vertices.

The Hamiltonian takes the form

$$H = -\sum_v A_v - \sum_p B_p, \tag{2.4}$$

where A_v and B_p are mutually commuting projectors. The vertex terms A_v energetically enforce the fusion rules at each trivalent vertex:

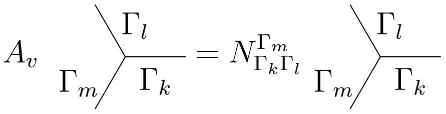

The plaquette term is defined as $B_p = \frac{1}{D}\sum_{\alpha\in\mathcal{C}} d_\alpha B_p^{(\alpha)}$ with $B_p^{(\alpha)}$ acting as

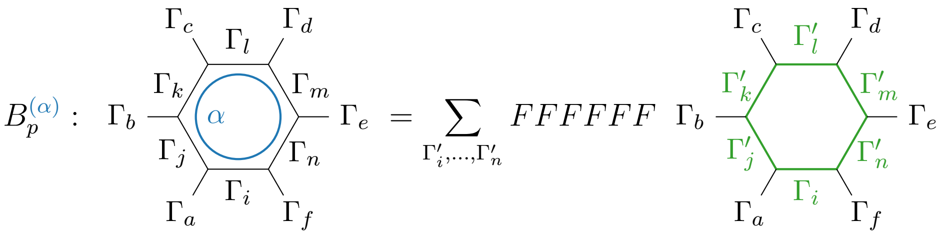

The operator $B_p^{(\alpha)}$ acts on the 12 edges surrounding and radiating from a plaquette p, modifying only the six inner edges. Its action can be expressed as a sequence of F-moves, though we suppress the explicit index structure of the F-symbols here.

All vertex operators A_v and plaquette operators B_p commute, so the model is exactly solvable. Ground states are simultaneous $+1$ eigenstates of all A_v and B_p projectors. On a closed surface, the ground state degeneracy depends only on the topology and is related to the Turaev-Viro invariant [58, 59]. On a disk or sphere, there is a unique ground state.

Anyonic excitations correspond to eigenstates with $A_v = 0$ or $B_p = 0$ at a certain vertex or plaquette. They can be created pairwise by open string operators labeled by an object in the Drinfeld center $\mathcal{Z}(\mathcal{C})$:

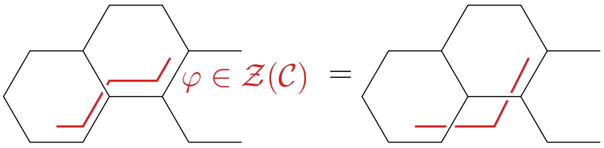

When acting on ground states, string operators are path-independent, as illustrated above. Each anyon $\varphi \in \mathcal{Z}(\mathcal{C})$ can be written as a pair (α, Ω_α), where α is an object in $\mathcal{C}$ and Ω_α is a collection of half-braiding phases [60]. These half-braiding phases are used to resolve the under-crossings between the red string and the black edges shown in the diagram.

2.2.2 Boundaries and module categories

Gapped boundaries of a string-net with edge labels in a fusion category $\mathcal{C}$ are classified by module categories $\mathcal{M}$ over $\mathcal{C}$ [53],

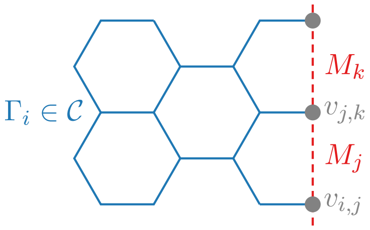

A right module category $\mathcal{M}$ consists of a set of objects $\{M, N, \ldots\} \in \mathcal{M}$ equipped with a right action $M \triangleleft \alpha = \oplus_N N$ for objects $\{\alpha, \beta, \ldots\} \in \mathcal{C}$. Pictorially, this action is represented by a trivalent vertex where two lines labeled by objects in the module category $\mathcal{M}$ meet a single line labeled by an object in the fusion category $\mathcal{C}$. The vector space $\mathcal{V}^{M}\alpha N$ associated with such a vertex is generally multidimensional, even if the fusion category $\mathcal{C}$ is multiplicity-free. It is therefore labeled by basis vectors $v \in \mathcal{V}^{M}\alpha N$ spanning the space. Common examples of module categories include: the regular module category $\mathcal{M} = \mathcal{C}$, as well as $\mathcal{M} = \text{Rep}(H)$ when $\mathcal{C} = \text{Rep}(G)$ and $H \subset G$.

The associativity of the module action is encoded in module F-symbols,

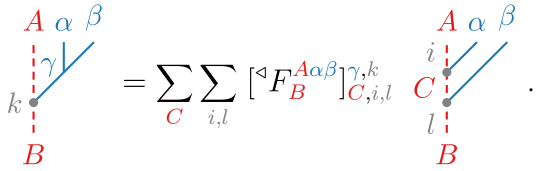

$$= \sum_{C} \sum_{i,l} [{}^{\triangleleft}F^{A\alpha\beta}_{B}]^{\gamma,k}_{C,i,l} \quad . \tag{2.5}$$

Choosing orthonormal bases for the vector spaces $\mathcal{V}^M_{\alpha N}$ allows us to impose orthogonality and completeness conditions similar to (2.3):

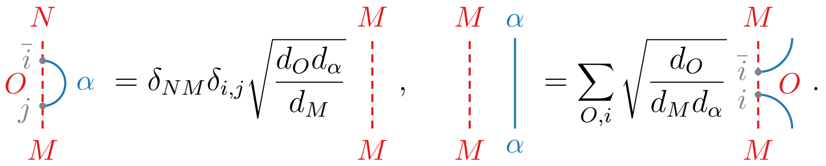

$$= \delta_{NM}\delta_{i,j}\sqrt{\frac{d_O d_\alpha}{d_M}} \quad , \qquad = \sum_{O,i}\sqrt{\frac{d_O}{d_M d_\alpha}} \quad . \tag{2.6}$$

Boundary excitations correspond to objects in the Morita dual fusion category

$\mathcal{C}^*_{\mathcal{M}} = \mathrm{End}_{\mathcal{C}}(\mathcal{M})$, the category of $\mathcal{C}$-module endofunctors of $\mathcal{M}$, as depicted below.

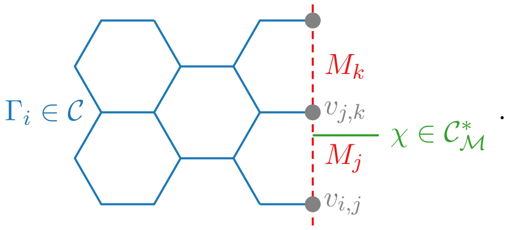

The Morita dual category shares the same Drinfeld center with $\mathcal{C}$, $Z(\mathcal{C}) = Z(\mathcal{C}^*_{\mathcal{M}})$, and makes $\mathcal{M}$ an invertible $\mathcal{C}$–$\mathcal{C}^*_{\mathcal{M}}$ bimodule. The boundary excitations can be moved using the bimodule ${}^{\bowtie}F$-symbols,

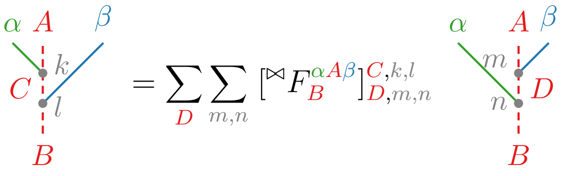

$$= \sum_D \sum_{m,n} [{}^{\bowtie}F^{\alpha A \beta}_{B}]^{C,k,l}_{D,m,n} \tag{2.7}$$

There is a well-known correspondence between module categories $\mathcal{M}$ over $\mathcal{C}$ and algebra objects in $\mathcal{C}$ [53, 61]. Depending on the context, it can be more convenient to work with one perspective over the other. An algebra object is a (non-simple) object $A \in \mathcal{C}$ with a multiplication map $m_A : A \otimes A \to A$ and a unit operator $i_A : 0 \to A$ satisfying associativity and unitality [62],

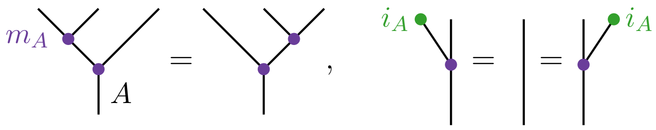

(2.8)

Given an algebra object $A \in \mathcal{C}$, one can construct the associated module category $\mathcal{M} = \mathrm{Mod}_A(\mathcal{C})$. Its objects are right A-modules, which are equivalence classes of objects identified under condensing A; that is, objects $\alpha \in \mathcal{C}$ and $\alpha \otimes A$ are considered equivalent.

2.3 Anyon chains

Anyon chains are 1+1d quantum lattice models constructed from fusion categories [18, 21, 63]. They can be obtained from the anisotropic limit of 2d statistical-mechanical models [3, 6, 7]. A key feature is that the Hamiltonian commutes with non-invertible symmetries whose generators obey the same fusion algebra as the objects in the input category. While fusion categories provide the necessary mathematical structure to define anyon chains with categorical symmetries, module categories over a given fusion category are essential to establish dualities: Different module categories lead to dual chains, related by a matrix product operator implementing the duality transformation [23, 24]. Their energy spectra share the same levels, albeit with different degeneracies, and, in particular, exhibit matching energy gaps in the thermodynamic limit.

2.3.1 Construction and fusion category symmetry

States in the anyon chain Hilbert space correspond to fusion trees of the form

$$|\{\Gamma_i\}\rangle =$$

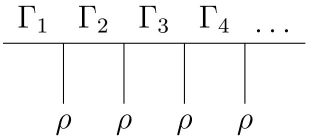

Each vertical leg of the fusion tree is labeled by the same object $\rho \in \mathcal{C}$. The horizontal edges $\Gamma_i \in \mathcal{C}$ are the dynamical degrees of freedom. The dimension of the Hilbert space grows as $\sim d_\rho^L$. The local Hamiltonian $H_{i-1,i,i+1}$ acts on the fusion tree state as

$$H_{i-1,i,i+1} :$$

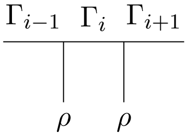

$$\to \sum_\lambda A_\lambda$$

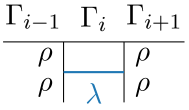

$$, \qquad (2.9)$$

with $\lambda \in \mathcal{C}$ and constants $A_\lambda \in \mathbb{R}$. Each term on the right-hand side of (2.9) can be evaluated using the F-moves (2.2) as well as the resolution of identity and bubble removal (2.3). Explicitly, it follows that

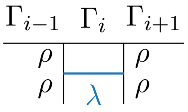

$$= \sum_{\Gamma_i'} \sqrt{\frac{d_{\Gamma_i'}}{d_{\Gamma_i} d_\lambda}}$$

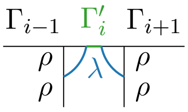

$$= \sum_{\Gamma_i'} \sqrt{d_\lambda} [F^{\Gamma_i'\lambda\rho}_{\Gamma_{i-1}}]_{\Gamma_i\rho} [F^{\rho\lambda\Gamma_i}_{\Gamma_{i+1}}]_{\rho\Gamma_i'}$$

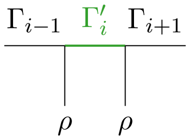

$$.$$

A special choice of Hamiltonian is the projection onto the identity channel,

$$e_i \equiv d_\rho P_i^{(0)} :$$

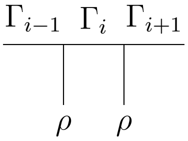

$$\to d_\rho$$

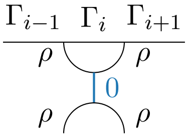

$$,$$

which is equivalent to 2.9 with $A_\lambda = [F_\rho^{\rho\rho\rho}]_{0\lambda}$. This local Hamiltonian generates the Temperley-Lieb algebra [5]:

$$e_i^2 = d_\rho e_i, \quad e_i e_{i\pm1} e_i = e_i, \quad e_i e_j = e_j e_i \text{ for } |i-j| > 1$$

For the input category $\mathcal{A}_k$ – with $\mathcal{A}_3$ equivalent to the Fibonacci category, and $\mathcal{A}_4$ sharing fusion rules with $su(2)_4$, which plays a major role in Section 3 – the anyon chains with this Temperley-Lieb Hamiltonian are the anisotropic limits of the ABF models [10].

The local Hamiltonian (2.9) commutes with topological line operators $D^{(\alpha)}$ labeled by simple objects $\alpha \in \mathcal{C}$:

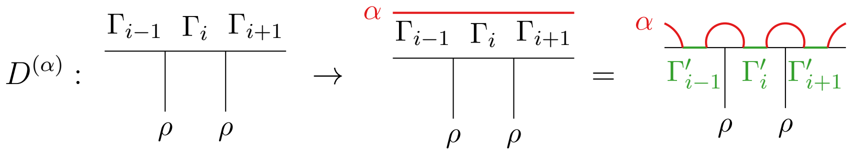

$$= \dots [F_\rho^{\Gamma'_{i-1}\alpha\Gamma_i}]_{\Gamma_{i-1}\Gamma'_i} [F_\rho^{\Gamma'_i\alpha\Gamma_{i+1}}]_{\Gamma_i\Gamma'_{i+1}} \cdots$$

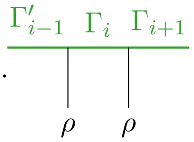

(2.10)

Intuitively, the Hamiltonian acts from below on the fusion tree, while the topological lines act from above, so they ought to commute:

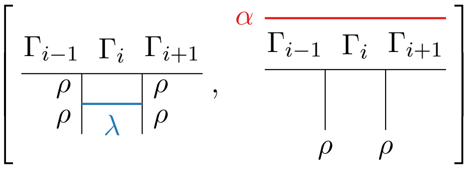

$= 0$ (2.11)

Mathematically, this commutation follows from the pentagon equations satisfied by the F-symbols. Consequently, these topological lines implement symmetries when they map the Hilbert space to itself, or dualities when they map to a different Hilbert space. When the quantum dimension $d_\alpha > 1$, they are generally non-invertible. Many examples are given in e.g. [3, 23, 64]. The symmetry generators $D^{(\alpha)}$ obey the same algebra as the corresponding object in the input category and can be naturally expressed as matrix product operators whose tensors incorporate the F-symbols [23]. The local commutation relation (2.11) implies that any Hamiltonian

$H = \sum_i C_i H_{i-1,i,i+1}$ with $C_i \in \mathbb{R}$ will commute with the topological lines $D^{(\alpha)}$. In particular, translation invariance is not required.

Twisted boundary conditions are implemented by gluing an additional vertical leg $\beta \in \mathcal{C}$ to the fusion tree:

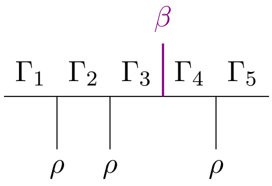

With twisted boundary conditions, it is possible to define a modified translation operator as a combination of the original translation operator and a unitary transformation. The unitary transformation is given by an F-move that moves the defect back to its original location [3].

2.3.2 Dualities between anyon chains from module categories

To capture dualities between different anyon chains, the input data is refined by specifying a module category $\mathcal{M}$ over the fusion category $\mathcal{C}$. In the anyon chain constructed from the category pair $(\mathcal{M}, \mathcal{C})$, the degrees of freedom are now objects $M_i \in \mathcal{M}$ labeling the horizontal edges and basis vectors $v_{i,j} \in \mathcal{V}^{M_i}_{\rho M_j}$ living on the trivalent vertices,

$$|\{M_i\}, \{v_i\}\rangle = \tag{2.12}$$

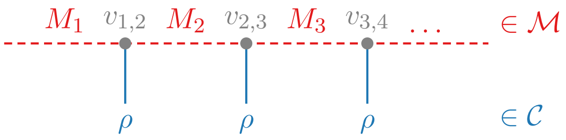

The regular module category $\mathcal{M} = \mathcal{C}$ recovers the construction discussed earlier in Section 2.3.1.

The action of the local Hamiltonian

$$H_{i-1,i,i+1} = \sum_{\lambda \in \mathcal{C}} A_\lambda H^{(\lambda)}_{i-1,i,i+1}$$

on the general state (2.12) is analogous to (2.9), where each $H^{(\lambda)}_{i-1,i,i+1}$ acts as

$$H^{(\lambda)}_{i-1,i,i+1} : \tag{2.13}$$

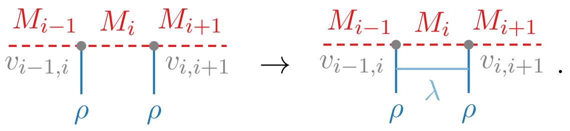

Changing the module category $\mathcal{M}$ does not affect the operator algebra generated by the local terms $H^{(\lambda)}_{i-1,i,i+1}$, as it depends solely on the fusion category $\mathcal{C}$. The corresponding Hamiltonians are therefore dual, with closely related energy spectra: they share the same energy levels (up to possibly twisted boundary conditions), though the same energy levels may occur with different degeneracies, and some may not appear at all in one of the models.

Using the identities (2.6) and (2.5), the local Hamiltonian (2.13) evaluates to

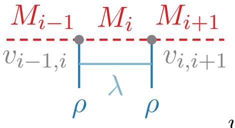

$$= \sum_{\substack{M_i',k \\ v'_{i-1,i},v'_{i,i+1}}} \left[{}^{\triangleleft}F^{M_i\lambda\rho}_{M_{i-1}}\right]^{M_i',v'_{i-1,i}\bar{k}}_{\rho v_{i-1,i}} \left[{}^{\triangleleft}\bar{F}^{M_{i+1}\rho\lambda}_{M_i'}\right]^{M_i,v_{i,i+1},k}_{\rho v'_{i,i+1}} \sqrt{d_\lambda}$$

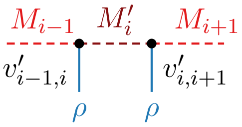

The choice of a module category $\mathcal{M}$ also affects the symmetries of the system. For the regular module category $\mathcal{M} = \mathcal{C}$, the lattice model has a symmetry corresponding to each object in $\mathcal{C}$, cf. (2.10). For generic choices of $\mathcal{M}$, the symmetry category is no longer $\mathcal{C}$, but its Morita dual fusion category $\mathcal{C}^*_{\mathcal{M}}$. Graphically, the symmetry action is depicted as:

$$D^{(\chi)} :$$

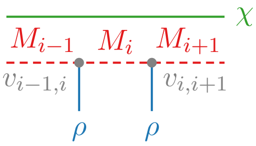

$$\text{for } \chi \in \mathcal{C}^*_{\mathcal{M}} \tag{2.14}$$

The diagram (2.14) can be evaluated explicitly by fusing the symmetry line to the horizontal edges $M_i \in \mathcal{M}$ and utilizing the bimodule F-symbols ${}^{\bowtie}F$ (2.7). Duality transformations between Hamiltonians constructed from different module categories $\mathcal{M}$ and $\mathcal{N}$ can be explicitly expressed as matrix product operators using the data of module functors $X \in \mathrm{Func}(\mathcal{M},\mathcal{N})$ [23]:

$$O^{(X)}H^{\mathcal{M}} = H^{\mathcal{N}}O^{(X)}$$

We will see an example of such a duality operator in Section 3.3.2.

3

The Rydberg-blockade ladder and its phase diagram

Contents

Rydberg atoms provide an attractive platform to simulate strongly correlated quantum many-body systems because of their long lifetime and strong sensitivity to electric fields [33, 65, 66]. Neutral atoms are trapped in optical tweezers and laser-driven to high-lying Rydberg states, where strong dipole-dipole interactions impose a blockade constraint: two atoms within a “blockade” radius cannot be excited simultaneously. By tuning the chemical potential and interaction strengths along with the blockade radius, a wide range of strongly correlated phases and transitions can be accessed.

The minimal theoretical description is the Rydberg-blockade chain with nearest-neighbor exclusion. With only nearest-neighbor interactions, this model exhibits an Ising transition into a $\mathbb{Z}_2$ density-wave phase upon tuning the chemical potential [67], and hosts experimentally observable quantum many-body scars [30, 33]. Adding next-nearest-neighbor interactions leads to a tricritical point [67] and a $\mathbb{Z}_3$-ordered phase with Potts and chiral transitions [67–71]. Along an integrable line, the model maps to the Hamiltonian limit of Baxter’s hard-square model [11, 67], or equivalently the Fibonacci anyon chain [18].

Explorations beyond the chain geometry are more recent, with ladder systems revealing cluster Luttinger liquids, supersymmetric criticality, and order-by-disorder transitions [72–74]. Arrays of coupled chains have been proposed to realize two-dimensional quantum spin liquids [34, 75, 76]. This chapter explores the phase diagram of a Rydberg-blockade ladder, starting from an integrable lattice model built from the $so(3)_2$ fusion category whose the constrained Hilbert space mirrors a Rydberg-type blockade.

3.1 The Rydberg-blockade ladder from the $so(3)_2$ fusion category

We begin by constructing the anyon chain from the subcategory $so(3)_2$ of $su(2)_4$, also known as Rep(S_3). Its simple objects are $\{0, 1, 2\}$ with fusion rules

$$1 \otimes 1 = 0 \oplus 1 \oplus 2, \quad 2 \otimes 1 = 1, \quad 2 \otimes 2 = 0.$$

We follow the notation from [32], where the non-abelian “spin-1” object in $so(3)_2$ is denoted by 1. Labeling all vertical legs with $\rho = 1$ imposes a constraint on the Hilbert space, which admits a natural physical interpretation: it corresponds to Rydberg atoms arranged on a square ladder with a blockade radius satisfying $\sqrt{2} < R_b < 2$ in lattice units:

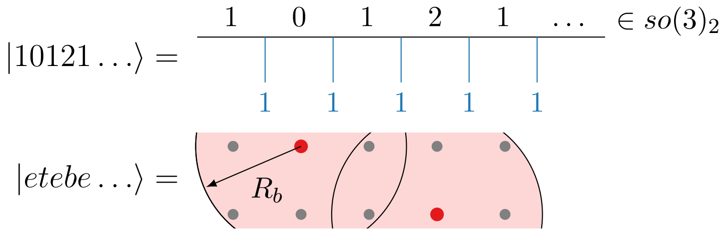

A rung without excitations corresponds to the state $|e\rangle = |1\rangle$, while excitations on the top and bottom of rung j, denoted by $|t\rangle = |0\rangle$ and $|b\rangle = |2\rangle$, are annihilated by hard-core bosonic operators t_j and b_j respectively. The corresponding number operators are $n_j^t = t_j^\dagger t_j$ and $n_j^b = b_j^\dagger b_j$. The fusion rule $\Gamma_{j+1} \in \Gamma_j \otimes \rho$ maps onto requiring at most one excitation per square, which imposes

$$n_j^t n_{j+1}^t = n_j^t n_{j+1}^b = n_j^b n_{j+1}^b = 0 \tag{3.1}$$

for all j. For L rungs, the ensuing Hilbert space is dimension $2^L + (-1)^L$. We utilize the linear combinations

$$p_j = \tfrac{1}{\sqrt{2}}\left(t_j + b_j\right) \;, \quad m_j = \tfrac{1}{\sqrt{2}}\left(t_j - b_j\right) \tag{3.2}$$

and define $|+\rangle = p_j^\dagger |e\rangle$ and $|-\rangle = m_j^\dagger |e\rangle$. We analogously define $n_j^- = m_j^\dagger m_j$ and $p_j^- = p_j^\dagger p_j$ so that the density of empty rungs is

$$n_j^e = 1 - n_j^t - n_j^b = 1 - n_j^+ - n_j^- \;. \tag{3.3}$$

A one-parameter integrable Hamiltonian of this anyon chain or 2d statistical mechanical model has appeared in various contexts [3, 23, 32, 77, 78]:

$$H = \sum_j \left(S_j + \Delta P_j\right), \text{ where}$$

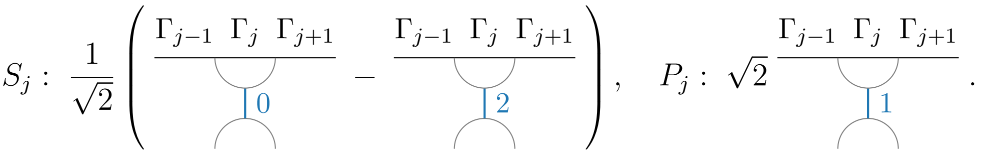

(3.4)

In terms of the bosonic operators defined above, S_j and P_j can be written as

$$S_j = p_j + p_j^\dagger + s_{j-1}s_{j+1}, \quad P_j = n_j^- + \left(n_{j-1}^e - n_{j+1}^e\right)^2,$$

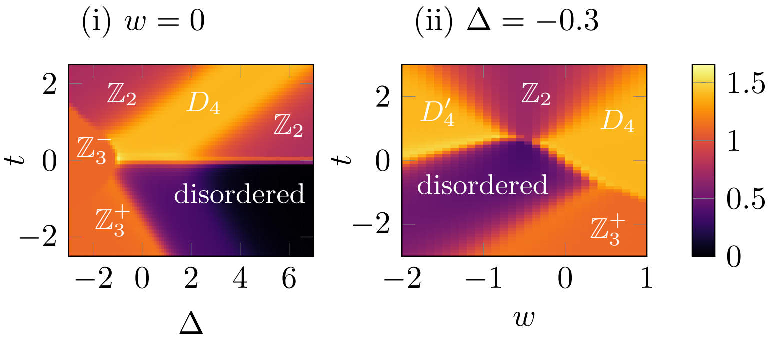

Figure 3.1: The half-cut ground-state entanglement entropy at $L = 12$ from exact diagonalization for (i) $w = 0$, (ii) $\Delta = -0.3$.

where $s_j \equiv n_j^t - n_j^b$ and we assume periodic boundary conditions. We deform the Hamiltonian by including two more couplings w and t that break integrability, yielding

$$H = \sum_{j=1}^{L} \Big((1-w)\big(p_j + p_j^\dagger\big) + (1+2w)s_{j-1}s_{j+1} \\ + (\Delta - 2t)n_j^- + (\Delta + t)\left(n_{j-1}^e - n_{j+1}^e\right)^2 \Big), \tag{3.5}$$

In the ± basis, the first term creates or annihilates + bosons, the second swaps $+ \leftrightarrow -$ on a pair of sites, the third is a chemical potential for − bosons, and the last is a next-nearest-neighbor interaction.

A first look at the rich phase diagram is given in Fig. 3.1, showing the half-cut entanglement entropy for the ground state of H along two planes within the three-parameter space of couplings. Here and elsewhere in this chapter, the exact diagonalization (ED) results are found using the package EDKit [79]. Our more detailed results are summarized in the phase diagram given in Fig. 3.2. The $\mathbb{Z}_2$ and $\mathbb{Z}_3$ labels refer to density-wave phases in which translation symmetry is spontaneously broken down to shifts by two or three sites, respectively.

3.2 Non-invertible symmetries

The Rydberg-blockade ladder Hamiltonian (3.5) features both conventional and non-invertible symmetries, as we discuss in detail in this section. In particular, it preserves a $\mathbb{Z}_2 \times \mathbb{Z}_2$ symmetry and a non-invertible $U(1)$ symmetry. Along the integrable line, an additional non-invertible self-duality is conserved.

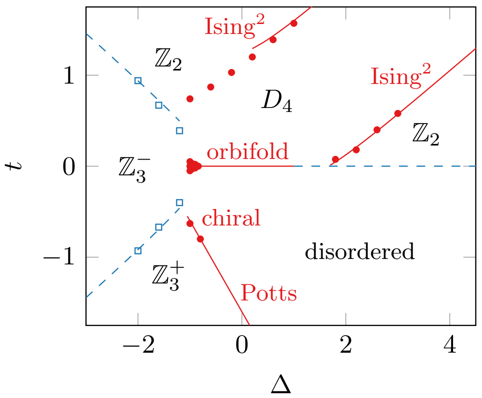

Figure 3.2: Phase diagram of the Rydberg ladder at $w=0$. Critical (red filled circles) and first-order (blue empty squares) transitions are obtained with DMRG ($L=121$). The transition lines at $t=0$ are exact, while the others are perturbative.

For even L, the Hamiltonian (3.5) has a $\mathbb{Z}_2 \times \mathbb{Z}_2$ symmetry exchanging bosons between top and bottom for all even and for all odd rungs. The even generator is

$$F_{\text{even}} = \prod_{l=1}^{L/2} \left(n^e_{2l} + t^\dagger_{2l} b_{2l} + b^\dagger_{2l} t_{2l} \right) = \prod_{l=1}^{L/2} (-1)^{n^-_{2l}} \tag{3.6}$$

The other generator F_{odd} is given by replacing $2l$ with $2l-1$ in (3.6).

Along the integrable line $w = t = 0$, the anyon chain construction guarantees the presence of two symmetry generators $D^{(1)}$ and $D^{(2)}$, cf. (2.10). The $D^{(2)}$ operator corresponds to the diagonal $\mathbb{Z}_2$ symmetry $F = F_{\text{even}} F_{\text{odd}}$, while $D^{(1)}$ is a non-invertible symmetry satisfying the same fusion rules as the non-abelian object:

$$D^{(1)} \cdot D^{(1)} = \mathbb{I} + D^{(1)} + F.$$

All states with charge -1 under the global symmetry F are annihilated by $D^{(1)}$, which is therefore non-invertible. We also call this symmetry a self-duality as it mixes the individual terms in the integrable Hamiltonian (3.4), e.g.

$$\begin{aligned} &D^{(1)} p_j = \left(p_j^\dagger + s_{j-1} s_{j+1} \right) D^{(1)}, \quad D^{(1)} p_j^\dagger = \left(p_j + s_{j-1} s_{j+1} \right) D^{(1)}, \\ &D^{(1)} s_{j-1} s_{j+1} = \left(p_j^\dagger + p_j \right) D^{(1)}. \end{aligned}$$

The w and t perturbations were deliberately chosen to be odd under this self-duality:

$$\begin{aligned} &D^{(1)} \hat{O}^w_j = -\hat{O}^w_j D^{(1)} \quad \text{and} \quad D^{(1)} \hat{O}^t_j = -\hat{O}^t_j D^{(1)} \quad \text{for} \\ &\hat{O}^w_j = 2 s_{j-1} s_{j+1} - p_j - p_j^\dagger, \quad \hat{O}^t_j = \left(n^e_{j-1} - n^e_{j+1} \right)^2 - 2 n^-_j \end{aligned}$$

Hence, the full Hamiltonian (3.5) breaks the self-duality once w or t are turned on. Another way to find this symmetry is via a duality mapping to a 3-state antiferromagnet (see Section 3.3.1), whose $\mathbb{Z}_3$ symmetry maps to the self-duality [32].

The combination of the $\mathbb{Z}_2 \times \mathbb{Z}_2$ symmetry and our blockade constraint makes H (3.5) also invariant under a non-invertible $U(1)$ symmetry [32] generated by

$$\mathcal{Q} = \tfrac{1}{2}\,(1+F)\sum_{j=1}^{L}\sum_{k=0}^{L-1}\prod_{l=0}^{k}(-1)^{1-n^{-}_{j+l}}. \tag{3.7}$$

As apparent from (3.7), $\mathcal{Q}$ is non-vanishing only on the half of the Hilbert space invariant under F. Along the integrable $w = t = 0$ line, the Rydberg ladder is related to the spin-$\frac{1}{2}$ XXZ chain via a non-invertible duality discussed below. Then the symmetry generator (3.7) maps to the squared $U(1)$ charge in XXZ. Remarkably, this non-invertible symmetry survives for nonzero w and t, and plausibly for any perturbation preserving the blockade and the $\mathbb{Z}_2 \times \mathbb{Z}_2$ symmetry. Such a non-invertible $U(1)$ symmetry also appears in the Ashkin-Teller chain, see Appendix A.2, and the free boson orbifold CFT [80], and is similar to the "cosine symmetry" discussed in [81–83].

3.3 Duality mapping to the XXZ chain

One can obtain the integrable Rydberg-blockade ladder by gauging the S_3 symmetry in the spin-$\frac{1}{2}$ XXZ chain. This duality was crucial in finding the non-invertible $U(1)$ symmetry (3.7), and constrains the phase diagram of the integrable line, as discussed in Sections 3.5 and 3.4. The mapping can be understood in the framework of lattice orbifolds [32, 84]. At criticality, these flow to orbifold transformations between the conformal field theories describing the low-energy continuum limit. However, this approach does not generalize easily to higher dimensions. In contrast, the more systematic module category framework introduced in [23] and reviewed in Section 2.3.2 offers a natural generalization beyond 1+1d as discussed in Chapter 5. In what follows, we present the mapping between the integrable Rydberg ladder and the XXZ chain from both perspectives side by side.

3.3.1 Lattice orbifold approach

The integrable Rydberg ladder is related via a $\mathbb{Z}_2$ lattice orbifold to a 3-state height model version of the 6-vertex model / XXZ chain, as first shown in [84] under the name $\hat{A}_5 \leftrightarrow \hat{D}_5$ duality and explained in more detail in [32]. The XXZ chain can be expressed as $H = \sum_j (S_j + \Delta P_j)$ with

$$S_j = \frac{1}{2}\left(X_{j-1/2}X_{j+1/2} + Y_{j-1/2}Y_{j+1/2}\right), \quad P_j = \frac{1}{2}\left(Z_{j-1/2}Z_{j+1/2} + \mathbb{I}\right). \tag{3.8}$$

The operators S_j and P_j generate a representation of the $so(3)_2$ BMW algebra enhanced by its Jones-Wenzl projector [32], satisfying the relations

$$S_j^2 = 1 - P_j, \quad P_j^2 = P_j, \quad S_jP_j = 0, \quad S_jS_{j\pm1}S_j = P_jS_{j\pm1}P_j = 0. \tag{3.9}$$

All lattice models with local terms obeying this algebra (including the unperturbed Rydberg-blockade ladder (3.4)) are integrable [32].

The 3-state height model version of the XXZ chain has degrees of freedom $s_j \in \{A, B, C\}$ subject to the constraint $s_{j+1} \neq s_j$ for $j = 1, \ldots, L$, which motivated the name "3-state antiferromagnet" in [32]. The constraint can be visualized in an adjacency diagram, where an edge connects two heights if they can be adjacent to each other:

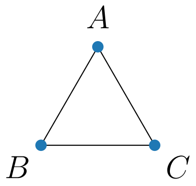

(3.10)

The $\mathbb{Z}_2$ domain walls of this model (up for the configurations $\{AB, BC, CA\}$, and down for $\{BA, CB, AC\}$) are governed by the XXZ Hamiltonian – or stated otherwise, the 3-state antiferromagnet is a $\mathbb{Z}_3$ orbifold of the XXZ chain. Explicitly, the Hamiltonian of the 3-state antiferromagnet takes the familiar form $H = \sum_j (S_j + \Delta P_j)$ with S_j and P_j now defined as

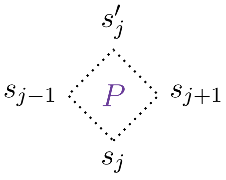

$= |\epsilon_{s_{j-1}s_js_{j+1}}|\delta_{s_js_j'},$

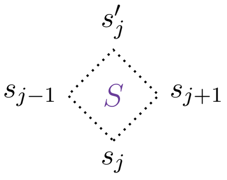

$= |\epsilon_{s_{j-1}s_js_j'}|\delta_{s_{j-1}s_{j+1}}.$

(3.11)

Here, $|\epsilon_{abc}| = 1$ if $a, b, c \in \{A, B, C\}$ are all different and zero otherwise. We adopt the notation from [32] where the rotated square with label S inside denotes matrix elements $\left\langle s_{j-1} s'_j s_{j+1} \right| S_j \left| s_{j-1} s_j s_{j+1} \right\rangle$ of the operator S_j, and similar for P_j.

The adjacency diagram (3.10) has a $\mathbb{Z}_2$ reflection symmetry about the axis perpendicular to the B–C edge, by which we want to orbifold. Under this orbifold, the heights B and C, which are exchanged by the reflection symmetry, are identified into a state called 1. The fixed point A instead doubles into two distinct states, labeled 0 and 2. The resulting adjacency diagram describes precisely the Rydberg ladder constraint: if $h_j \in \{0, 2\}$, then h_{j+1} must equal 1.

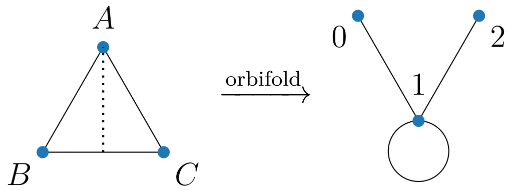

The matrix elements of the S_j and P_j operators in the Rydberg ladder can be derived from the 3-state antiferromagnet matrix elements (3.11) via discrete Fourier transform, see Equations 2.17-2.19 in [84]. For example, the S_j matrix elements follow as

$$\begin{array}{ccc} & 1 & \\ \begin{array}{c}0\\2\end{array} & S & \begin{array}{c}0\\2\end{array} \\ & 1 & \end{array} = \begin{array}{ccc} & B & \\ A & S & A \\ & B & \end{array} + \begin{array}{ccc} & C & \\ A & S & A \\ & B & \end{array} = 0 + 1 = 1,$$

$$\begin{array}{ccc} & 1 & \\ \begin{array}{c}0\\2\end{array} & S & \begin{array}{c}2\\0\end{array} \\ & 1 & \end{array} = \begin{array}{ccc} & B & \\ A & S & A \\ & B & \end{array} - \begin{array}{ccc} & C & \\ A & S & A \\ & B & \end{array} = 0 - 1 = -1,$$

$$\begin{array}{ccc} & 0\,/\,2 & \\ 1 & S & 1 \\ & 1 & \end{array} = \frac{1}{2} \begin{array}{ccc} & A & \\ B & S & B \\ & C & \end{array} = \frac{1}{2}, \qquad \begin{array}{ccc} & 1 & \\ 1 & S & 1 \\ & 0/2 & \end{array} = \frac{1}{2} \begin{array}{ccc} & C & \\ B & S & B \\ & A & \end{array} = \frac{1}{2}.$$

This is precisely the S_j operator in the Rydberg ladder Hamiltonian written in the t_j / b_j basis, see (3.4):

$$S_j = \tfrac{1}{2} \left(t_j^\dagger + t_j + b_j^\dagger + b_j \right) + \left(n^t_{j-1} - n^b_{j-1} \right) \left(n^t_{j+1} - n^b_{j+1} \right)$$

The matrix elements of the duality operator mapping between the 3-state antiferromagnet and the Rydberg ladder can be reverse-engineered from comparing the matrix elements of the respective S_j and P_j operators, see Section 4.3 in [32].

3.3.2 Module category approach

We start by choosing the trivial module category $\mathcal{M} = \mathrm{Vec}$ over the input category $\mathcal{C} = \mathrm{Rep}(S_3)$. This results in an anyon chain where the Hilbert space is a tensor product of qubits $v_{i,i+1} \in \mathbb{Z}_2$ located on the trivalent vertices, while the horizontal edges are labeled by the unique simple object $\underline{0} \in \mathrm{Vec}$ and thus contribute no dynamical degrees of freedom:

$|\{v_i\}\rangle =$

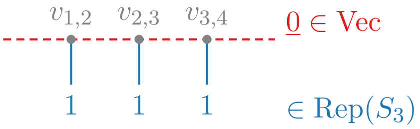

with $v_{i,i+1} \in \mathbb{Z}_2$. (3.12)

This can be seen as follows: For any subgroup $H \subseteq S_3$, $\mathrm{Rep}(H)$ serves as a module category over $\mathrm{Rep}(S_3)$ via the restriction functor $\mathrm{Res}^{S_3}_{H} : \mathrm{Rep}(S_3) \to \mathrm{Rep}(H)$. The module action is defined as $M \triangleleft \alpha \equiv M \otimes \mathrm{Res}^{S_3}_{H}(\alpha)$ for all $M \in \mathrm{Rep}(H)$ and $\alpha \in \mathrm{Rep}(S_3)$ [61]. In our example of $\mathcal{M} = \mathrm{Vec} \simeq \mathrm{Rep}(\mathbb{Z}_1)$, the restriction functor acts as $\mathrm{Res}^{S_3}_{\mathbb{Z}_1}(0) = \mathrm{Res}^{S_3}_{\mathbb{Z}_1}(2) = \underline{0}$ and $\mathrm{Res}^{S_3}_{\mathbb{Z}_1}(1) = 2 \cdot \underline{0}$ for $0, 1, 2 \in \mathrm{Rep}(S_3)$ and $\underline{0} \in \mathrm{Vec}$. The notation $2 \cdot \underline{0}$ means two copies of the object $\underline{0}$. In particular, this implies $\underline{0} \triangleleft 1 = 2 \cdot \underline{0}$, which results in the $\mathbb{Z}_2$ degrees of freedom $v_{i,i+1} \in \mathcal{V}^{\underline{0}}_{1\underline{0}}$ on the trivalent vertices in (3.12). On this Hilbert space, the Rydberg ladder Hamiltonian (3.4) reduces exactly to the XXZ chain (3.8).

The $\mathrm{Rep}(S_3)$ symmetry of the integrable Rydberg ladder—generated by the $\mathbb{Z}_2$ symmetry $D^{(2)}$ and the self-duality $D^{(1)}$—is Morita dual to the invertible S_3 symmetry of the XXZ chain. The duality transformation between the Rydberg ladder and the XXZ chain can be implemented by a matrix product operator $\hat{O}^{(\underline{0} \in \mathrm{Vec})}$ intertwining the Hamiltonians:

$$\hat{O}^{(\underline{0})} H^{\mathcal{M}=\mathrm{Rep}(S_3)} = H^{\mathcal{M}=\mathrm{Vec}} \hat{O}^{(\underline{0})} \tag{3.13}$$

The action of the MPO can be visualized graphically as

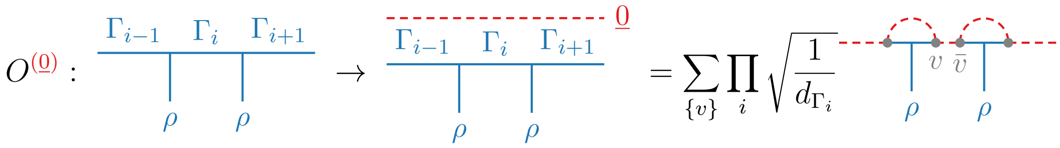

Using the module ${}^{\triangleleft}F$ symbols, this can be further simplified to obtain the matrix elements of $\hat{O}^{\underline{0}}$.

3.4 Non-invertible symmetry breaking along the integrable line

The non-invertible symmetries play an important role in the phase diagram of the integrable Rydberg-blockade ladder, yielding three separate phases as Δ is tuned:

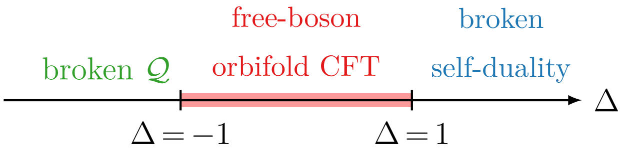

As $\Delta \to \infty$, the Rydberg ladder has three ground states not related by any conventional symmetry:

$$|eeeeee\ldots\rangle\,,\ |{+e+e+e}\ldots\rangle\,,\ |e+e+e+\ldots\rangle\,.$$

Thus one might expect that for finite Δ, the degeneracy is lifted. Remarkably, the self-duality requires that the degeneracy persists, as $D^{(1)}$ maps between the three ground states even when they are no longer exactly known. Since the XXZ chain remains gapped until $\Delta = 1$, the same must hold for the Rydberg ladder. In the three-parameter phase diagram discussed below in Section 3.6, we show how this gapped line with spontaneously broken self-duality describes a first-order transition between a $\mathbb{Z}_2$-ordered and a disordered phase.

On the opposite side, for $\Delta < -1$, the model enters a gapped phase with exact ground states that are degenerate even for finite size. They are analogous to the exact ferromagnetic ground states $|{\uparrow\uparrow\uparrow\uparrow}\ldots\rangle$ and $|{\downarrow\downarrow\downarrow\downarrow}\ldots\rangle$ of the XXZ chain and take the form

$$|{-ee-ee}\ldots\rangle\,,\quad |e-ee-e\ldots\rangle\,,\quad |ee-ee-\ldots\rangle$$

Similar to the exact ferromagnetic ground states in XXZ, these states maximize the non-invertible $U(1)$ charge $\mathcal{Q}$ (3.7). They occur only when L is a multiple of 3. The non-invertible self-duality $D^{(1)}$ permutes them as well, but their degeneracy is already guaranteed by translation invariance.

3.5 Free boson orbifold CFT in the critical integrable Rydberg ladder

The duality mapping implies that the Rydberg ladder is critical for $|\Delta| \leq 1$, just as the XXZ chain. Its continuum limit is described by a free-boson orbifold conformal field theory (except at $\Delta = -1$, where the Fermi velocity is zero). This CFT is labeled by a radius R and contains operators $C_{l,m}$ of dimension $x_{l,m}$ for non-negative integers l, m, where

$$\Delta = -\cos\frac{2\pi}{9}R^2 \ , \qquad x_{l,m} = \frac{l^2}{4R^2} + m^2 R^2 \tag{3.14}$$

so that $0 < R \leq 3/\sqrt{2}$. The other primary operators in the orbifold CFT are called twist fields. There are two of dimension $x = \frac{1}{8}$ and two of dimension $\frac{9}{8}$, denoted by $\sigma_{1,2}$ and $\sigma'_{1,2}$ respectively.

To verify Eq. (3.14) and support the identification of lattice and CFT symmetries, we analyze the finite-size spectrum of the Hamiltonian (3.4). In the limit $L \to \infty$, the low-lying energy levels of a critical lattice model are related to the scaling dimensions of CFT fields according to [85, 86]:

$$E_i = \frac{2\pi v_F}{L}\Big(x_i - \tfrac{1}{12}\Big) \ , \qquad v_F = \pi\frac{\sqrt{1-\Delta^2}}{\arccos\Delta}. \tag{3.15}$$

Here the Fermi velocity v_F is determined using the integrability of the XXZ chain, and the subtraction factor $\frac{1}{12}$ follows from the central charge $c = 1$ of the free boson orbifold CFT. We use exact diagonalization via the package EDKit [79] to find the energies for various values of Δ, and give the results in Fig. 3.3. The agreement with the CFT dimensions is excellent. We also find that states created by $C_{l,m}$ have lattice translation eigenvalue $e^{ik} = (-1)^{l+m}$, while those created by

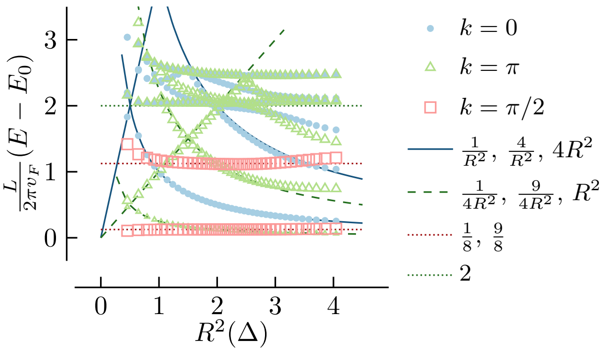

Figure 3.3: The lowest-lying rescaled energy gaps of the $L = 12$ integrable Rydberg ladder with parameter Δ found using ED are plotted against the squared radius $R^2(\Delta)$.

the twist fields have $e^{ik} = \pm i$. This indicates that the unit cell for taking the continuum limit is comprised of four sites.

The orbifold CFT is invariant under a D_4 symmetry, the symmetry group of the square. Its generators $\overline{F}_1$, $\overline{F}_2$ and $\overline{E}$ act on the CFT fields as [32]:

$$\overline{F}_1: \ \sigma_1 \to (-1)\sigma_1, \quad \sigma_2 \to \sigma_2, \quad \sigma_1' \to (-1)\sigma_1', \quad \sigma_2' \to \sigma_2', \quad C_{l,m} \to (-1)^m C_{l,m}$$

$$\overline{F}_2: \ \sigma_1 \to \sigma_1, \quad \sigma_2 \to (-1)\sigma_2, \quad \sigma_1' \to \sigma_1', \quad \sigma_2' \to (-1)\sigma_2', \quad C_{l,m} \to (-1)^m C_{l,m}$$

$$\overline{E}: \ \sigma_1 \to \sigma_2, \quad \sigma_1' \to \sigma_2', \quad \sigma_2 \to \sigma_1, \quad \sigma_2' \to \sigma_1', \quad C_{l,m} \to (-1)^l C_{l,m}$$

The lattice analogues of the $\overline{F}_1$, $\overline{F}_2$ operators are the $\mathbb{Z}_2 \times \mathbb{Z}_2$ symmetry generators F_{even} and F_{odd} (3.6) of the Rydberg ladder. Translation by a single site turns into an internal $\mathbb{Z}_4$ symmetry $\overline{F}_1\overline{E}$ in the CFT, reflecting the fact that the unit cell used in taking the continuum limit is four sites. This is consistent with the translation generator T obeying $TF_{\text{even}} = F_{\text{odd}}T$, akin to $(\overline{F}_1\overline{E})\,\overline{F}_1 = \overline{F}_2(\overline{F}_1\overline{E})$.

Since the vertex operators in the XXZ chain have charge $2m$ under the $U(1)$ symmetry, we conjecture that the operators $C_{l,m}$ in the orbifold CFT have charge $(2m)^2$ under the non-invertible remnant of $U(1)$ symmetry. We verify this prediction numerically by checking that a variety of levels of dimension $x_{l,m}$ in Fig. 3.3 have charge $4m^2$ under $\mathcal{Q}$. From a $\mathbb{Z}_2$ orbifold mapping of the Rydberg ladder to the 3-state antiferromagnet (see Section 3.3.1) under which the self-duality maps to an ordinary $\mathbb{Z}_3$ symmetry, one can deduce that only operators $C_{l,m}$ with $l = 0$ mod 3 commute with the self-duality [32].

Next, we give more detail into how lattice operators in the integrable Rydberg ladder correspond to those in the CFT. The simplest operators commuting with the $\mathbb{Z}_2 \times \mathbb{Z}_2$ symmetry as well as $\mathcal{Q}$ are those in the Hamiltonian. The Hamiltonian along the integrable line is comprised of two self-dual operators, namely

$$\widehat{O}^1_j = S_j = p^\dagger_j + p^\dagger_j + s_{j-1}s_{j+1}\ , \quad \widehat{O}^\Delta_j = P_j = n^-_j + \left(n^e_{j-1} - n^e_{j+1}\right)^2\ . \tag{3.16}$$

The perturbation terms $\widehat{O}^w_j$ and $\widehat{O}^t_j$ given by

$$\widehat{O}^w_j = 2s_{j-1}s_{j+1} - p_j - p^\dagger_j\ , \quad \widehat{O}^t_j = \left(n^e_{j-1} - n^e_{j+1}\right)^2 - 2n^-_j\,. \tag{3.17}$$

are odd under the self-duality of the integrable line. Since translation symmetry on the lattice becomes an internal symmetry of the CFT, it is useful to consider both staggered and unstaggered lattice operators. For each of these four operators we thus define the combinations

$$\widehat{O}^+_j \equiv \widehat{O}_j + \widehat{O}_{j+1}\ , \qquad \widehat{O}^-_j \equiv \widehat{O}_j - \widehat{O}_{j+1}\ . \tag{3.18}$$

The swap operators

$$s_j = p^\dagger_j m_j + m^\dagger_j p_j, \qquad s'_j = p^\dagger_j m_j - m^\dagger_j p_j. \tag{3.19}$$

provide another basic set of operators. These are odd under the $\mathbb{Z}_2$ symmetries F_{even} and F_{odd} for j even and odd respectively. Thus we do not take the staggered and unstaggered combinations here, but rather treat operators for j even and odd separately. Indeed, the two-point function $\langle s_j s_k\rangle$ vanishes unless j and k are both even or both odd.

It is natural to identify the continuum limit of the simplest lattice operators with the simplest CFT fields possessing the same symmetries. Since the integrable Hamiltonian is comprised of the two self-dual operators from (3.16), varying the coefficient of either changes R in the CFT. The lattice operators $\widehat{O}^{1+}$ and $\widehat{O}^{\Delta+}$ should thus correspond to $|\nabla\Phi|^2$ in the CFT, the exactly marginal field. The anti-self-dual operators defined in (3.17) are invariant under both F_{even}, F_{odd}, and $\mathcal{Q}$. They therefore should correspond to $C_{1,0}$ and $C_{2,0}$ in the staggered and unstaggered

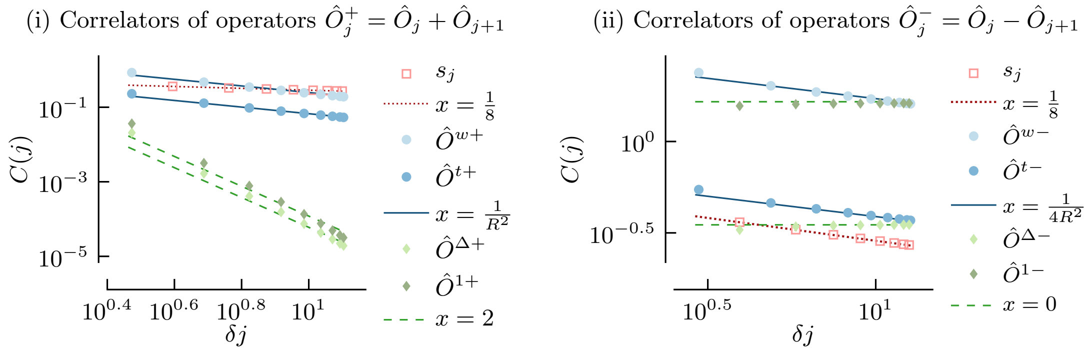
(i) Correlators of operators $\hat{O}_j^+ = \hat{O}_j + \hat{O}_{j+1}$

(ii) Correlators of operators $\hat{O}_j^- = \hat{O}_j - \hat{O}_{j+1}$

Figure 3.4: The two-point correlator (3.20) of the periodic $L = 40$ integrable Rydberg ladder at $\Delta = 0$ found using DMRG for several (i) unstaggered and (ii) staggered lattice operators. The slope is compared to the expected CFT scaling dimensions.

cases respectively. The swap operators s_{even} and s_{odd} are odd under F_{even} and F_{odd} respectively, and so should correspond to σ_1 and σ_2. Likewise, s'_{even} and s'_{odd} should correspond to σ'_1 and σ'_2. We summarize these correspondences in Table 3.1.

lattice:	$(\widehat{O}^{1,\Delta})^+$	$(\widehat{O}^{w,t})^-$	$(\widehat{O}^{w,t})^+$	$s_{j\,\text{even,odd}}$	$s'_{j\,\text{even,odd}}$
CFT:	$\lvert\nabla\Phi\rvert^2$	$C_{1,0}$	$C_{2,0}$	σ_1, σ_2	τ_1, τ_2
dim:	2	$\frac{1}{4R^2}$	$\frac{1}{R^2}$	$\frac{1}{8}$	$\frac{9}{8}$

Table 3.1: Correspondence between lattice and CFT operators

To confirm these identifications, we compute their two-point functions in the ground state. The long-distance behavior of this correlation function in a critical theory is

$$\langle \widehat{O}_0 \widehat{O}_j \rangle - \langle \widehat{O}_0 \rangle \langle \widehat{O}_j \rangle \sim c\big(\delta j\big)^{-2x_{\mathcal{O}}} \ , \quad \delta j \equiv \tfrac{L}{\pi} \sin\left(\tfrac{\pi}{L} j\right) \ , \tag{3.20}$$

where $x_{\mathcal{O}}$ is the scaling dimension of the corresponding continuum field $\mathcal{O}$. The correlation functions are obtained with DMRG using the ITensor library [87], and the hard-core nearest-neighbor constraint is implemented as described in [70]. We plot some for $\Delta = 0$ in Fig. 3.4. We collect our numerical results for a variety of lattice operators for various Δ in Table 3.2, giving strong support to the correspondences in Table 3.1.

lattice op.	$\Delta=-0.5$	$\Delta=-0.2$	$\Delta=0$	$\Delta=0.2$	$\Delta=0.5$
$\widehat{O}_j^{\Delta+}$	2.30 ± 0.20	2.42 ± 0.12	2.44 ± 0.16	2.41 ± 0.20	2.34 ± 0.19
$\widehat{O}_j^{1+}$	2.37 ± 0.22	2.54 ± 0.16	2.56 ± 0.26	2.50 ± 0.29	2.39 ± 0.28
$\lvert\nabla\phi\rvert^2$	2	2	2	2	2
$\widehat{O}_j^{w+}$	0.680 ± 0.019	0.523 ± 0.015	0.456 ± 0.012	0.404 ± 0.011	0.341 ± 0.009
$\widehat{O}_j^{t+}$	0.669 ± 0.010	0.514 ± 0.007	0.449 ± 0.007	0.399 ± 0.008	0.341 ± 0.011
$(n_j^++n_j^-)^+$	0.717 ± 0.001	0.534 ± 0.007	0.461 ± 0.007	0.408 ± 0.006	0.346 ± 0.006
$C_{2,0}$	0.6667	0.5098	0.4444	0.3939	0.3333
$\widehat{O}_j^{w-}$	0.174 ± 0.007	0.131 ± 0.003	0.114 ± 0.002	0.100 ± 0.002	0.0844 ± 0.0007
$\widehat{O}_j^{t-}$	0.1664 ± 0.0003	0.126 ± 0.001	0.110 ± 0.001	0.0972 ± 0.0009	0.0823 ± 0.0005
$(n_j^++n_j^-)^-$	0.168 ± 0.001	0.1282 ± 0.0007	0.1118 ± 0.0006	0.0992 ± 0.0006	0.0840 ± 0.0005
$C_{1,0}$	0.1667	0.1274	0.1111	0.09849	0.08333
s_j	0.1241 ± 0.0007	0.1240 ± 0.0008	0.1240 ± 0.0008	0.1240 ± 0.0008	0.1244 ± 0.0005
σ_1, σ_2	0.125	0.125	0.125	0.125	0.125
s_j'	1.17 ± 0.04	1.159 ± 0.028	1.158 ± 0.029	1.16 ± 0.03	1.16 ± 0.04
σ_1', σ_2'	1.125	1.125	1.125	1.125	1.125

Table 3.2: Scaling dimensions of lattice operators $\widehat{O}_j^{\pm}$ (cf. Eqs. (3.16)-(3.19)) measured with DMRG in the $L=40$ integrable Rydberg ladder with periodic boundary conditions. The scaling dimensions of the corresponding CFT fields are highlighted.

3.6 $\mathbb{Z}_2$, D_4 and $\mathbb{Z}_3$ ordered phases in extreme limits

Next, the Hamiltonian (3.5) is analyzed in various limits where certain coupling constants become large. All of the ordered phases are found in these limits, and several of the transitions are accurately determined using perturbation theory. We also identify the region of parameter space in which the Rydberg ladder effectively behaves as the Rydberg chain introduced in [67].

3.6.1 The Ising^2 limit: D_4 and $\mathbb{Z}_2$ order

We first take $\Delta+t$ positive and much larger than the other coefficients. The final term in (3.5) dominates, and so all pairs of rungs j and $j+2$ must either both be occupied by bosons, or both left empty. The even-L Hilbert space then reduces to two decoupled sectors: one comprised of states $|\pm e\pm e\pm\ldots\rangle$ and the other of states $|e\pm e\pm e\ldots\rangle$. (The entirely empty state is higher energy and can be ignored.) In this limit, the effective Hamiltonian decouples into two identical pieces:

$$\lim_{\Delta+t\to\infty} H=\sum_{j=1}^{L}\Big((1+w)s_{j-1}s_{j+1}+(\Delta-2t)n_j^-\Big) \tag{3.21}$$

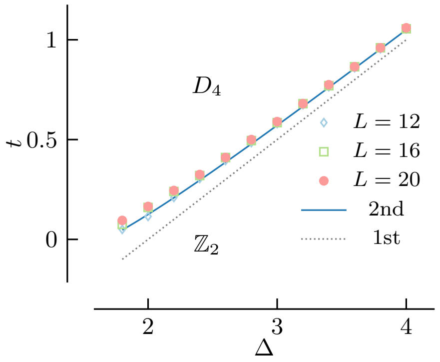

Figure 3.5: Numerical results (ED with $L = 12$, $L = 16$, $L = 20$) and analytical results (1st and 2nd order perturbation theory (3.22)) for the locations $t_+(w, \Delta)$ of Ising squared transitions between the $\mathbb{Z}_2$ ordered phase and the D_4 ordered phase.

giving identical transverse-field Ising chains on odd sites in the first sector and even sites in the second.

Ancient results locate a critical point between order and disorder when the couplings of the two terms in (3.21) are equal in magnitude [88], here corresponding to $\Delta - 2t = \pm 2(1 + w)$. The $p_j + p_j^\dagger$ term in H gives rise to corrections, which can be dealt with in perturbation theory, as described in Appendix A.1. Their effect is to renormalize the n_j^- term in (3.21), shifting the transitions to

$$t_\pm = \frac{\Delta}{2} \pm |1 + w| + \frac{(1+w)^2}{6\Delta \pm 4|1+w|} + \mathcal{O}\Big(\Delta \pm \frac{2|1+w|}{3}\Big)^{-2}. \qquad (3.22)$$

These curves are plotted in Figs. 3.5 and 3.2 along with data for the transition found from ED. The analytical and numerical results agree well for large enough Δ. The two sectors remain independent until the transitions break down, as it takes order L actions of H to mix them. The continuum limit all along these transition lines is thus described by the Ising^2 CFT, i.e. the free boson orbifold CFT at radius $R = 1$.

The symmetry-breaking patterns in this Ising^2 limit (3.21) are easy to obtain. The $\mathbb{Z}_2$ translation symmetry exchanging even and odd sites is spontaneously broken throughout this region. The Ising-disordered regions $t > t_+$ and $t < t_-$ are therefore denoted by $\mathbb{Z}_2$ in Fig. 3.2. For $t_- < t < t_+$ the Ising chains are ordered, and $\mathbb{Z}_2 \times \mathbb{Z}_2$ exchange symmetry is broken as well. Since translation symmetry relates F_{even} and F_{odd}, the full broken symmetry group in this phase is the dihedral group D_4. The four ground states depend on the sign of $1 + w$. For the Ising antiferromagnet $w > -1$, as $t \to \infty$ in this region they are $|tebeteb\dots\rangle$ and its translations. For the Ising ferromagnet $w < -1$, as $t \to \infty$ they are $|tetete\dots\rangle$, $|bebebe\dots\rangle$ and translations. While the broken symmetry is D_4 in both cases, the two phases are distinguishable, as translation symmetry relates all four ground states in the former phase but not the latter. We thus denote the latter phase with a prime, and it is visible at the left of Fig. 3.1(ii) as well as in Fig. 3.7(ii)-(iii) below.

3.6.2 $\mathbb{Z}_3$ phases and their transitions

The physics changes dramatically, not surprisingly, if we consider the opposite sign. Sending $\Delta + t \to -\infty$, we find two distinct $\mathbb{Z}_3$ phases. When $\Delta - 2t$ remains finite, the final term of H dominates and is minimized for a boson on every third site. For $\Delta > 2t \to -\infty$ and L a multiple of 3, the three ground states approach $|+ee+ee\dots\rangle$ and its translations. For $2t > \Delta \to -\infty$, there are three exact ground states $|-ee-ee\dots\rangle$ and its translations. Both regions thus have $\mathbb{Z}_3$ density-wave order, but for L a multiple of 12, no other conventional symmetry is spontaneously broken.

Remarkably, the two phases can still be distinguished. The non-invertible symmetry (3.7) is spontaneously broken in the latter but not the former. Indeed, while $\mathcal{Q}|+ee+ee\dots\rangle = 0$, the exact ground states $|\dots -ee-ee\dots\rangle$ maximize this charge. We thus dub the two phases $\mathbb{Z}_3^+$ and $\mathbb{Z}_3^-$ respectively, and they are readily located in Fig. 3.2 and Fig. 3.7(ii)-(iii).

The first-order transition between the two $\mathbb{Z}_3$ phases occurs when their ground-state energies are equal. In this limit, the effective Hamiltonian is simply

$$\lim_{\Delta+t\to-\infty} H = \sum_{j=1}^{L} (\Delta - 2t) n_j^-, \tag{3.23}$$

so the transition occurs when its coefficient vanishes. Including perturbative corrections as described in Appendix A.1 locates the transition at

$$t_{3^-3^+} \approx \tfrac{\Delta}{2} - \tfrac{(1-w)^2}{6\Delta} + \mathcal{O}\Big(\tfrac{1}{\Delta^2}\Big) \ . \tag{3.24}$$

As apparent from the bottom left of Fig. 3.2, the agreement between this curve and our DMRG numerics is good for a large region. We have no analytic results for the transitions between the D_4 and the $\mathbb{Z}_3$ phases, but our DMRG numerics indicate that they are first-order as well. The transition from the $\mathbb{Z}_3^+$ to the disordered phase is subtler, and we defer a detailed discussion to Section 3.8.

The other transition out of the $\mathbb{Z}_3^-$ phase can be understood by still requiring $\Delta + t \to -\infty$ but now allowing for $\Delta - 2t \to -\infty$ as well. The effective Hamiltonian is then comprised of the last two terms of H, which are diagonal in the ± basis. The $\mathbb{Z}_2$ phase also occurs in this limit, with ground states $|e-e-e-\dots\rangle$ and its translation. The first-order transition occurs when the ground state-energies of the $\mathbb{Z}_3^-$ and $\mathbb{Z}_2$ phases are equal. Including the perturbative corrections from the off-diagonal terms in H (see Appendix A.1) locates it at

$$t_{3^-2^-} \approx -\tfrac{\Delta}{2} + \tfrac{(1+2w)^2}{8\Delta} + \mathcal{O}\Big(\tfrac{1}{\Delta^2}\Big)\ . \tag{3.25}$$

The numerically determined transitions follow the perturbative results (3.24,3.25) fairly well, as apparent in Fig. 3.2.

3.6.3 The chain limit

In the limit $\Delta - 2t \to \infty$, the $-$ bosons are forbidden. The effective Hamiltonian describing the $+$ bosons is

$$H_+ = \sum_{j=1}^{L} \Big((1-w)(p_j + p_j^\dagger) + 2(\Delta + t)\Big(n_j^+ - n_{j-1}^+ n_{j+1}^+\Big)\Big).$$

Ignoring the $-$ bosons makes H_+ precisely the Hamiltonian of the Rydberg-blockade chain along a line of couplings where the chain chemical potential U is equal to $-V$, the next-nearest-neighbor interaction strength [67]. The precise correspondence is $U = -V = 2(\Delta + t)/(1-w)$, where we set to 1 the annihilation/creation coefficient of [67]. This line includes the “PXP” model possessing quantum scars [30] at $U = V = 0$, which is $\Delta = -t$ here.

For large negative $\Delta + t$, H_+ is in the $\mathbb{Z}_3^+$ phase, with a critical transition to the disordered phase [67]. The chain results allow us to locate the analogous transition in the three-parameter space of the ladder. The $U = -V$ line of the chain comes close to the exact three-state Potts critical point at $U \approx -3.03$, $V \approx 3.33$. Since the transition line is smooth as U and V are varied away from the Potts values, we can approximate the critical value on the nearby $U = -V$ line as $U = -V \approx$-3.2. The $\mathbb{Z}_3^+$ to disorder transition therefore occurs at

$$t_{3^+,\mathrm{dis}} \approx -\Delta - 1.6(1-w) + \mathcal{O}\Big(\frac{1}{\Delta}\Big) \ , \tag{3.26}$$

as apparent in Fig. 3.2.

The $\mathbb{Z}_3$ to disordered transition in the chain can be in three-state Potts or chiral-clock universality classes, or take place via an intermediate incommensurate phase [67–70]. There the analysis is aided both by integrability and an extreme limit where incommensurability can be established analytically. Unfortunately, these avenues are not available in the square ladder, as the integrable line here does not cross this transition. We thus need to use numerics to understand the nature of this transition, a task we defer to Section 3.8.

3.6.4 First-order $\mathbb{Z}_2$-disorder transition

The gapped $\Delta > 1$ regime of the integrable line possesses three ground states $|eeee\ldots\rangle$, $|{+}\,e+e\ldots\rangle$ and $|e+e+e\ldots\rangle$ mixed by the self-duality symmetry. This degeneracy is characteristic of a first-order transition between the disordered phase and the $\mathbb{Z}_2$ density-wave order apparent in the Ising^2 limit. The first-order transition, readily apparent in Fig. 3.2, cannot be located exactly away from the integrable line, but perturbation theory works well. For large Δ, the diagonal terms dominate, and we find (see App. A.1)

$$t_{2,\mathrm{dis}} \approx -\Delta w \frac{2+w}{1+2w^2} \ . \tag{3.27}$$

We locate the first-order transition numerically by using ED to find when the gap between the lowest two momentum-zero states closes. The results together with the curve (3.27) are plotted in Fig. 3.6 for $\Delta = 2.5$, with excellent agreement.

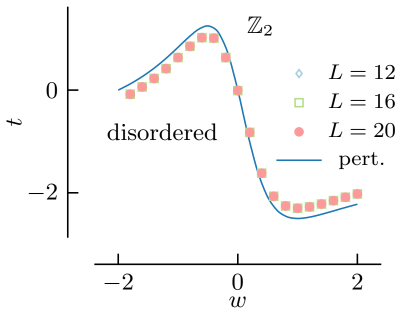

Figure 3.6: Numerical results from ED compared to the perturbative curve (3.27) for the location $t_{2,\mathrm{dis}}$ of the first-order transition between the $\mathbb{Z}_2$ and disordered phases at $\Delta = 2.5$

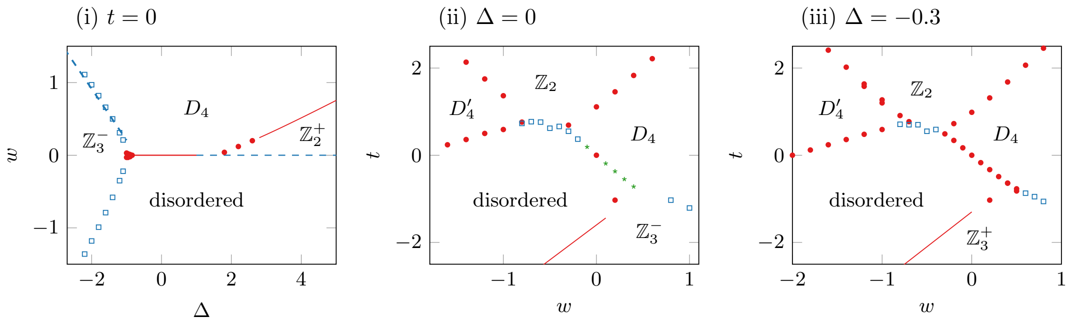

Figure 3.7: The phase diagram of the Rydberg ladder at (i) $t = 0$, (ii) $\Delta = 0$ and (iii) $\Delta = -0.3$ with second order transitions (red filled circles) and first order transitions (darkblue empty squares) and weakly first order transitions (darkgreen stars).

3.7 The D_4-disorder transition and a critical triangle

In this section, we identify the phases surrounding the critical integrable line in the three-dimensional phase diagram and analyze its stability under the w and t perturbations. Our results are summarized in the three planar regions displayed in Fig. 3.7, along with Fig. 3.2 above.

The map to the XXZ chain guarantees that along the integrable $w = t = 0$ line, the system is critical for $|\Delta| \leq 1$. The nearest gapped phases to it are the D_4-broken and the disordered phases, and so it is natural to guess that this critical line governs a transition between the two. To explore this further, we analyze the effective field theory valid for w and t small. The field theory can be described as a perturbation of the CFT by relevant operators invariant under the lattice symmetries. The correspondences in Section 3.5 make finding these operators simple.

Lattice translation sends $C_{l,m} \to (-1)^{l+m} C_{l,m}$ in the CFT, while only the operators $C_{l,0}$ are invariant under the non-invertible symmetry $\mathcal{Q}$. Thus only operators $C_{2n,0}$ of dimension n^2/R^2 appear in the effective continuum Hamiltonian

$$H_{\mathrm{CFT}} + \int dx \Big(\lambda_1 C_{2,0}(x) + \lambda_2 C_{4,0}(x) + \kappa C_{6,0}(x)\Big). \tag{3.28}$$

On the integrable line the system possesses a self-duality under which $C_{2,0}$ and $C_{4,0}$ are not invariant. Thus the integrable line must correspond to setting $\lambda_1 = \lambda_2 = 0$. We indeed identified $C_{2,0}$ above as the leading continuum piece of the anti-self-dual lattice perturbations $\widehat{O}^w$ and $\widehat{O}^t$. Since $C_{4,0}$ is invariant under the same lattice symmetries, it must also appear in (3.28). However, $C_{6,0}$ is self-dual, so $\kappa \neq 0$ even on the integrable line. This operator is of dimension $9/R^2$, so it is irrelevant for $R < 3/\sqrt{2}$. It thus can be ignored until it causes a KT transition to the integrable gapped $\mathbb{Z}_2$/disorder transition line at $\Delta = 1$ [78].

Taking w and/or t nonzero can drive the system into the D_4-broken or the disordered phase. For $\sqrt{2} < R < 3/\sqrt{2}$ $(-0.17 < \Delta \leq 1)$, both $C_{2,0}$ and $C_{4,0}$ are relevant, so the transition between D_4 and disordered phases here should be first order and direct away from $w = t = 0$. Our numerics indicate that the transition is weakly first-order, in that for our system sizes it still exhibits characteristics of a second-order phase transition. We denote these points accordingly in Fig. 3.7(ii).

For $1/\sqrt{2} < R < \sqrt{2}$ $(-0.94 < \Delta < -0.17)$, only $C_{2,0}$ is relevant. Perturbing by either $\widehat{O}^w_j$ or $\widehat{O}^t_j$ still gaps the system. However, since both $\widehat{O}^w_j$ and $\widehat{O}^t_j$ renormalize onto $C_{2,0}$, there must be some linear combination of lattice couplings that makes λ_1 in (3.28) vanish, i.e. $\widetilde{w}\widehat{O}^w_j + \widetilde{t}\widehat{O}^t_j \to C_{4,0}$ in the continuum. Perturbing by this combination thus should preserve the criticality when $C_{4,0}$ is irrelevant, and the orbifold critical line is extended to the 2d region $w/t \approx \widetilde{w}/\widetilde{t}$, for small enough w, t.

Our numerics indeed indicate a direct and critical transition occurs between D_4-ordered and disordered phases governed by the orbifold CFT over a two-dimensional region with non-zero w and t. Results for $\Delta = -0.3$ are plotted in Fig. 3.8, with the corresponding lines shown in the phase diagram in Fig. 3.7(iii). In our DMRG numerics, we chose system sizes $L = 12n + 1$, $n \in \mathbb{N}$ for open boundary conditions so that there is a unique ground state in the $\mathbb{Z}_3$ ordered phase and two (instead of four) ground states in the D_4 ordered phases. The truncation error was fixed at 10^{-11}, and the energy tolerance at 10^{-9} as a convergence criterion. For $L = 601$, MPS bond dimensions up to 300 were typically enough to reach convergence.

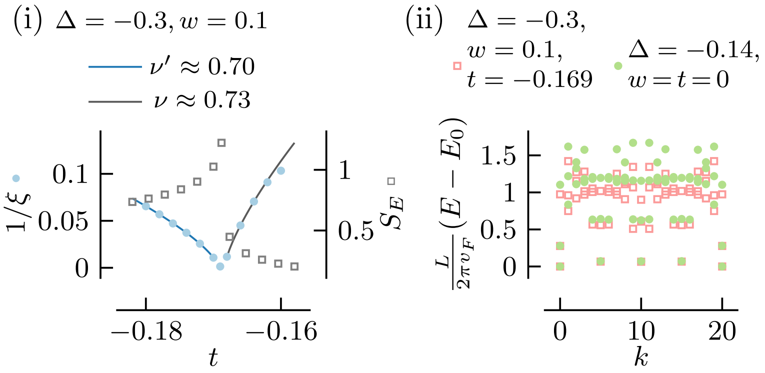

Figure 3.8: (i) Correlation length and half-cut entanglement entropy across the D_4 to disordered transition at $\Delta = -0.3$, $w = 0.1$ with $L = 601$, (ii) energy spectra versus momentum with $L = 20$ at two transition points with a similar CFT radius R: $(\Delta, w, t) = (-0.14, 0, 0)$ and $(-0.3, 0.1, -0.169)$.

On the other hand, for $0 < R < 1/\sqrt{2}$ $(-1 < \Delta < -0.94)$ all the perturbations in (3.28) are irrelevant and the critical line is stable. A small critical cone-shaped region thus occurs in between the D_4, $\mathbb{Z}_3^-$ and disordered phases. A similar critical triangle also appears in the phase diagram of the quantum Ashkin-Teller model [89].

We confirm the presence of the critical triangle close to $\Delta = -1$ by numerically finding the entanglement entropy $S_E(l)$ for open boundary conditions across bond $l = 1, \ldots, L/2$. In a CFT, $S_E(l)$ obeys the Calabrese-Cardy formula [90]

$$S_E(l) = \frac{c}{6} \log\left(\frac{2L}{\pi} \sin\frac{\pi l}{L}\right) + \text{const} . \tag{3.29}$$

with c the central charge. Convergence of DMRG is slow because $v_F \to 0$ from (3.15) as $\Delta \to -1$, but we were able to find convincing evidence that the curve fits the formula throughout the triangular regions in Figs. 3.2 and 3.7(i). We plot the extracted central charge at $w = 0$ in Fig. 3.9.

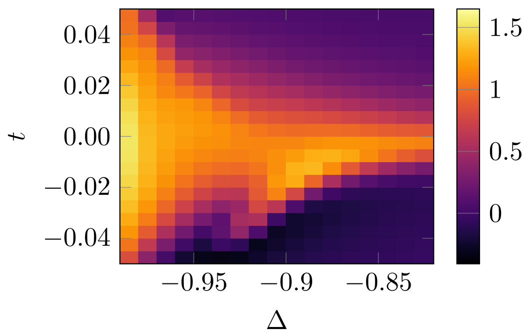

Figure 3.9: Central charges close to $\Delta=-1$ at $w=0$ found with $L=121$ DMRG by fitting the entanglement entropy to (3.29).

3.8 The chiral $\mathbb{Z}_3$ transition

The last topic we address is the nature of the $\mathbb{Z}_3^+$ to disordered transition. This transition is apparent in Figs. 3.2 and 3.7(iii), with the location given approximately by (3.26). It is critical in the chain limit of Section 3.6, and our numerics indicate it remains so until it collides with the first-order line separating the two $\mathbb{Z}_3$ phases. However, determining the precise type of transition requires a careful analysis, as both chiral transitions and intermediate incommensurate regions occur in the chain [67–70].

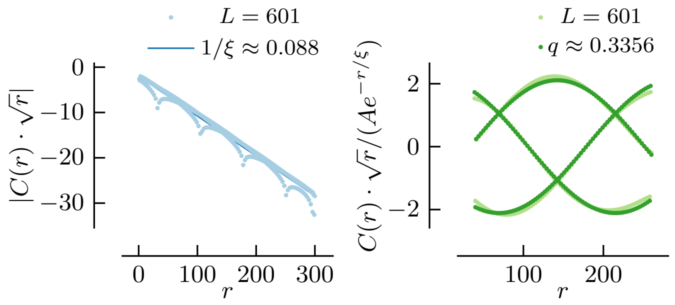

Figure 3.10: On the left, the logarithm of $|G(r)\sqrt{r}|$ is fitted linearly to extract the correlation length ξ at $w=0$, $\Delta=-0.92$, $t=-0.63$. The reduced correlation function $G(r)\sqrt{r}/(Ae^{-r/\xi})$ is fitted to a cosine function on the right to extract the wave vector q.

We utilize the numerical method of [69] and study the boson-density two-point correlator

$$G(r) = \langle(1-n_r^e)(1-n_0^e)\rangle - \langle 1-n_r^e\rangle\langle 1-n_0^e\rangle\ . \tag{3.30}$$

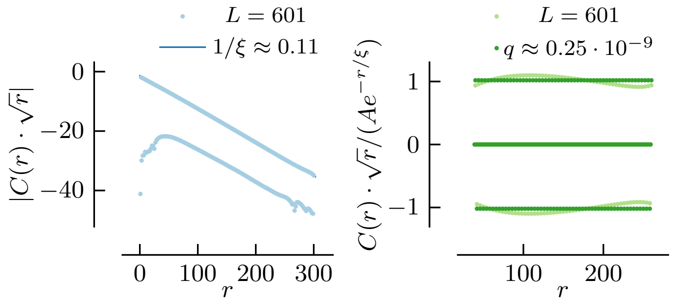

Figure 3.11: As with Fig. 3.10, but here close to the D_4 to disorder transition at $w = 0.1$, $\Delta = -0.48$, $t = -0.16$. The resulting wave vector is $q = 1/4$.

We use their two-step fitting procedure to fit it to the Ornstein-Zernicke relation

$$G(r) \propto e^{-r/\xi} \frac{\cos(2\pi q r + \phi_0)}{\sqrt{r}} \; . \tag{3.31}$$

As illustrated in Figs. 3.10 and 3.11, we first extract the correlation length ξ from fitting $|G(r)\sqrt{r}|$, and then use it to extract the wave vector q by fitting the cosine function. The latter figure provides a useful check, as we do not expect the D_4 to disorder transition to be chiral (as observed in e.g. [91] for a $\mathbb{Z}_4$ transition). The reason is that here operators $C_{n,-n}$ which induce chiral perturbations are forbidden by the non-invertible $U(1)$ symmetry $\mathcal{Q}$. We indeed find that the wave vector is always $q = 1/4$, excluding the possibility of a chiral transition.

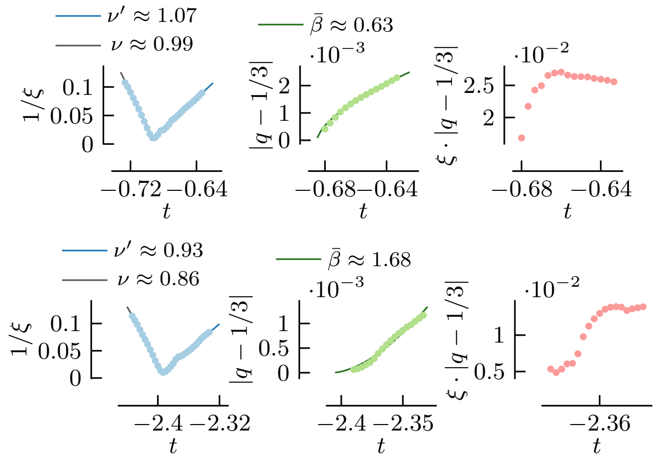

Figure 3.12: The wave vector q, correlation length ξ and their product across the $\mathbb{Z}_3^+$-disorder transition at $w = 0$, $\Delta = -0.6 + 0.5t$ (top row) and $\Delta = 2 + 0.5t$ (bottom row). The DMRG data obtained with $L = 601$ sites is plotted together with power-law fits for the exponents ν, ν' and $\bar{\beta}$.

However, we have strong evidence that the $\mathbb{Z}_3^+$ to disordered transition indeed can be chiral. We display our results for several points along this line in Fig. 3.12. At small Δ (top row), the product $\xi \cdot |q - 1/3|$ seems to go to a very small but finite value and the exponent $\bar{\beta}$ is closer to the prediction $\bar{\beta} = \nu$ for a chiral transition than to the Potts value $\bar{\beta} = 5/3$. At large Δ (bottom row), the product $\xi \cdot |q - 1/3|$ seems to go zero and the exponent $\bar{\beta}$ is in good agreement with the Potts value $\bar{\beta} = 5/3$. We conclude that the $\mathbb{Z}_3^+$ transition in the ladder is likely to be a chiral transition for smaller Δ, and a Potts transition for large Δ. We were not able to locate a sharp transition between the chiral regime and the Potts regime, and so presume that the strength of the chiral perturbations gradually decays with increasing Δ.

We find no evidence of any incommensurate phase, despite one occurring in the chain. However, we note that the incommensurate phase in the chain (established definitively in an extreme limit) is rather small and almost impossible to see numerically. Thus our lack of evidence for its existence here is not definitive.

4

Generalizations of Kitaev's honeycomb model from braided fusion categories

Contents

Kitaev's exactly solvable spin-$\frac{1}{2}$ model on the honeycomb lattice [39] displays a range of exotic quantum spin liquid phases, both topologically ordered and gapless. When time-reversal symmetry is broken, it supports non-abelian topological order with Ising anyons, which holds promise for fault-tolerant quantum computation [45]. This non-abelian phase features gapless edge modes described by chiral Ising conformal field theories, which may have experimentally detectable signatures [42–44].

Numerous generalizations of Kitaev's honeycomb model have been developed independently, including extensions to higher spin [92–94] and to $\mathbb{Z}_N$ [49, 95, 96]. In this chapter, we take a systematic approach to constructing these generalizations using the fusion surface model framework introduced by Inamura and Ohmori [51], taking braided fusion 1-categories as input.

The resulting 2+1d models possess 1-form symmetries that manifest as mutually commuting plaquette operators. They reduce to Levin-Wen string-nets [48] in a particular limit, and to weakly coupled anyon chains in a different limit. Chiral topological order can occur because of non-commuting terms and explicit time-reversal symmetry breaking, and we provide evidence it does indeed occur.

4.1 Construction and symmetries

We start by reviewing Inamura and Ohmori's fusion surface model construction [51], noting that many interesting cases do not require the general data of a fusion 2-category, but rather only that of a braided fusion 1-category. Thus in essence generalizing the anyon-chain construction to 2+1d requires (at minimum) adding braiding to fusing. We study a Hamiltonian that mirrors the structure of Kitaev's honeycomb model [39], a connection we elaborate on in Section 4.4. By design, it preserves categorical 1-form symmetries and, for generic input categories with complex braiding, likely breaks time-reversal symmetry explicitly.

We denote the input braided fusion 1-category as $\mathcal{B}$ and assume it is unitary, multiplicity-free and self-dual (except for Section 4.5). Mathematically, its condensation completion $\mathrm{Mod}(\mathcal{B})$ defines a fusion 2-category, which serves as a valid input to the fusion surface model construction. The objects of Mod($\mathcal{B}$) are algebra objects $A \in \mathcal{B}$ (see Section 2.2.2), and 1-morphisms between two such algebras A and C form the category of C-A bimodules, denoted ${}_C\mathcal{B}_A$ [97–100]. The fusion 2-category Mod($\mathcal{B}$) is connected, meaning that there exists a 1-morphism between any two objects. In particular, when both algebras correspond to the identity object $0 \in \mathcal{B}$, the bimodule category ${}_0\mathcal{B}_0$ is simply $\mathcal{B}$ itself. Thus, in practice, the resulting lattice model depends only on the data of $\mathcal{B}$ when all surfaces are empty [51].

States in the Hilbert space are fusion trees on the honeycomb lattice,

$$|\{\Gamma_i, \Gamma_{ijk}\}\rangle = \tag{4.1}$$

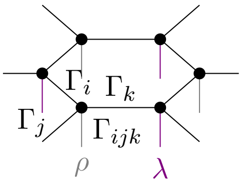

The black edges are labeled by objects $\Gamma_i \in \mathcal{B}$ and the four-valent vertices by morphisms $\Gamma_{ijk} \in \mathrm{Hom}(\Gamma_i \otimes \Gamma_j, \Gamma_k \otimes \rho)$. Following [51], the four-valent vertices are resolved into two trivalent vertices, at the expense of creating a new edge labeled by $\Gamma_{ijk} \in \mathcal{B}$:

$$|\{\Gamma_i, \Gamma_{ijk}\}\rangle = \tag{4.2}$$

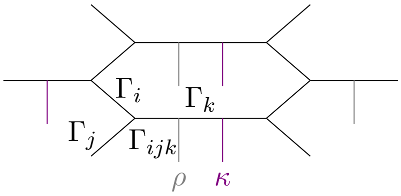

All planar edges Γ_i and Γ_{ijk} on the surface of the fusion tree are dynamical degrees of freedom. As in the anyon chains, the vertical legs are fixed and labeled by the objects $\rho, \kappa \in \mathcal{B}$. In principle, ρ and κ can be different due to the bipartiteness of the honeycomb lattice, but in all examples discussed here, we choose $\kappa = \rho$. From now on, we use the graphical representation (4.2), where all edges are labeled by objects $\Gamma_i, \Gamma_{ijk}, \rho \in \mathcal{B}$. Unless stated otherwise, all vertical lines will be implicitly labeled by ρ.

We consider Hamiltonians of the form depicted below, reminiscent of Kitaev's honeycomb model [39]:

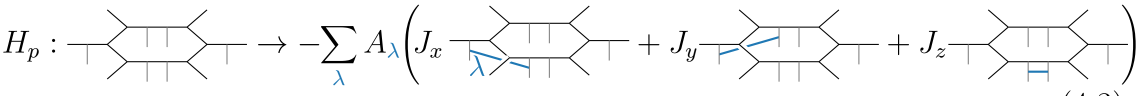

(4.3)

We group the three types of operators around each plaquette p into a single term H_p, so that $H = \sum_p H_p$. All coupling constants J_x, J_y, J_z and weights A_λ are assumed to be real numbers. The Hamiltonian thus yields the simplest 2d analog of the anyon chain. The z-link term with coefficient J_z is precisely the local anyon-chain Hamiltonian $H_{2i-1,2i,2i+1}$ from (2.9) and can be evaluated in the same way. However, because of the geometry of the honeycomb lattice, the J_x and J_y fusion diagrams in Fig. 4.3 are no longer planar diagrams, as the line labeled by λ passes underneath the other lines. The braiding therefore is necessary to define the fusion surface models.

The x-link term with coefficient J_x in Fig. 4.3 can be evaluated as follows:

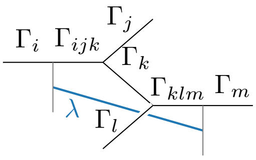

$$= \sum_{\Gamma'_{klm},\Gamma'_l,\Gamma'_k,\Gamma'_{ijk}}$$

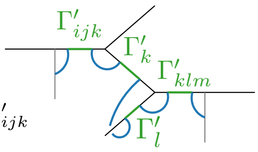

$$= \sum_{\Gamma'_{klm},\Gamma'_l,\Gamma'_k,\Gamma'_{ijk}} [F^{\rho\lambda\Gamma_{klm}}_{\Gamma_m}]_{\rho\Gamma'_{klm}} [F^{\Gamma'_{klm}\lambda\Gamma_l}_{\Gamma_k}]_{\Gamma_{klm}\Gamma'_l} [F^{\Gamma_l\lambda\Gamma_k}_{\Gamma'_{klm}}]_{\Gamma'_l\Gamma'_k}$$

$$\times [F^{\Gamma'_k h\Gamma_{ijk}}_{\Gamma_j}]_{\Gamma_k\Gamma'_{ijk}} [F^{\Gamma'_{ijk}\lambda\rho}_{\Gamma_i}]_{\Gamma_{ijk}\rho} \left(R^{\Gamma_l\lambda}_{\Gamma'_l}\right)^{-1} \sqrt{d_\lambda}$$

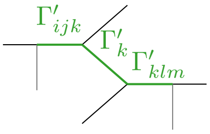

The y-link term with coefficient J_y can be evaluated analogously to the x-link term. In fact, it is related to the x-link term by combined spatial mirror reflection symmetry $\mathcal{P}$ and complex conjugation $\mathcal{K}$:

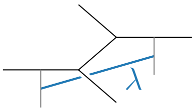

$$= \mathcal{P}\mathcal{K} \left(\quad \right) \mathcal{K}^\dagger \mathcal{P}^\dagger. \tag{4.4}$$

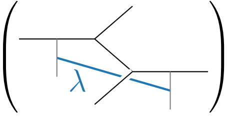

Complex conjugation is necessary to conjugate the braiding phase. The z-link term is invariant under both $\mathcal{P}$ and $\mathcal{K}$. Because the x-link and y-link terms are not real, the fusion surface Hamiltonian breaks time-reversal symmetry unless there exists a unitary matrix U such that $UH_pU^\dagger = (H_p)^*$.

Another new aspect of the 2+1d models is the existence of conserved plaquette operators $B_p^{(\alpha)}$, $\alpha \in \mathcal{B}$ [51]:

$$B_p^{(\alpha)} :$$

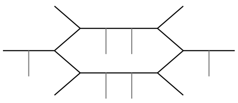

$$\rightarrow$$

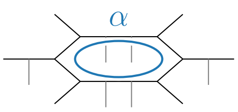

$$=$$

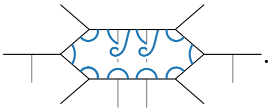

$$. \tag{4.5}$$

In the diagram above, the blue α-lines fused to the lattice can be removed as usual, using the F-symbols and R-symbols of $\mathcal{B}$. We will no longer write out the evaluation explicitly. These plaquette operators commute with the Hamiltonian (4.3) and among themselves. They can be combined into projectors B_p satisfying $B_p^2 = B_p$, where

$$B_p = \sum_{\alpha \in \mathcal{B}} \frac{d_\alpha}{D} B_p^{(\alpha)}, \quad \text{with } D = \sqrt{\sum_\alpha d_\alpha^2}. \tag{4.6}$$

The conserved plaquette operators $B_p^{(\alpha)}$ can be understood as generators of a 1-form symmetry $\mathcal{B}$ acting on the smallest contractible cycles of the lattice. Strictly speaking, true 1-form symmetries must act trivially on contractible loops; when this condition is not met, the symmetry is more accurately described as a 1-symmetry [26, 51, 101]. Nonetheless, we adopt the more common terminology of 1-form symmetry for convenience, bearing in mind that the symmetry action on a contractible loop is only trivial when $B_p = 1$.

On a torus, each non-contractible cycle supports an additional symmetry generator. Graphically, these generators correspond to lines labeled by $\alpha \in \mathcal{B}$ fused into the honeycomb fusion tree from above along a non-contractible loop:

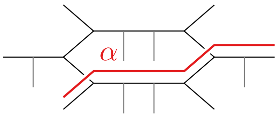

The 1-form symmetry generators commute with each individual term H_p, so any Hamiltonian $H = \sum_p C_p H_p$ with $C_p \in \mathbb{R}$ commutes with them.

The anomalies of 1-form symmetries in the fusion surface models are determined by the F- and R-symbols of the input category $\mathcal{B}$. For example, an invertible 1-form symmetry generated by an object $a \in \mathbb{Z}_N$ is anomalous when the braiding phase $R_1^{aa^{-1}}$ is nontrivial [102, 103]. In such cases, anomaly matching must occur, either via spontaneous symmetry breaking or by realizing a gapless phase. For non-invertible symmetries, generalized anomaly-matching conditions are explored in [103–105].

If the 1-form symmetry associated with $\mathcal{B}$ (or a subcategory thereof) is spontaneously broken, the system enters a topologically ordered phase. In this regime, anyonic excitations labeled by $\alpha \in \mathcal{B}$ can be created at the endpoints of open string operators, much like in the Levin-Wen model (see Section 2.2). When $\mathcal{B}$ is not modular, the full topological order is described by a UMTC of the form $\mathcal{B} \boxtimes \mathcal{C}$, with the fusion category $\mathcal{C}$ accounting for emergent anyons not linked to exact 1-form symmetries [51, 106].

The Hamiltonian does not generically preserve independent 0-form symmetries. Nevertheless, one can construct conserved surface operators $S^{(A)}$ from networks of 1-form symmetry lines labeled by an algebra object $A \in \mathcal{B}$, known as condensation defects [51, 103, 107–109]:

$S^{(A)}$:

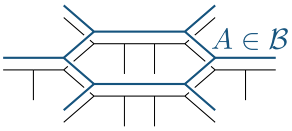

4.2 String-net limit

Next we look at the phase diagram of the fusion surface Hamiltonian (4.3), displayed in Fig. 4.1. Two analytically tractable limits exist within the phase diagram. Here we discuss one such limit, and in Section 4.3 the other.

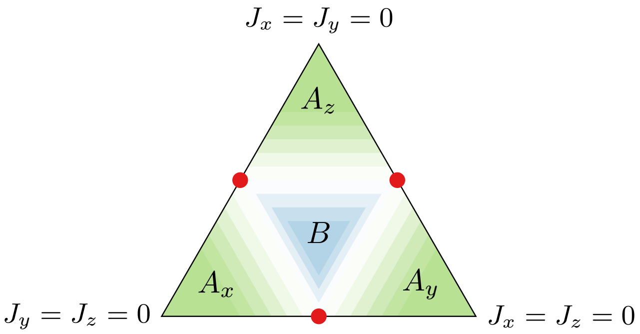

Figure 4.1: Schematic phase diagram of the fusion surface model (2.9) with $J_x+J_y+J_z = 1$. The phases A_x, A_y, A_z are characterized by non-chiral $\mathcal{Z}(\mathcal{B})$ topological order. At the red points, the model reduces to decoupled anyon chains, while in phase B, the chains are weakly coupled.

In the limit $J_z \to \infty$, the Hamiltonian in Fig. 4.3 simplifies to a sum of commuting z-link terms that can be diagonalized independently. Each such term is that of the anyon-chain Hamiltonian $H_{2i-1,2i,2i+1}$ from (2.9), which acts non-diagonally only on even sites. The ground states of the anyon chain in this completely staggered limit were computed in Section 8.1 of [3] for cases where $\mathcal{B}$ is either the $\mathbb{Z}_N$ Tambara-Yamagami category or the $\mathcal{A}_{k+1}$ category, and where $A_\lambda = [F_\rho^{\rho\rho\rho}]_{0\lambda}$ in (2.9) (all our examples satisfy these conditions up to a constant and an overall scaling). There exists one ground state for each object $\nu \in \mathcal{B}$, namely

$$|\nu\tilde{\nu}\nu\rangle =$$

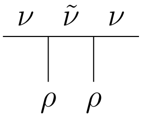

$$\text{with } |\tilde{\nu}\rangle = \frac{1}{\sqrt{d_\nu d_\rho}} \sum_\eta N^\eta_{\nu\rho} \sqrt{d_\eta}\, |\eta\rangle \,.$$

Consequently, the ground state subspace is effectively a honeycomb string-net,

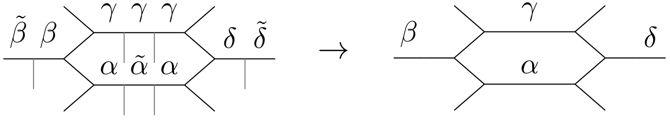

(4.7)

We compute the effective Hamiltonian resulting from including the x-link and y-link terms, and show that it is precisely the Levin-Wen Hamiltonian for topological order [48]. Namely, the lowest-order perturbation theory Hamiltonian in this subspace is the product of x-link and y-link terms around a plaquette:

$$H^{\text{eff}} \sim \frac{J_x^2 J_y^2}{J_z^3} \sum_\lambda A_\lambda$$

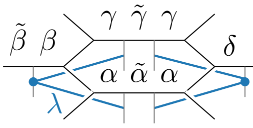

$$\rightarrow \frac{J_x^2 J_y^2}{J_z^3} \sum_\lambda \tilde{A}_\lambda$$

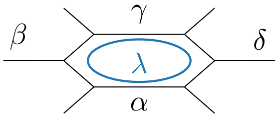

(4.8)

In the first line of (4.8), we must sum over the two resolutions of the four-valent blue vertices,

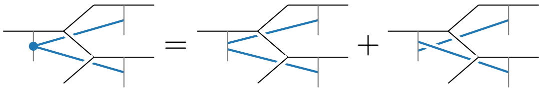

(4.9)

This large-J_z result is straightforward to derive. At first order in perturbation theory, a single J_x or J_y link term changes two z-link states from their ground state $|\nu\tilde{\nu}\nu\rangle$ to an excited state,

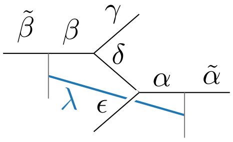

$$= \sum_{\alpha',\beta',\tilde{\alpha}',\tilde{\beta}',\ldots} C_{\alpha',\beta',\tilde{\alpha}',\tilde{\beta}',\ldots}$$

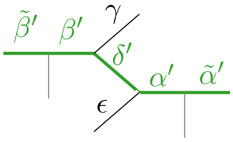

Note that the x-link term changes $\tilde{\alpha} \rightarrow \tilde{\alpha}'$ as $\tilde{\alpha}$ is not necessarily a simple object. The coefficients $C_{\alpha',\beta',\ldots}$ depend on the F-symbols and R-symbols. The overlap between this state and the original one can only be nonzero when $\alpha' = \alpha$, $\beta' = \beta$ and $\delta' = \delta$. In that case, the overlap reduces to

$$\left\langle \tilde{\alpha}' \middle| \tilde{\alpha} \right\rangle \left\langle \tilde{\beta}' \middle| \tilde{\beta} \right\rangle \propto \left(\sum_{\eta} d_\eta [F_\eta^{\rho\lambda\alpha}]_{\rho\alpha} \right) \left(\sum_{\eta} d_\eta [F_\eta^{\rho\lambda\beta}]_{\rho\beta} \right).$$

This follows from the expansion $|\tilde{\alpha}\rangle \propto \sum_{\eta\in\mathcal{B}} N_{\alpha\rho}^{\eta} \sqrt{d_\eta}\, |\eta\rangle$ and the action $[F_\eta^{\rho\lambda\alpha}]_{\rho\alpha'} = [F_\eta^{\rho\lambda\alpha}]_{\rho\alpha}$ of the Hamiltonian on each simple object η in $\tilde{\alpha}$ (and likewise for $\tilde{\beta}$). The overlap vanishes from the symmetry properties of the F-symbols we require (see e.g. [3], and the discussion below):

$$\begin{aligned}
\sum_{\eta} d_\eta [F_\eta^{\rho\lambda\alpha}]_{\rho\alpha} &= \sum_{\eta} d_\eta \sqrt{d_\alpha d_\rho} \begin{bmatrix} \rho & \lambda & \rho \\ \alpha & \eta & \alpha \end{bmatrix} = \sum_{\eta} d_\eta \sqrt{d_\eta d_\rho} \begin{bmatrix} \rho & \rho & \lambda \\ \alpha & \alpha & \eta \end{bmatrix} \\
&= (d_\alpha d_\rho) \sum_{\eta} d_\eta \begin{bmatrix} \rho & \rho & \lambda \\ \alpha & \alpha & \eta \end{bmatrix} \begin{bmatrix} \rho & \rho & 0 \\ \alpha & \alpha & \eta \end{bmatrix} \\
&= (d_\alpha d_\rho) \delta_{0\lambda} N_{\alpha\alpha}^{0} N_{\rho\rho}^{0} = 0 \ \text{ if } \lambda \neq 0.
\end{aligned} \tag{4.10}$$

In the first equality, we write the F-symbol in terms of the tetrahedral symbol, which can be defined graphically as

$$\begin{bmatrix} \alpha & \beta & \gamma \\ \delta & \epsilon & \eta \end{bmatrix} = \frac{1}{\sqrt{d_\alpha d_\beta d_\gamma d_\delta d_\epsilon d_\eta}}$$

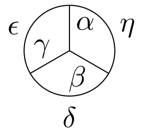

$$= \frac{1}{\sqrt{d_\gamma d_\eta}} [F_\epsilon^{\alpha\beta\delta}]_{\gamma\eta}$$

These symbols possess the symmetries of a tetrahedron, and we exploit these in our derivation of (4.10). In the second equality in (4.10), we employ the column-permutation symmetry of the tetrahedral symbol; see e.g. equation (2.42) in [3]. In the third equality, we use their (2.40) to insert a second tetrahedral symbol at the expense of a numerical factor, and in the fourth, we employ the orthogonality of the tetrahedral symbols in their (2.44). The overlap therefore vanishes for any Hamiltonian (as any term with $\lambda = 0$ is simply a constant, we can simply set $A_0 = 0$ without loss of generality). This vanishing can be easily checked explicity for the Fibonacci fusion category with $\lambda = \eta = \tau$ studied in Section 4.6.

At second order, the product of two adjacent J_x and J_y terms contains a part which acts diagonally on the z-link state that they share (due to λ being self-dual), even though they change the other two z-link states to orthogonal states. In a picture,

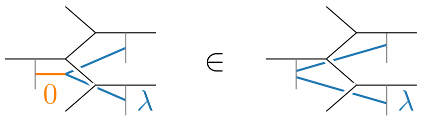

Hence, the lowest-order effective Hamiltonian that preserves the ground-state subspace arises at fourth order, and is the product of two J_x and two J_y terms around one plaquette, as depicted in the first line of (4.8). It contains a contribution that acts diagonally on the z-link states $\left|\beta\tilde{\beta}\beta\right\rangle$ and $\left|\delta\tilde{\delta}\delta\right\rangle$ on the left and right of the plaquette, and a contribution that flips the z-link states $|\alpha\tilde{\alpha}\alpha\rangle$ and $|\gamma\tilde{\gamma}\gamma\rangle$ on the top and bottom to different states $|\alpha'\tilde{\alpha}'\alpha'\rangle$ and $|\gamma'\tilde{\gamma}'\gamma'\rangle$ with the same energy. To show the last statement, we compute the overlap between the z-link acted upon by the J_x and J_y terms and the original z-link state. The new state is given by

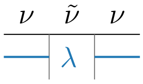

$$= \sum_{\nu',\nu'',\eta} \sqrt{d_\eta} N^{\eta}_{\nu\rho} d_\lambda [F^{\nu''\lambda\rho}_{\eta}]_{\nu\rho} [F^{\rho\lambda\nu'}_{\eta}]^{*}_{\rho\nu}$$

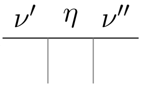

The overlap between the new state and another ground state $|\nu'\tilde{\nu}'\nu'\rangle$ is proportional to

$$\sum_{\eta} d_\eta N^{\eta}_{\lambda\rho} [F^{\nu'\lambda\rho}_{\eta}]_{\nu\rho} [F^{\rho\lambda\nu'}_{\eta}]^{*}_{\rho\nu} = \sum_{\eta} d_\eta N^{\eta}_{\nu\rho} \left| [F^{\rho\lambda\nu'}_{\eta}]_{\rho\nu} \right|^2 > 0.$$

The equality follows from the tetrahedral symmetry of the F-symbol. Hence, the ground states mix at fourth order in perturbation theory. In the ground state subspace, this fourth-order effective Hamiltonian thus acts as a Levin-Wen plaquette operator [48], as sketched in the second line of (4.8). The coefficient $\tilde{A}_\lambda$ may be different from the coefficient A_λ in the first line because one of the two resolutions in (4.9) has an additional braiding phase depending on λ. The Levin-Wen model string-net with edge labels in the fusion category $\mathcal{B}$ realizes non-chiral topological order described by the Drinfeld centre $\mathcal{Z}(\mathcal{B})$ [48, 60]. Therefore the fusion surface model (4.3) also realizes such order in the $J_z \gg J_x, J_y$ limit (denoted as the A_z phase in Fig. 4.1). We expect the same kind of topological order when either J_x or J_y dominate.

4.3 Weakly coupled chains

We now turn to the isolated points highlighted in red in the phase diagram (Fig. 4.1), where the system effectively simplifies to decoupled 1+1d subsystems equivalent to anyon chains. This suggests that the isotropic phase at the center of the diagram is qualitatively described by weakly coupled chains and may realize chiral topological order.

When one coupling, e.g. J_x, is set to zero, the fusion surface model (4.3) reduces to a stack of J_y–J_z chains with local Hamiltonian

$$-\sum_{\lambda} A_\lambda \Bigg(J_y$$

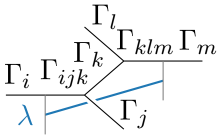

$$+ J_z$$

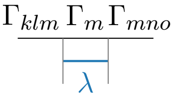

$$\Bigg) \tag{4.11}$$

This Hamiltonian is diagonal in the Γ_j and Γ_l degrees of freedom. If they are all set to the identity object, the J_y–J_z chain is precisely the anyon chain with the usual z-link Hamiltonian, cf. (2.9), and staggered couplings. If not, the Γ_l edges can be moved using F-symbols,

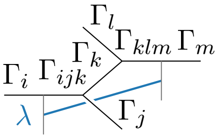

$$= \sum_{\Gamma'_{klm}} [F^{\Gamma_k\Gamma_l\Gamma_m}_{\rho}]_{\Gamma_{klm}\Gamma'_{klm}} \tag{4.12}$$

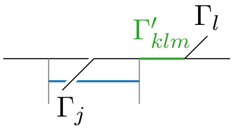

Since the F-symbols are unitary in the lower two indices, moving the Γ_l edge in this manner implements a unitary transformation of the Γ_{klm} edge. Similarly, the Γ_j edges can be shifted using a combination of F-symbols and R-symbols,

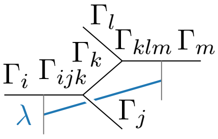

$$= \sum_{\Gamma'_{ijk}} [F^{\Gamma_i\Gamma_j\Gamma_k}_{\rho}]^{-1}_{\Gamma_{ijk}\Gamma'_{ijk}} R^{\Gamma_j\Gamma_{ijk}}_{\Gamma_k} \left(R^{\Gamma_j\Gamma_i}_{\Gamma'_{ijk}}\right)^{-1} \tag{4.13}$$

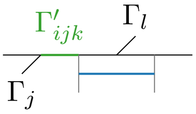

This transformation is also unitary because the R-symbols are unitary as well. By repeating these processes, all Γ_j and Γ_l edges can be moved to the same location, as illustrated below for a J_y–J_z chain of size $L = 4$:

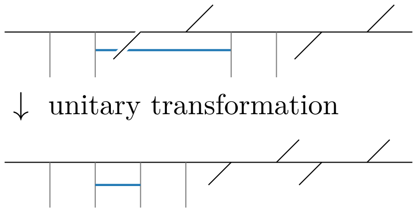

(4.14)

Except for the right-most term, the unitarily transformed Hamiltonian is exactly the anyon chain Hamiltonian. Having been moved together, the Γ_j and Γ_l edges then can be fused together, leading to a sum over objects at this location. For an open chain, taking the location to be the end of the chain amounts to a sum over boundary conditions. The multiplicities in the sum lead to additional degeneracies in the spectrum for each boundary condition. For periodic boundary conditions, only one term in the Hamiltonian differs from the anyon chain. This unitarily transformed Hamiltonian is effectively an anyon chain with a sum over twisted boundary conditions, again with multiplicities. We work out the unitary transformation (4.14) explicitly for the chain constructed from the Ising category in Appendix B.1. As seen there, the degeneracies grow exponentially with the size of the system. These large degeneracies can also be understood as arising from the remnants of plaquette operators $B_p^{(\alpha)}$ or of 1-form symmetry generators $W_l^{(\alpha)}$ along an incontractible cycle l, acting as

$B_p^{(\alpha)}$:

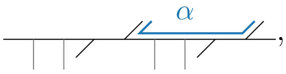

,

$W_l^{(\alpha)}$:

Once the eigenvalues of the largest commuting set of these operators are fixed, the $J_z = 0$, $J_y = J_z$ model reduces to the anyon chain in the corresponding background fields. In many interesting cases including the examples we study, the continuum limit yields a conformal field theory.

Along the $J_y = J_z$, $J_x = 0$ line, the fusion surface model (4.3) is expected to be gapless and characterized by L_y distinct 1+1d theories, which in the examples we study are CFTs. Upon introducing a small coupling $J_x \ll J_y = J_z$ between neighbouring critical chains, the fusion surface model realizes a coupled-wire system [110, 111]. When time-reversal symmetry is broken, chiral topological order is possible, as illustrated by examples in Sections 4.5 and 4.6.

4.4 Kitaev's honeycomb model as an Ising fusion surface model

The simplest non-trivial example of a fusion surface model of the form (4.3) is built from the Ising category, and its Hamiltonian is unitarily equivalent to the well-known Kitaev honeycomb model [51]. We review and expand upon this result to set the stage for its generalizations in Sections 4.5 and 4.6. Under a magnetic field perturbation, Kitaev's honeycomb model is known to exhibit chiral Ising topological order [39]. By representing a related perturbation graphically we demonstrate explicitly that fusion surface models realize chiral topological order, as anticipated but not proven in [51].

4.4.1 Constructing Kitaev's honeycomb model from the Ising category

Kitaev [39] proposed an exactly solvable model of qubits on the vertices of a honeycomb lattice, with interactions between adjacent qubits depending on the direction of the connecting link, see Fig. 4.2. The Hamiltonian is

$$H^{\text{Kitaev}} = - J_x \sum_{a,b\in \text{x-link}} X_a X_b - J_y \sum_{a,c\in \text{y-link}} Y_a Y_c - J_z \sum_{b,d\in \text{z-link}} Z_b Z_d, \tag{4.15}$$

where X, Y and Z denote the Pauli matrices. Conserved plaquette operators commute with the Hamiltonian (4.15) and among themselves,

$$B_p = Y_1 Z_2 X_3 Y_4 Z_5 X_6. \tag{4.16}$$

The physics of Kitaev's honeycomb model is well understood, as it can be mapped to free fermions when all plaquette operators are fixed to $B_p = \pm 1$ [39]. Its phase diagram is depicted on the right of Fig. 4.2. In the anisotropic coupling limits, the effective Hamiltonian in perturbation theory reduces to the toric code Hamiltonian and thus realizes doubled $\mathbb{Z}_2$ topological order in the phases A_x, A_y and A_z. The phase B near the isotropic point is gapless.

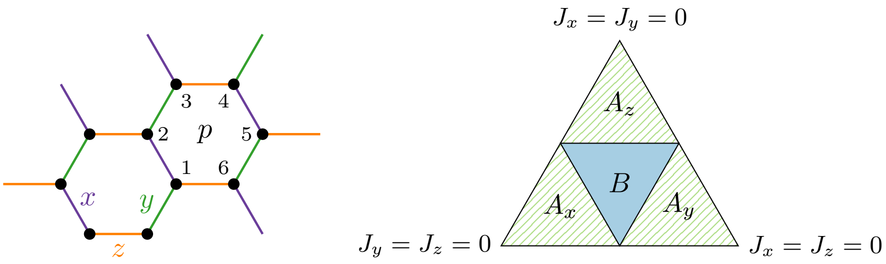

Figure 4.2: Left: Kitaev's honeycomb model with qubits on the vertices and interactions depending on the direction of the link, right: phase diagram for $J_x + J_y + J_z = 1$, exhibiting gapped phases A_x, A_y, A_z and a gapless phase B [39].

Remarkably, Kitaev's honeycomb model is unitarily equivalent to the fusion surface model built from the Ising category [51]. The Ising category consists of three objects $\{0, 1, \sigma\}$ with the identity object denoted as 0. The non-abelian object σ has $d_\sigma = \sqrt{2}$ and obeys the fusion rules $\sigma \otimes \sigma = 0 \oplus 1$ and $\sigma \otimes 1 = \sigma$. In the fusion surface model construction, we pick $\rho = \sigma$ so that all vertical legs of the fusion tree are labeled by σ. Half of the planar edges Γ_i are also labeled by σ, with the remaining planar edges representing the dynamical degrees of freedom $\Gamma_{ijk} \in \{0, 1\}$ of the quantum state:

$|\{\Gamma_{ijk}\}\rangle =$

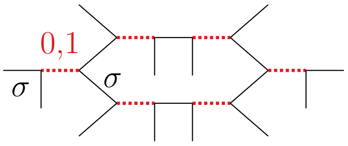

(4.17)

In this and all subsequent fusion diagrams, the thin black lines are labeled by σ, and the red dotted lines are labeled by $\{0, 1\}$. Consequently, the Hilbert space is spanned by states of qubits on a honeycomb lattice. The action of the local Hamiltonian on the states (4.17) is given by

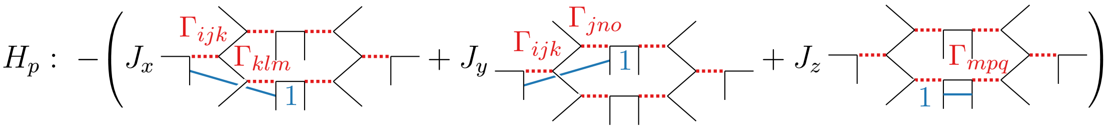

(4.18)

Because of the fusion rule $\sigma \otimes 1 = \sigma$, the Hamiltonian does not change the σ labels on half of the planar edges, consistent with these labels being fixed initially.

The x-link, y-link and z-link terms in the local Hamiltonian (4.18) can be evaluated as discussed in Section 4.1, with detailed calculations provided in Appendix B.2. The z-link term evaluates to $Z_{klm}Z_{mpq}$ just as half of the terms in the Ising chain, and the x-link and y-link terms yield $-Y_{klm}X_{ijk}$ and $Y_{ijk}X_{jno}$ respectively. Thus, the full fusion surface Hamiltonian $H = \sum_p H_p$ with H_p as defined in (4.18) is equal to

$$H = -J_x \sum_{b,a \in \text{x-link}} (-Y_b X_a) - J_y \sum_{a,c \in \text{y-link}} Y_a X_c - J_z \sum_{b,d \in \text{z-link}} Z_b Z_d. \tag{4.19}$$

After a unitary rotation $e^{i\pi Z/4}$ of all qubits on one sublattice of the bipartite honeycomb lattice, the Hamiltonian (4.19) becomes Kitaev's honeycomb model (4.15).

By construction, the fusion surface model (4.19) has conserved plaquette operators $B_p^{(1)}$ as defined in (4.5),

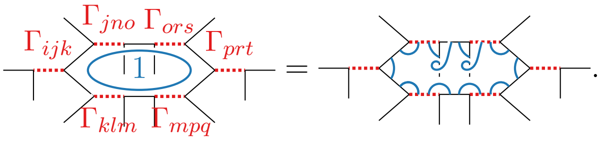

(4.20)

In operator form, (4.20) yields

$$B_p^{(1)} = -X_{klm} Z_{ijk} Y_{jno} Y_{ors} Z_{prt} X_{mpq}.$$

Equivalently, $B_p^{(1)}$ is the product of all terms in the Hamiltonian around the plaquette. After the unitary rotation described above, this is precisely the conserved plaquette operator (4.16) of Kitaev's honeycomb model.

The Ising fusion surface model (4.19) on a torus is also invariant under a $\mathbb{Z}_2$ 1-form symmetry along the incontractible cycles,

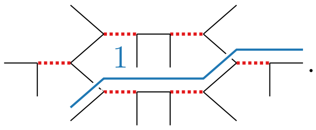

In operator form, this is the product of the terms in the Hamiltonian along the path, here leading to alternating X and Y matrices,

$$\dots Y_{klm} X_{mpq} Y_{prt} \dots$$

It follows immediately that the 1-form symmetry is fermionic as it inherits the braiding phase $R_0^{11} = -1$ of the input category. Open strings of this 1-form symmetry create fermionic $\mathbb{Z}_2$ anyons at their endpoints when the ground state is gapped.

For general fusion surface models, we showed in Section 4.2 that they reduce to a Levin-Wen string-net in the large J_z limit. The Ising fusion surface model discussed here reduces in fact to the $\mathbb{Z}_2$ toric code because its Hamiltonian (4.19) does not feature the σ-line. More explicitly, as $J_z \to \infty$, there are two ground states $Z_a = Z_b = \pm 1$ on each z-link. The lowest order Hamiltonian acting in this ground-state subspace is the following,

$$H^{\text{eff}} \sim \frac{J_x^2 J_y^2}{J_z^3}$$

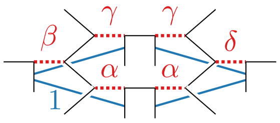

$$+ \dots \to \frac{J_x^2 J_y^2}{J_z^3}$$

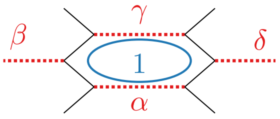

This effective Hamiltonian does not change the location of the qubits on the string-net, as it does not contain the σ-loop, and is therefore equivalent to the toric code rather than the Ising string-net.

4.4.2 Chiral Ising topological order from a magnetic field perturbation

The phase B in the center of the phase diagram in Fig. 4.2 is gapless but becomes chiral Ising topological order once time-reversal symmetry is broken [39, 112]. In this regime, the system is gapped on a torus or infinite cylinder, exhibiting three ground states corresponding to the simple objects of the Ising category. On an open strip, however, the system becomes gapless, with chiral Ising CFTs propagating along the top and bottom edges.

Time-reversal symmetry can be broken explicitly by adding a magnetic field perturbation V to Kitaev's honeycomb Hamiltonian (4.15), given by

$$V = -\sum_j (h_x X_j + h_y Y_j + h_z Z_j).$$

This perturbation V does not commute with the conserved plaquette operators (4.16). In perturbation theory, the lowest-order effective perturbation that commutes with the plaquette operators is [39]

$$V^{(3)}_{\text{eff}} \sim \frac{h_x h_y h_z}{J^2} \sum_{j,k,l} X_j Y_k Z_l. \tag{4.21}$$

The effective perturbation $V^{(3)}_{\text{eff}}$ consists of products of adjacent link terms in the Hamiltonian, which necessarily can be represented in the fusion surface framework.

$$V^{(3)}_{\text{eff}} \sim \frac{h_x h_y h_z}{J^2}$$

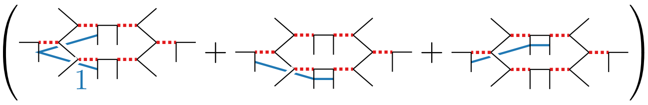

Kitaev [39] computed the spectrum of the Hamiltonian with the time-reversal symmetry breaking $V^{(3)}_{\text{eff}}$ perturbation explicitly using free-fermion methods and showed that it exhibits chiral Ising topological order. Thus, the Ising fusion surface model (4.18) with the perburbation (4.21) serves as an example of a fusion surface model with chiral topological order. We thus confirm that fusion surface models can exhibit chiral topological order, as anticipated in [51].

4.4.3 Twist defects

Another interesting point is the interpretation of the topological σ-line fused to the honeycomb lattice from above. The σ-line does not act as a 1-form symmetry because it changes the location of the qubits on the honeycomb fusion tree. Nonetheless, a closed σ-loop of any length commutes with the Hamiltonian and can thus be interpreted as a 1-form duality mapping between different disconnected sectors of the Ising fusion surface model Hilbert space. For example, fusing a σ-loop to one plaquette maps Kitaev's honeycomb model to a model with the following modified plaquette:

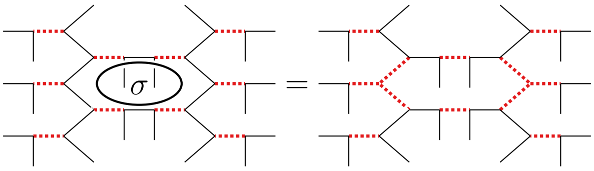

(4.22)

The lattice of qubits is different in the right picture, and also the terms in the Hamiltonian change. For instance, the z-link term changes from a $Z_{klm}Z_{mpq}$ interaction in to an X_m interaction, reminiscent of the Kramers-Wannier duality in the Ising chain. This 1-form duality $D^{(\sigma)}$ is non-invertible as it obeys the same fusion algebra $(D^{(\sigma)})^2 = \mathbb{I} + D^{(1)}$ as the σ-object, with $D^{(1)}$ denoting the $\mathbb{Z}_2$ 1-form symmetry. The fusion relation above implies that the 1-form duality does not implement a simple one-to-one mapping of the energy spectrum, as it annihilates states in the $D^{(1)} = -1$ sector, as with Kramers-Wannier duality in 1+1 dimensions [3, 23, 64].

Open σ-strings ought to create twist defects instead of anyons. Twist defects, introduced in the context of the toric code by Bombin [113], are located at the endpoints of lattice dislocations. Petrova, Mellado and Tchernyshyov [114, 115] explored lattice dislocations and twist defects in the gapped phase of Kitaev's honeycomb model. In the following, we review their results and compare them to the action of the open σ-string in the fusion surface model.

In the anisotropic phase, the ground state is in the $B_p^{(1)} = +1$ sector, with low-energy excitations corresponding to flipped plaquettes $B_p^{(1)} = -1$. These

$\mathbb{Z}_2$ vortex excitations come in two flavors, e and m, which live on alternating rows of the honeycomb lattice:

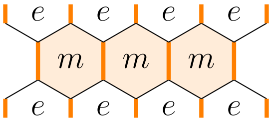

Here the strong z-bonds are represented by the thick orange lines and the weak x- and y-bonds by the thin black lines. At low energies, only vortices in the same row can be created or annihilated pairwise. They can move within their row or hop to the next-nearest row of the same vortex type. The creation of $f = e \otimes m$ anyons is effectively forbidden at low energies. When the number of rows is odd, e and m plaquettes cannot be consistently defined, reducing the ground state degeneracy on a torus from four to two.

8-2 lattice dislocations are created by removing certain link terms in the Hamiltonian, leading to defect sites involved in only two link terms instead of three:

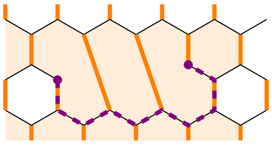

The two twist defect sites, which lack one weak bond each, are indicated by violet circles. The dashed line represents the branch cut, which disrupts the vortex flavor pattern. Each pair of dislocations encodes one nonlocal qubit, which increases the ground state degeneracy by a factor of two. For $n \geq 1$ dislocation pairs on a torus with an even number of rows, the ground state degeneracy increases to 2^{n+1} (the first dislocation pair does not affect the ground state degeneracy because the branch cut renders the e and m flavors indistinguishable). This demonstrates that the quantum dimension of the dislocation defect is $\sqrt{2}$, consistent with the σ object in the Ising category. Although twist defects are fundamentally different from the intrinsic anyonic excitations [116], they can still be leveraged for topological quantum computation, particularly through measurement-based approaches [117].

In the Ising fusion surface model (4.18), fusing an open σ-string to the lattice relocates the qubits along its path and creates twist defects at the endpoints:

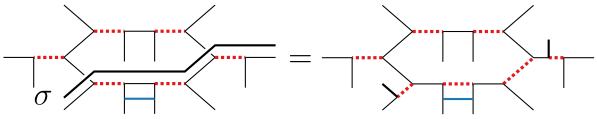

(4.23)

The twist defects are the thick black lines added to the fusion tree, and by definition they obey the same fusion and braiding rules as the Ising anyon. The σ-string is topological away from its endpoints, similar as the branch cut line. The difference to the lattice dislocations studied in [114, 115] is that fusing the σ-string to the lattice not only alters the positions of the term in the Hamiltonian but also modifies their operator form, as illustrated in (4.22).

4.5 $\mathbb{Z}_N$ generalization of Kitaev's honeycomb model

Starting from the $\mathbb{Z}_N$ Tambara-Yamagami category for odd $N > 2$, we build a $\mathbb{Z}_N$-symmetric fusion surface model generalizing Kitaev's honeycomb model. This fusion surface model turns out to be closely related to the $\mathbb{Z}_N$ generalization proposed by Barkeshli et al. [49]. A coupled-wire analysis suggests chiral parafermion topological order occurs in the $\mathbb{Z}_3$ model with additional and appropriately tuned interactions [49]. Our numerical studies of the entanglement spectrum provide evidence that this chiral parafermion topological order persists even when the interactions are not fine-tuned.

4.5.1 Constructing the Hamiltonian from the G-crossed braided $TY(\mathbb{Z}_N)$ category with odd N

The $\mathbb{Z}_N$ Tambara-Yamagami fusion categories [118] are generalizations of the Ising category ($N = 2$) to categories with N abelian objects. We assume odd N here to use the F-symbols and R-symbols found in Section XI.G.2 in [52]. The abelian objects are labeled by integers h modulo N, and their fusion rules are the group multiplication rules of $\mathbb{Z}_N$,

$$h \otimes g = [h + g]_N \quad \forall h, g \in \{0, 1, \ldots, N - 1\},$$

with addition modulo N on the right hand side. This category also contains a non-abelian object σ with quantum dimension $d_\sigma = \sqrt{N}$ and fusion rules

$$\sigma \otimes h = h \otimes \sigma = \sigma, \quad \sigma \otimes \sigma \ = \bigoplus_{h=0}^{N-1} h.$$

While σ is always self-dual, the abelian objects are no longer self-dual for $N > 2$, and so their lines in the fusion diagrams carry arrows. Charge conjugation acts on the abelian objects as $h \to h^{-1} = N - h$, i.e. reverses their direction.

The $\mathbb{Z}_N$ Tambara-Yamagami category is a G-graded fusion category $\mathcal{C}_G = \mathcal{C}_\mathbf{0} \oplus \mathcal{C}_\mathbf{1}$, with G being the $\mathbb{Z}_2$ charge conjugation symmetry. The grading structure is respected by the fusion rules, i.e. $a_\mathbf{g} \otimes b_\mathbf{h} = \oplus_{c_\mathbf{gh}} N^c_{ab} c_\mathbf{gh}$ for $g, h \in G$. The trivially graded component $\mathcal{C}_\mathbf{0} = \mathbb{Z}_N^{(r)}$ contains the abelian objects, while other graded component $\mathcal{C}_\mathbf{1}$ contains only the non-abelian object σ.

A crucial difference between the $\mathbb{Z}_N$ Tambara-Yamagami and Ising categories is that with $N > 2$ the former admits only G-crossed braiding [119, 120]. The braiding of the abelian anyons depends on an integer parameter $r = 1, \dots, N-1$,

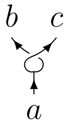

$= R^{bc}_a$

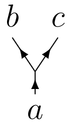

$$, \quad R^{ab}_{[a+b]_N} = e^{i\frac{2\pi}{N}rab} \text{ for } a, b \in \mathbb{Z}_N.$$

Their topological twist factors are given by

$$\theta_a \equiv (R_0^{aa^{-1}})^{-1} = e^{i\frac{2\pi}{N}ra^2} \text{ for } a \in \mathbb{Z}_N. \tag{4.24}$$

Graphically, the G-crossed braiding between the σ object and the abelian objects can be depicted as [52]

$R^{\sigma h} =$

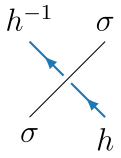

$, \quad R^{h\sigma} =$

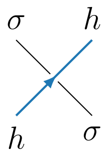

The σ-line thus applies the charge conjugation group action to the abelian object h when it crosses over their wordline. Conversely, when the σ-line undercrosses the h-line, nothing happens to the h-line. The R-symbols involving σ are given by [52]

$$R^{\sigma a}_\sigma = R^{a\sigma}_\sigma = (-1)^{ra} e^{\frac{-i\pi r}{N}a^2}. \tag{4.25}$$

For oriented lines, the F-symbols are defined as

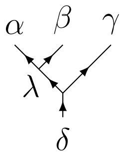

$$= \sum_{\kappa} \left[F^{\alpha\beta\gamma}_{\delta}\right]_{\kappa\lambda}$$

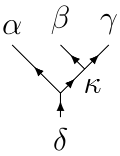

The non-trivial F-symbols of the Tambara-Yamagami category involve σ,

$$\left[F^{a\sigma b}_{\sigma}\right]_{\sigma\sigma} = \left[F^{\sigma a \sigma}_{b}\right]_{\sigma\sigma} = e^{\frac{2\pi i r}{N}ab}, \quad \left[F^{\sigma\sigma\sigma}_{\sigma}\right]_{ab} = \frac{1}{\sqrt{N}} e^{\frac{-2\pi i r}{N}ab} \text{ for } a, b \in \mathbb{Z}_N.$$

We define the local $\mathbb{Z}_N$ fusion surface Hamiltonian H_p to act as

$-J_x$
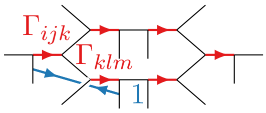

$- J_y$
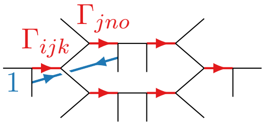

$- J_z$
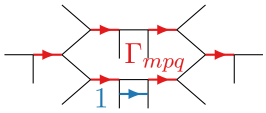

$+$ h.c. (4.26)

The degrees of freedom are now N-state qudits $\Gamma_{ijk} \in \{0, 1, \ldots, N-1\}$, denoted by red directed lines. When the blue line labeled by the 1-object undercrosses the σ-edge in the x-link and y-link term in (4.26), it changes its direction due to the G-crossed braiding. Apart from this important difference, the evaluation of the fusion diagrams (4.26) closely follows the calculation in Appendix B.2. The z-link term evaluates to $Z^{r\dagger}_{klm} Z^{r}_{mpq}$, and the x-link and y-link terms to $X_{ijk} Z^{r}_{klm} X^{\dagger}_{klm}$ and $Z^{r}_{ijk} X_{ijk} X^{\dagger}_{jno}$ respectively, each multiplied by additional complex phases. Here Z and X are the $\mathbb{Z}_N$ clock and shift operators satisfying $XZ = \omega ZX$, with $\omega = e^{\frac{2\pi i}{N}}$. Explicitly,

$$Z = \begin{pmatrix} 1 & 0 & \ldots & 0 \\ 0 & \omega & \ldots & 0 \\ \vdots & \vdots & \ddots & \vdots \\ 0 & 0 & \ldots & \omega^{N-1} \end{pmatrix}, \quad X = \begin{pmatrix} 0 & 1 & 0 & \ldots & 0 \\ 0 & 0 & 1 & \ldots & 0 \\ \vdots & \vdots & \vdots & \ddots & \vdots \\ 1 & 0 & 0 & \ldots & 0 \end{pmatrix}.$$

The resulting $\mathbb{Z}_N$ fusion surface Hamiltonian is thus:

$$\begin{aligned} H = &- J_x \sum_{b,a \in \text{x-link}} (-1)^{rN} e^{-\frac{i\pi r}{N}} X_a Z^r_b X^{\dagger}_b - J_y \sum_{a,c \in \text{y-link}} (-1)^{rN} e^{\frac{i\pi r}{N}} Z^r_a X_a X^{\dagger}_c \\ &- J_z \sum_{b,d \in \text{z-link}} Z^{r\dagger}_b Z^r_d + \text{h.c.} \end{aligned} \tag{4.27}$$

The complex phases in the x-link and y-link terms (4.27) are such that the Hamiltonian is invariant under unitary charge conjugation C, acting as

$$CXC^{\dagger} = X^{\dagger}, CZC^{\dagger} = Z^{\dagger}, \ C(XZ)C^{\dagger} = X^{\dagger}Z^{\dagger}, \quad \text{with } C = \begin{pmatrix} 1 & 0 & 0 \\ 0 & 0 & 1 \\ 0 & 1 & 0 \end{pmatrix}. \tag{4.28}$$

Graphically, the charge conjugated terms are obtained by reversing the direction of the interaction (blue) lines in (4.26), and are precisely the hermitian conjugate terms. After a unitary transformation $X_b^\dagger \to (-1)^{rN} e^{\frac{i\pi r}{N}} Z_b^{r\dagger} X_b^\dagger$, followed by charge conjugation – both only applied to one sublattice – Eq. (4.27) becomes

$$H = -\,J_x \sum_{b,a\in \text{x-link}} X_a X_b - J_y \sum_{a,c\in \text{y-link}} \omega^r Z_a^r X_a Z_c^r X_c - J_z \sum_{b,d\in \text{z-link}} Z_b^r Z_d^r \,+\, \text{h.c.} \tag{4.29}$$

The $r=1$ and $r=N-1$ Hamiltonians have the same spectrum, as they are related by complex conjugation.

The $r = N-1$ case of (4.29) is closely related to the Hamiltonian

$$H^{\mathbb{Z}_N} = -\,J_x \sum_{b,a\in \text{x-link}} X_a X_b - J_y \sum_{a,c\in \text{y-link}} (X_a Z_a^\dagger)(X_c Z_c^\dagger) - J_z \sum_{b,d\in \text{z-link}} Z_b Z_d \,+\, \text{h.c.} \tag{4.30}$$

proposed in [49] as a $\mathbb{Z}_N$ generalization of Kitaev's honeycomb model. The only distinction is the complex phase ω^r in the y-link term guaranteeing charge conjugation invariance. The resulting finite-size spectra for $N=3$ are slightly different. However, with DMRG on an infinite cylinder, their energy and entanglement spectra (cf. Fig. 4.3) agree. Therefore we expect the $N=3$ models (4.30) and (4.29) to exhibit the same topologically ordered phases.

The $r \in \{1, N-1\}$ fusion surface models (4.29) and the model (4.30) break time-reversal symmetry explicitly [49], as there is no unitary matrix U such that $UHU^\dagger = H^*$. For such a unitary U to exist for arbitrary coupling constants, it would need to map $Z \to Z^\dagger$ without changing X. However, such a mapping would change the commutation relations between X and Z, making it impossible to implement by any unitary matrix.

4.5.2 Anomalous $\mathbb{Z}_N$ 1-form symmetry

Plaquette operators $B_p^{(1)}$ that commute with the fusion surface model Hamiltonian (4.27) and among themselves are created by fusing a 1-loop to the inside of a plaquette,

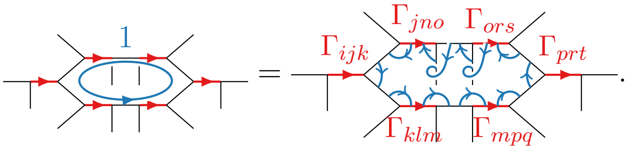

(4.31)

Note that the blue 1-loop does not change its direction because it overcrosses the σ-edges. When the Tambara-Yamagami braiding parameter is set to $r=1$, the plaquette operator is

$$B_p^{(1)} = \omega X_{klm} Z_{ijk} (Z X^\dagger)_{jno} (X^\dagger Z^\dagger)_{ors} Z^\dagger_{prt} X_{mpq},$$

which is the product of the terms in the Hamiltonian (4.26) around the plaquette (with the correct chiralities).

On a torus, additional $\mathbb{Z}_N$ 1-form symmetry generators arise by fusing lines labeled by abelian objects from above into the honeycomb lattice along non-contractible cycles. This 1-form symmetry is anomalous, meaning that endpoints of open strings have nontrivial exchange statistics. The exchange statistics for the model (4.30) were computed explicitly in [95, 121, 122], using the method described in [123]. The results are different, with $\theta_1 = \omega^2$ in [95] and $\theta_1 = \omega$ in [121, 122], as the models are slightly different, with the y-link term containing XZ in the former but $XZ^\dagger$ in the latter. The fusion surface model construction directly yields the exchange statistics factor of the 1-form symmetry line a to be the topological twist factor $\theta_a = \omega^{ra^2}$ (4.24) of the input category. This nontrivial statistics factor signals a 't Hooft anomaly, and anomaly matching requires the $\mathbb{Z}_N^{(r)}$ 1-form symmetry to be spontaneously broken or the phase to be gapless (as discussed in Section 4.1). When the 1-form symmetry is broken, the ground state is topologically ordered and its excitations include $\mathbb{Z}_N^{(r)}$ anyons.

Similar to the $\mathbb{Z}_2$ honeycomb model (cf. Section 4.4.3), the σ object does not give rise to a 1-form symmetry. Instead, it generates a topological twist defect line (when it is open) or a non-invertible 1-form duality (when it is closed). For example, when a σ-loop is fused to one plaquette as depicted in (4.22), the z-link and y-link terms on this plaquette are modified to $Z_{klm} Z^\dagger_{mpq} \to X_m$ and $Z_{mpq} X_{mpq} X^\dagger_{prt} \to Z^\dagger_m X_p Z_r X^\dagger_{prt}$ respectively (for $r = 1$).

4.5.3 Weakly coupled chains limit of the $\mathbb{Z}_3$ honeycomb model

The phase diagram of (4.30) for $N = 3$ was studied in [49] and more recently numerically in [95, 124]. Its general structure is believed to be similar to the phase diagram of the $\mathbb{Z}_2$ model in Fig. 4.2. In the anisotropic limits, the effective Hamiltonian in perturbation theory is the $\mathbb{Z}_3$ toric code, and the model is characterized by doubled $\mathbb{Z}_3$ topological order [49]. The nature of the phase near the isotropic point $J_x = J_y = J_z$ is not yet fully established. Due to the time-reversal breaking in the $\mathbb{Z}_3$ honeycomb Hamiltonian (4.30), chiral topological order is likely. Numerical results support this, indicating a gapped bulk with chiral edge modes [95, 124] and a ground state that breaks time-reversal symmetry [125].

To better understand this phase, we rephrase the coupled-wire analysis of [49] in the fusion surface model picture. When J_x is set to zero, the $\mathbb{Z}_3$ honeycomb Hamiltonian reduces to decoupled J_y-J_z chains, which are unitarily related to the anyon chain with twisted boundary conditions, as discussed in Section 4.3. The anyon chain built from the $\mathbb{Z}_3$ Tambara-Yamagami category is the $\mathbb{Z}_3$ Potts chain:

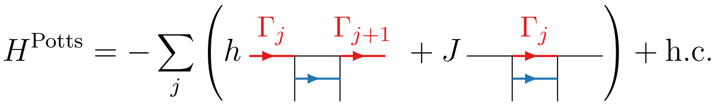

$$= -h \sum_j Z_j^\dagger Z_{j+1} - J \sum_j X_j + \text{h.c.}$$

When $J_y = J_z$, the J_z-J_y chain is critical and described by the Potts CFT [49]. The J_x term which couples neighbouring chains can be rewritten in terms of left and right lattice parafermion operators $\hat{\alpha}_{L,i}$ and $\hat{\alpha}_{R,i}$, represented as

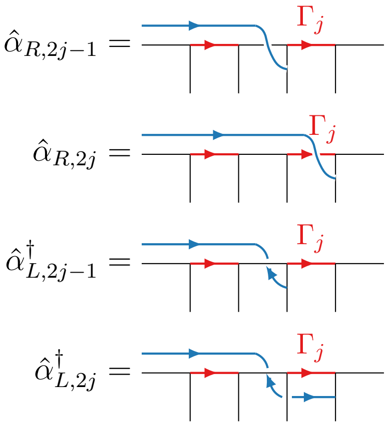

$$\begin{aligned}
\hat{\alpha}_{R,2j-1} &= \left(\prod_{k=1}^{j-1} X_k\right) \omega Z_j \\
\hat{\alpha}_{R,2j} &= \left(\prod_{k=1}^{j-1} X_k\right) X_j Z_j \\
\hat{\alpha}^\dagger_{L,2j-1} &= \left(\prod_{k=1}^{j-1} X_k\right) \omega^2 Z_j^\dagger \\
\hat{\alpha}^\dagger_{L,2j} &= \left(\prod_{k=1}^{j-1} X_k\right) X_j Z_j^\dagger .
\end{aligned} \tag{4.32}$$

Apart from an overall complex phase, these definitions agree with those in [49]. The lattice parafermions commute with the Hamiltonian away from their endpoints and are discretely holomorphic current operators [126–129]; also see Section 4.7. Because the J_z-J_y chains can be mapped to Potts chains, they contain lattice parafermions with a similar visualization. The J_x coupling, in terms of the lattice parafermions of the J_z-J_y chains, is given by

$$H^x_{ij}:$$

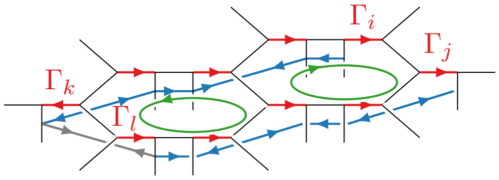

$$+\ \text{h.c.} \tag{4.33}$$

$$= H^x_{kl}\left(B^{(1)}_{p_1}B^{(1)\dagger}_{p_2}\dots\right)\hat{\alpha}^\dagger_{R,2i}\hat{\alpha}_{L,2j-1}\ +\ \text{h.c.}.$$

Here H^x_{kl} is another x-link term that can be chosen to be outside of the region in which the Hamiltonian acts, allowing it to be set to a constant. The product goes over all plaquette operators located between H^x_{kl} and H^x_{ij} and can be set to one in the ground state sector where $B^{(1)}_p = 1$ on all plaquettes. In this sector, the honeycomb Hamiltonian is quadratic in the lattice parafermions [49]:

$$\begin{aligned} H &= \sum_{n=1}^{L_y} H^{(n)}_{1\text{d}} - J_x\sum_{j,n}\left(\hat{\alpha}^{(n+1)\dagger}_{R,2j}\hat{\alpha}^{(n)}_{L,2j-1} + \text{h.c.}\right), \\ H^{(n)}_{1\text{d}} &= \sum_j\Big(-J_y\omega\hat{\alpha}^{(n)\dagger}_{R,2j}\hat{\alpha}^{(n)}_{R,2j-1} - J_z\omega^2\hat{\alpha}^{(n)\dagger}_{R,2j}\hat{\alpha}^{(n)}_{L,2j+1}\ +\ \text{h.c.}\Big). \end{aligned} \tag{4.34}$$

In the above equation, $H^{(n)}_{1\text{d}}$ is the Hamiltonian of the J_z-J_y chain that can be mapped to the Potts chain, and the J_x interchain coupling is written in terms of the lattice parafermions as derived graphically in (4.33).

When the Potts chain is critical, the lattice parafermions contain the (anti-)holomorphic parafermion fields ψ, $\bar{\psi}$ of the Potts CFT, but also a non-holomorphic operator [130],

$$\begin{aligned} \hat{\alpha}_{R,j} &\sim c_1\bar{\psi} + c_2(-1)^j\Phi_{\epsilon\bar{\sigma}}, \\ \hat{\alpha}_{L,j} &\sim d_1\psi + d_2(-1)^j\Phi_{\sigma\bar{\epsilon}}. \end{aligned}$$

The parafermion field ψ with scaling dimensions $(h,\bar{h}) = (\frac{2}{3},0)$ mixes with the operator $\Phi_{\sigma\bar{\epsilon}}$ with $(h,\bar{h}) = (\frac{1}{15},\frac{2}{5})$ because they have the same conformal spin $h-\bar{h}$

modulo integers. Therefore, the J_x interchain coupling in (4.34) can be expanded as

$$\begin{aligned} H^{\text{inter}} &\sim \left(c_1\bar{\psi}^\dagger + c_2\Phi_{\epsilon\bar{\sigma}^\dagger}\right)^{(n+1)}\left(d_1\psi - d_2\Phi_{\sigma\bar{\epsilon}}\right)^{(n)} \\ &\sim c_1 d_1\bar{\psi}^\dagger\psi - c_2 d_2\Phi_{\epsilon\bar{\sigma}^\dagger}\Phi_{\sigma\bar{\epsilon}} \end{aligned} \tag{4.35}$$

The mixed terms $\bar{\psi}^\dagger\Phi_{\sigma\bar{\epsilon}}$ and $\Phi_{\epsilon\bar{\sigma}^\dagger}\psi$ in (4.35) are odd under $\mathcal{PT}$ [111] and therefore forbidden. If the interchain coupling only contained the $\bar{\psi}^\dagger\psi$ fields, the model would realize chiral parafermion topological order $\mathbb{Z}_3 \boxtimes \text{Fib}$ with gapless Potts CFT edge modes [111]. As noted in [49], the other CFT fields present in (4.35) can be tuned away by adding additional interactions to the honeycomb model so that

$$\tilde{H}^{\text{inter}} = -J_x \sum_j \Big(\left(\hat{\alpha}^{(n+1)\dagger}_{R,2j} + \hat{\alpha}^{(n+1)\dagger}_{R,2j-1}\right)\left(\hat{\alpha}^{(n)}_{L,2j-1} + \hat{\alpha}^{(n)}_{L,2j-2}\right) + \text{ h.c.}\Big). \tag{4.36}$$

In the fusion surface model construction, the modified fine-tuned interaction term (4.36) can be depicted as

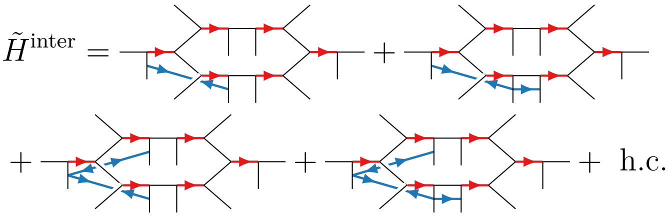

(4.37)

Hence, the $\mathbb{Z}_3$ fusion surface model with the coupling (4.36) instead of the J_x term realizes chiral parafermion topological order. The fine-tuned interchain coupling (4.36) also is realized in a triangular-lattice Hamiltonian believed to exhibit the same chiral topological order [131]. In the Appendix B.3, we show that this model can be cast into the fusion category framework as well, but as an anyon chain with long-range couplings rather than a fusion surface model.

For the original Hamiltonian with interchain coupling (4.34) and the CFT expansion (4.35), the coupled-wire analysis could not conclusively establish the nature of this phase, and numerics are required. We will see in the following that the entanglement spectrum shows signatures of chiral parafermion topological order even when the interactions are not fine-tuned as in (4.36). Chen et al. [95] measure a central charge close to $c = 1$ and a topological entanglement entropy close to $\sqrt{12}$ for the model (4.30) at its isotropic point. Based on their results, they conclude that chiral $U(1)_{12}$ topological order is likely. However, the central charge $c = \frac{4}{5}$ and topological entanglement entropy $\sqrt{3(1+\phi^2)} \approx \sqrt{10.85}$ of chiral parafermion topological order $\mathbb{Z}_3 \boxtimes \text{Fib}$ are not too far away from the measured values.

The entanglement spectrum proves a useful tool for distinguishing different types of topological order. Namely, the low-lying entanglement energies of a ground state with chiral topological order are characterized by the CFT of its gapless edge modes [132, 133]. It was used by Stoudenmire et al. [131] to distinguish between a chiral parafermion and a chiral $U(1)_6$ phase in their triangular lattice $\mathbb{Z}_3$ model. They found signatures of chiral $U(1)_6$ topological order in the entanglement spectrum of their model in the square lattice limit. Their Hamiltonian in this limit has almost the same parafermionic current operator description (4.33) as the honeycomb model (4.30) in fixed $B_p = 1$ sectors (the difference being that their interchain coupling is invariant under translations by one and not by two sites).

To gain more insight into the isotropic phase of our $\mathbb{Z}_3$ model, we measure the entanglement spectrum of the ground state on an infinite cylinder, using the DMRG package Tenpy [134, 135]. More details on the numerical simulations are collected in Appendix B.4. The partition function of the Potts CFT with free boundary conditions is given by

$$Z^{\text{Potts}}_{\text{f,f}}(q) = q^{-c/24}\left(1 + 2q^{2/3} + 2q^{5/3} + q^2 + 4q^{8/3} + 2q^3 + \dots\right). \tag{4.38}$$

The degeneracies of the lowest entanglement energies in a chiral parafermion phase are expected to match the coefficients $(1, 2, 2, 1, (2, 2) \dots)$ in the partition function. The $(2, 2)$ notation indicates that the four-fold degeneracy can be split into two two-fold degeneracies by finite size effects, as the corresponding term $4q^{8/3}$ in the partition function is the sum of contributions $2q^{2^2 \cdot 2/3}$ from the $\chi_{2/3}$ character and $2q^{5/3+1}$ from the $\chi_{5/3}$ character. This pattern is indeed what we observe in Fig. 4.3 for the ratios of degeneracies on cylinders of circumferences $L_y = 2, 3, 4$. The absolute degeneracies in the $L_y = 3, 4$ plots are higher due to the conserved plaquette operators crossing an entanglement cut, as observed in [136] for the original Kitaev honeycomb model. The $L_y = 2, 4$ entanglement spectra are computed across a different bond of the matrix product state than the $L_y = 3$ spectrum, due to an even-odd effect on the cylinder, see Appendix B.4 for details. We also checked that these degeneracies remain the same for various $J_z < 1$. For a chiral $U(1)_{12}$ phase, we would expect a different degeneracy pattern $(1, 2, 1, 2, 2, \dots)$.

Considering the clear signatures of chiral topological order observed in [95] as well as the parafermion CFT degeneracies in the entanglement spectra presented in Fig. 4.3, it seems likely that the phase realizes chiral parafermion topological order. One does not need to add a magnetic field or an analog of $V_{\text{eff}}^{(3)}$ from (4.21) to obtain chiral topological order; the time-reversal symmetry breaking arising from the braiding in the fusion surface models appears sufficient.

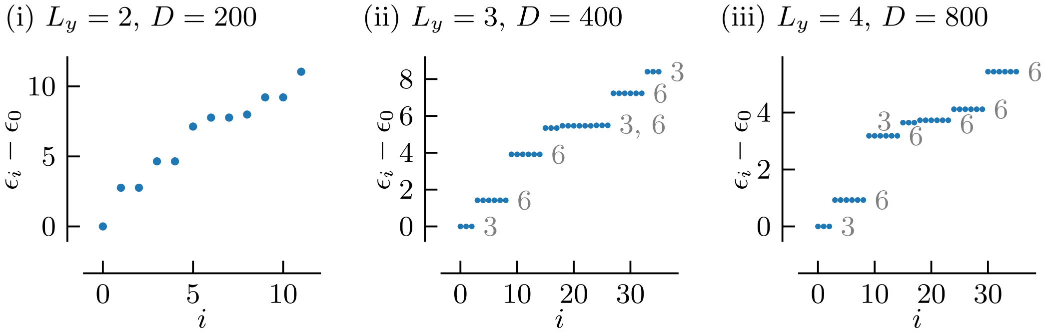
(i) $L_y = 2,\ D = 200$ (ii) $L_y = 3,\ D = 400$ (iii) $L_y = 4,\ D = 800$

Figure 4.3: Entanglement energies ϵ_i of the $\mathbb{Z}_3$ honeycomb model (4.30) with $J_x = J_y = J_z = 1$ on an infinite cylinder for different circumferences L_y and bond dimensions D; the degeneracies are written in gray. For chiral parafermion topological order, a degeneracy pattern of $(1, 2, 2, 1, (2, 2), 1, \dots)$ is expected [131].

4.6 Fibonacci fusion surface model

The Tambara-Yamagami categories give rise to very special fusion surface models with dynamical degrees of freedom only on half the planar edges, as discussed in Sections 4.4 and 4.5. To explore more generic cases where degrees of freedom live on all planar edges of the honeycomb fusion tree, we turn to a model built from the Fibonacci fusion category. This novel 2+1d Fibonacci model preserves a non-invertible 1-form symmetry and explicitly breaks time-reversal symmetry. Through a coupled-wire analysis, we show that with appropriately fine-tuned interactions, the model likely exhibits chiral topological order with tricritical Ising edge modes.

4.6.1 Constrained Hilbert space, broken time-reversal and non-invertible 1-form symmetry

The Fibonacci category contains two self-dual objects $\{1, \tau\}$ with fusion rule $\tau \otimes \tau = 1 \oplus \tau$. In our Fibonacci fusion surface model, all vertical legs of the fusion tree are labeled by the object τ. The Hilbert space is spanned by the states $|\{\Gamma_i, \Gamma_{ijk}\}\rangle$ with degrees of freedom $\Gamma_i, \Gamma_{ijk} \in \{1, \tau\}$ on all planar edges of the honeycomb fusion tree.

$$|\{\Gamma_i, \Gamma_{ijk}\}\rangle =$$

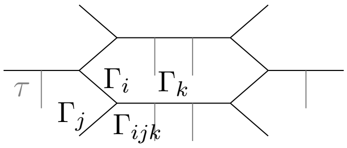

At each trivalent vertex, the Fibonacci fusion rule must be obeyed, resulting in a constrained Hilbert space. The Fibonacci fusion surface Hamiltonian $H = \sum_p H_p$ has the same structure (4.3) as Kitaev's honeycomb model, with H_p acting as

$-J_x$
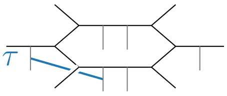

$- J_y$
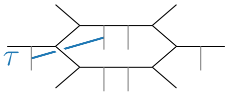

$- J_z$
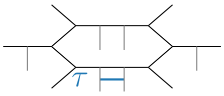

(4.39)

The x-link and y-link terms now couple seven degrees of freedom. Since τ has a trivial Frobenius-Schur indicator, the Hamiltonian is automatically Hermitian [51]. Its operator form is derived from the fusion diagrams in (4.39) and given in Appendix B.5.

The Fibonacci Hamiltonian breaks time-reversal symmetry explicitly. Although the z-link term is real, the x-link term includes complex operators such as

$$R^{\tau\tau}_{\tau}\sigma^{+}_{ijk} + (R^{\tau\tau}_{\tau})^{*}\sigma^{-}_{ijk} = \begin{pmatrix} 0 & (R^{\tau\tau}_{\tau})^{*} \\ R^{\tau\tau}_{\tau} & 0 \end{pmatrix}_{ijk},$$

where $R^{\tau\tau}_{\tau} = e^{3\pi i/5}$. If a unitary U existed such that $UH_pU^{\dagger} = H_p^{*}$, it would need to map $\sigma^{\pm}_{ijk} \to \sigma^{\mp}_{ijk}$ in the x-link term, while also commuting with the $n_{ijk} = \mathrm{diag}(0,1)_{ijk}$ matrix in the real z-link term. Such a transformation would change the commutation relations between n and $\sigma^{\pm}$, and so cannot be implemented by a unitary operator. An anti-unitary time-reversal symmetry $U\mathcal{K}$ is therefore ruled out.

By construction, the Fibonacci fusion surface model (4.39) has a 1-form symmetry generated by fusing a τ-line to incontractible cycles of the system, as well as conserved plaquette operators $B_p^{(\tau)}$. These symmetries are non-invertible because they obey the same fusion algebra as the object τ in the input category, for instance $\left(B_p^{(\tau)}\right)^2 = \mathbb{I} + B_p^{(\tau)}$.

4.6.2 Doubled Fibonacci topological order and weakly coupled tricritical Ising chains

To understand the Fibonacci model (4.39) in the anisotropic limit $J_z \gg J_x, J_y$, we apply the results derived in Section 4.2. When $J_z \to \infty$, it is known from the completely staggered antiferromagnetic Fibonacci chain (favoring the singlet fusion channel) that there are two ground states, $|1\tau 1\rangle$ and $|\tau\tilde{\tau}\tau\rangle$, on each z-link [3], where $|\tilde{\tau}\rangle = \phi^{-1}|1\rangle + \phi^{-1/2}|\tau\rangle$ and ϕ denotes the golden ratio. Each z-link can thus be replaced by a single horizontal edge labeled by 1 or τ, cf. (4.7):

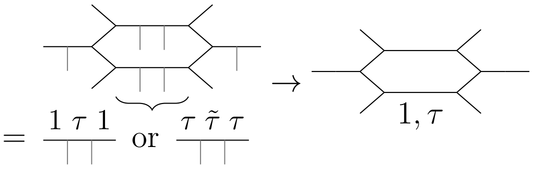

(4.40)

This substitution results in a highly degenerate ground state subspace that forms a Fibonacci string-net on the honeycomb lattice.

For sufficiently large systems, the lowest order Hamiltonian generated by perturbation theory in $J_x, J_y \ll J_z$ is the Levin-Wen plaquette operator,

$$H^{\text{eff}} \sim \frac{J_x^2 J_y^2}{J_z^3}$$

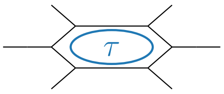

(4.41)

This Fibonacci Levin-Wen string-net, along with a magnetic field perturbation, has been studied in [137–139]. It realizes doubled Fibonacci topological order. The same holds for the limit $J_x \to \infty$, since the energy spectrum is invariant under exchanging J_z and J_z (for a symmetric geometry $L_x = L_y$ and suitable toroidal boundary conditions, as we checked numerically).

In the decoupled limit $J_x = J_y$ and $J_z = 0$, the model (4.39) reduces to L_y J_x-J_y chains with Hamiltonian

$H_{1\text{d}}: \; -J_x$

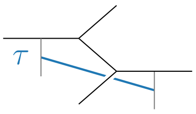

$-\,J_y$

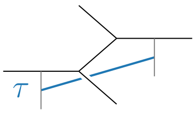

(4.42)

As explained in Sec. 4.3, the J_x-J_y chain (4.42) is unitarily related to the Fibonacci anyon chain with a sum over boundary conditions. Large degeneracies arise because of the plaquette 1-form symmetries, as illustrated in App. B.1 for the Ising fusion surface model. With uniform couplings this chain is the Hamiltonian limit [29] of a critical point of the integrable model of hard squares with diagonal interactions [140, 141], which is the A_4 case of the Andrews-Baxter-Forrester models [10]. It was reformulated in terms of fusion-category data and (re)named the "golden chain" [18]. The chain is invariant under a "topological symmetry", generated by fusing a τ-line to the fusion tree from above [18]. This symmetry is now recognized as a canonical example of a non-invertible, categorical or generalized symmetry [3, 23, 102, 142, 143]—that is, one which cannot be represented by a unitary matrix. The constrained Hilbert space of the Fibonacci anyon chain admits a physical interpretation in terms of Rydberg-blockade atoms on a chain with nearest-neighbour occupancy forbidden [29, 31].

With uniform antiferromagnetic couplings, the Fibonacci anyon chain is critical and described by the tricritical Ising conformal field theory [29, 140, 141, 144]. The same must hold for the J_x-J_y chain (4.42) with $J_x = J_y > 0$, as boundary conditions do not change the gap of the system. The tricritical Ising CFT contains a topological defect line corresponding to the non-invertible symmetry on the lattice, which obeys the same fusion algebra. Of the six chiral primary fields, only σ' with scaling dimension $h = \frac{7}{16}$ and ϵ'' with scaling dimension $h = \frac{3}{2}$ are commuting with the topological defect line [18].

The J_z term, which couples adjacent chains, commutes with the non-invertible 1-form symmetry of the fusion surface model. In the continuum limit, it can be expanded in terms of CFT fields of the critical chains it couples. Due to the non-invertible 1-form symmetry, this expression can only include σ' and ϵ''. The most relevant fields in the expansion have zero conformal spin and are given by:

$$H^z \sim \; a_1 \Phi^{(n,n+1)}_{\sigma' \bar{\sigma}'} + a_2 \Phi^{(n,n+1)}_{\bar{\sigma}' \sigma'} + a_3 \Phi^{(n)}_{\sigma' \bar{\sigma}'} \Phi^{(n+1)}_{\sigma' \bar{\sigma}'} \tag{4.43}$$

The notation $\Phi^{(n,n+1)}_{\sigma'\bar{\sigma}'}$ (instead of $\sigma'^{(n)}_L \sigma'^{(n+1)}_R$) reflects that the chiral fields σ' cannot be realized separately as local or semi-local lattice operators [130]. The fields with coefficients a_1 and a_2 in (4.43) combine the left and right σ' fields from two adjacent chains, whereas the a_3 term is a product of the non-chiral $\Phi_{\sigma'\bar{\sigma}'}$ fields from both chains. Since time-reversal symmetry is explicitly broken in the lattice Hamiltonian, we must have $a_1 \neq a_2$ in the expansion. Due to the presence of multiple CFT fields in (4.43), the nature of the resulting phase remains unclear. It could be gapless or (chiral) topological order $\mathrm{Fib} \boxtimes \mathcal{C}$, constrained by the anomalous non-invertible 1-form symmetry.

If only the first term $\Phi^{(n,n+1)}_{\sigma'\bar{\sigma}'}$ appeared in (4.43), the model would exhibit chiral topological order with tricritical Ising edge modes, following an idea going back to [19] and studied in more detail in [111, 145, 146]: The tricritical Ising CFT perturbed by $\Phi_{\sigma'\bar{\sigma}'}$ is gapped with two degenerate (but not symmetry-related) ground states [147], implying that the bulk of the coupled chain system is gapped. Since the coupling $\Phi^{(n,n+1)}_{\sigma'\bar{\sigma}'}$ does not contain the right-moving CFT fields of the bottom chain and the left-moving CFT fields of the top chain, gapless tricritical Ising edge modes remain. It is plausible that the a_2 and a_3 terms in (4.43) could be tuned away by adding different lattice couplings between adjacent chains, such as those depicted in (4.37) in the context of the $\mathbb{Z}_3$ model. The coupled-wire system with the $\Phi^{(n,n+1)}_{\sigma'\bar{\sigma}'}$ coupling, which cannot be easily decomposed into a product of two lattice operators from individual chains, appears to be unexplored. A system of coupled Grover-Sheng-Vishwanath chains [148] with tricritical Ising edge modes was studied in [149], but their coupling does not seem to respect the non-invertible Fibonacci symmetry, yielding a different coupled-wire field theory.

To support our phase diagram analysis, we compute the lowest energy levels in small Fibonacci models with $L_y = 2$, $L_x = 2, 3$. This was done with the exact diagonalization package Quspin [150]. We choose periodic boundary conditions in both directions, as depicted in (4.45). The energy gaps for $J_x = J_y = 1$ and $J_z \in [0, 3]$ are shown in Fig. 4.4(i). The plot indicates two distinct regimes separated by a phase transition, consistent with our qualitative understanding of an anisotropic phase and a weakly coupled chains phase. The ground state is always two-fold degenerate, suggesting that the 1-form symmetry around one of two incontractible cycles around the torus is spontaneously broken. A closer examination of the ground state energies in the large J_z limit, shown in Fig. 4.4(ii), reveals that the leading contributions are

$$E_{\mathrm{GS}} = -J_z L_x L_y E_{\mathrm{GS}}^{(\text{z-link})} - \frac{C}{J_z} + \mathcal{O}\left(\frac{1}{J_z^2}\right) \tag{4.44}$$

The $1/J_z$ contribution arises from incontractible loops around the torus, generated at second order in perturbation theory when $L_y = 2$ or $L_x = 2$. Schematically,

$$H^{(\text{eff})} \sim \frac{J_x J_y}{J_z}$$

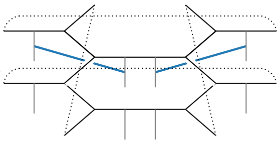

$$, \tag{4.45}$$

with the dotted edges wrapping around the torus. Due to these $1/J_z$ terms, which dominate over the $1/J_z^3$ Levin-Wen projector terms, we are unable to observe four degenerate ground states characteristic of doubled Fibonacci topological order.

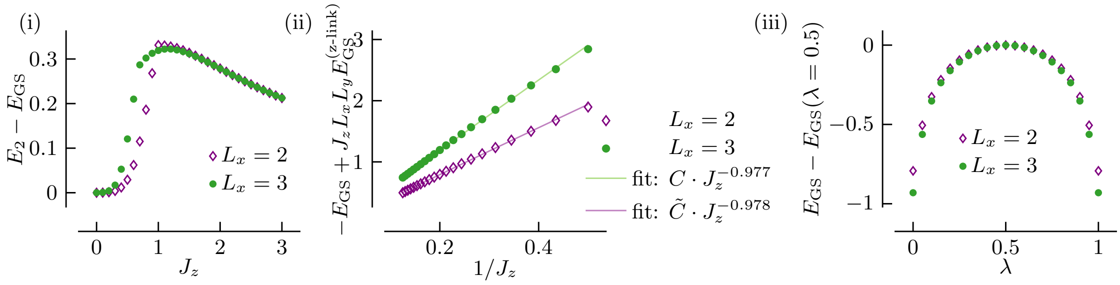

Figure 4.4: (i) Energy gap of the $L_y = 2$ Fibonacci models on a torus for $J_x = J_y = 1$, (ii) Ground state energies of the Fibonacci model on a $L_y = 2$ torus for $J_x = J_y = 1$, with the zeroth-order contribution $-J_z L_x L_y E_{\mathrm{GS}}^{(\text{z-link})}$ subtracted and the second-order contribution fitted, cf. (4.44), (iii) Ground state energies of the interpolated Hamiltonian (4.46) on a $L_y = 2$ torus with $J_x = J_y = \lambda$, $J_z = 0.6$

If the weakly coupled chains phase is described by chiral topological order, its ground state must break time-reversal symmetry. To test this hypothesis, we define a time-reversal invariant interpolation of the Fibonacci model,

$$H_p = H^z + \lambda(H^x + H^y) + (1 - \lambda)(H^x + H^y)^* \tag{4.46}$$

A similar interpolation was discussed in [125] for the $\mathbb{Z}_3$ generalization of Kitaev's honeycomb model. The ground state energies of the interpolated Fibonacci Hamiltonian (4.46) are shown in Fig. 4.4(iii). It is conceivable that a phase transition occurs at $\lambda = 0.5$, though the plot is not conclusive and larger system sizes would be necessary to confirm the existence of a transition. A phase transition at $\lambda = 0.5$ would be evidence for chiral topological order, as it implies that the ground states of the $\lambda = 0$ and $\lambda = 1$ Hamiltonians cannot be adiabatically connected.

4.7 Conserved currents and integrability

In classical 2+0d height models, terminating topological defects can be interpreted as currents. These currents are conserved when they satisfy a discrete divergence-free condition, also known as discrete holomorphicity, which was originally introduced in quantum-group symmetric models [151] and later extended to a wider class of statistical mechanical models built from fusion categories [126]. This conservation condition implies Yang–Baxter integrability and is satisfied, for instance, in the ABF models at their integrable and critical points. We begin by reformulating the current conservation condition from [126] in the setting of 1+1d anyon chains. We then attempt to generalize this construction to 2+1d fusion surface models. However, perhaps unsurprisingly, we find no 2+1d solutions beyond Kitaev's honeycomb model tuned to its phase transition line.

4.7.1 Conserved currents in 1+1d anyon chains

In 2d statistical mechanical models constructed from a braided fusion category $\mathcal{B}$, conservation of a current $\phi \in \mathcal{B}$ can be depicted graphically as [126]

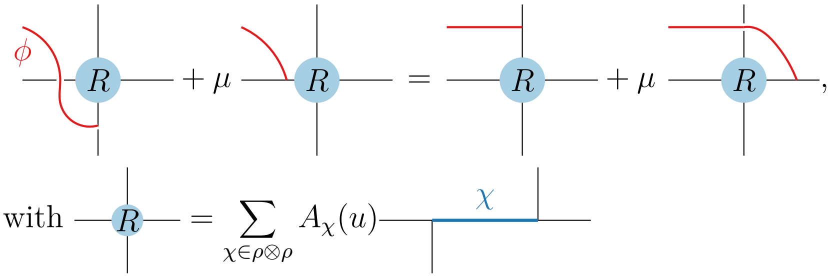

(4.47)

All black edges are labeled by the same object $\rho \in \mathcal{B}$. The operator $R_j(u) = \sum_{\chi \in \rho\otimes\rho} A_\chi(u) P_j^{(\chi)}$ depicted in the second row is the generator of the transfer matrix. It is a linear combination of projectors $P_j^{(\chi)}$ with amplitudes $A_\chi(u)$ that depend on the spectral parameter u. These amplitudes are assumed to be uniform across the lattice. The parameter μ is a complex number that rescales the x and y coordinates in the 2d picture. To allow the current ϕ to over-cross the black lines, the input category $\mathcal{B}$ must be braided. For a category that does not admit braiding (such as $\frac{1}{2}E_6$ or Haagerup [152]), one might still be able to define a conserved current by lifting ϕ to the Drinfeld center and using its half-braiding. The pictorial condition (4.47) translates into a condition on the Boltzmann weights $A_\chi(u)$ and the deformation parameter μ, involving the R-symbols of $\mathcal{B}$ [126]:

$$\frac{A_\alpha(u)}{A_\beta(u)} = \frac{R_\rho^{\rho\beta} + \mu R_\rho^{\rho\alpha}}{R_\rho^{\rho\alpha} + \mu R_\rho^{\rho\beta}} \quad \text{for } \alpha, \beta \text{ with } N_{\alpha\phi}^{\beta} \neq 0. \tag{4.48}$$

To obtain the analogue of the conserved-current condition (4.47) for 1+1d anyon chains, we expand the transfer matrix generator as $R_j(u) \approx \mathbb{I} + uH_j$, where H_j denotes the local anyon chain Hamiltonian. Simultaneously, we expand the lattice deformation parameter as $\mu \approx 1 + Au$, with A a constant. Collecting terms linear in u, we find:

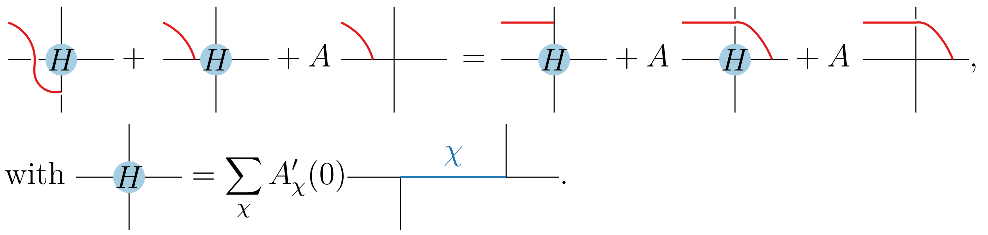

(4.49)

This can be rearranged into a relation for the commutator of the local anyon chain Hamiltonian and the current,

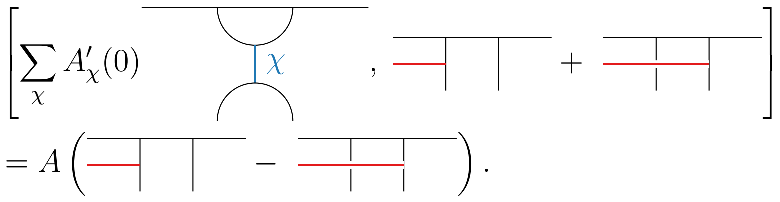

(4.50)

Written out as an equation, (4.50) becomes

$$\left[H_i, J_{i-1,i}^{(\phi)} + J_{i,i+1}^{(\phi)}\right] = A\left(J_{i-1,i}^{(\phi)} - J_{i,i+1}^{(\phi)}\right), \tag{4.51}$$

where $J^{(\phi)}_{i-1,i}$ is the current operator terminating at the vertical leg $(i-1,i)$. If the conservation condition (4.51) is satisfied, the commutator between the full Hamiltonian (with translation-invariant couplings) and the charge $Q^{(\phi)} = \sum_k J^{(\phi)}_{k-1,k}$ vanishes up to boundary terms:

$$\left[H, Q^{(\phi)}\right] = \left[\sum_i H_i, \sum_k J^{(\phi)}_{k-1,k}\right] = \sum_i \left[H_i, J^{(\phi)}_{i-1,i} + J^{(\phi)}_{i,i+1}\right] = A\left(J^{(\phi)}_{1,2} - J^{(\phi)}_{L-1,L}\right). \tag{4.52}$$

The second equality in (4.52) holds because H commutes with the current away from its endpoint. In the anyon chain setting, the analogue of the Boltzmann weight condition (4.48), derived from the diagrammatic constraint (4.47), is a condition on the coefficients $A'_\chi(0)$ of the terms in the Hamiltonian $H_j = \sum_\chi A'_\chi(0) H^{(\chi)}_j$:

$$A'_\beta(0) - A'_\alpha(0) = \frac{R^{\rho\alpha}_\rho - R^{\rho\beta}_\rho}{R^{\rho\alpha}_\rho + R^{\rho\beta}_\rho} \quad \text{for } \alpha, \beta \text{ with } N^\beta_{\alpha\phi} \neq 0. \tag{4.53}$$

As an example, consider the parafermion current $J^{(1)}_j$ in the $\mathbb{Z}_3$ Potts model built from the Tambara–Yamagami category. This current was introduced in Section 4.5.3 under the name $\hat{\alpha}_{R,j}$. Since the braiding phases satisfy $R^{\sigma 1}_\sigma = R^{\sigma 2}_\sigma$ (cf. (4.25)), the condition (4.53) holds whenever $A'_2(0) = A'_1(0)$, i.e., when the Hamiltonian is hermitian. In this case, one can also verify explicitly that the local commutator relation (4.51) is satisfied:

$$\left[H_{2i}, J^{(1)}_{2i-1,2i} + J^{(1)}_{2i,2i+1}\right] =$$

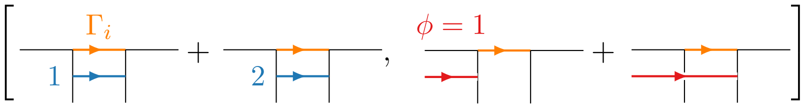

$$= \left[X_i + X_i^\dagger, Z_i + \omega X_i Z_i\right] = (\omega - \omega^2)(Z_i - \omega X_i Z_i) = (\omega - \omega^2)\left(J^{(1)}_{2i-1,2i} - J^{(1)}_{2i,2i+1}\right).$$

Note that, since the red line $\phi = 1$ over-crosses the black σ edge, it does not reverse its direction (cf. Section 4.5.1). The same condition with respect to the diagonal terms in the Hamiltonian reads

$$\left[H_{2i+1}, J^{(1)}_{2i,2i+1} + J^{(1)}_{2i+1,2i+2}\right] =$$

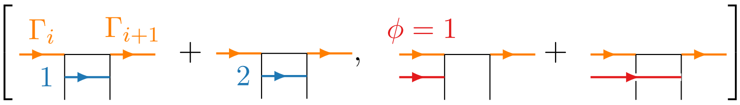

$$= \left[Z_i Z^\dagger_{i+1} + Z^\dagger_i Z_{i+1}, \omega X_i Z_i + X_i Z_{i+1}\right] = (\omega - \omega^2)(\omega X_i Z_i - X_i Z_{i+1})$$
$$= (\omega - \omega^2)\left(J^{(1)}_{2i,2i+1} - J^{(1)}_{2i+1,2i+2}\right).$$

4.7.2 Conserved currents in 2+1d fusion surface models?

Given an anyon chain built from a braided fusion category $\mathcal{B}$ with a conserved charge $Q^{(\phi)} = \sum_k J^{(\phi)}_{k-1,k}$, it is natural to ask whether the corresponding 2+1d fusion surface model constructed from $\mathcal{B}$ admits a related conserved quantity.

The z-link term in the fusion surface model Hamiltonian (4.3) coincides with the local anyon chain Hamiltonian and thus automatically satisfies the current conservation condition (4.51). The x- and y-link terms, which can be viewed as twisted versions of the anyon chain Hamiltonian (as discussed in Section 4.3), satisfy modified versions of the conservation condition:

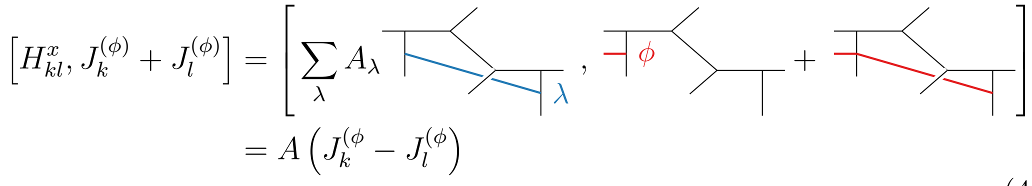

(4.54)

Here, the coefficients A_λ are chosen so that the anyon chain Hamiltonian with local terms $\sum_i A_\lambda H^{(\lambda)}_i$ admits a conserved current ϕ. With a slight abuse of notation, we now label the vertical legs by lowercase letters $k, l, \ldots$ and denote the currents terminating at them as $J^{(\phi)}_k$, and so on. Note that in the second diagram, the ϕ line must under-cross the black edge, reflecting the interpretation of this edge as a twist added to the anyon chain.

This approach suggests the possibility of defining a conserved surface charge $Q^{(\phi)}_{\text{surf}} = \sum_v J^{(\phi)}_v$, where the sum runs over all vertical legs v of the honeycomb fusion tree, as illustrated in Fig. 4.5. The commutator $[H, Q_{\text{surf}}] = [H, \sum_v \mathcal{J}_v]$ contains three contributions for each vertical leg in the bulk:

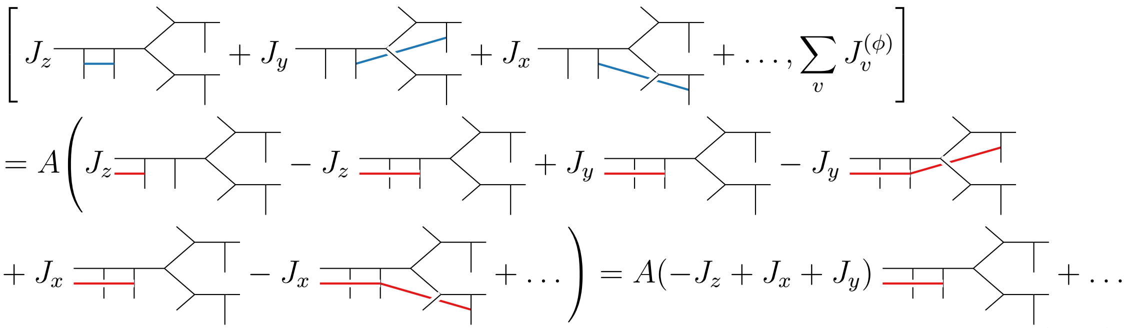

(4.55)

When the Hamiltonian couplings are tuned to satisfy $J_x + J_y = J_z$, the contributions to the commutator vanish for each vertical leg in the bulk. To ensure that the surface charge depicted in Fig. 4.5 is conserved up to boundary terms, we also require that $B_p = 1$ everywhere.

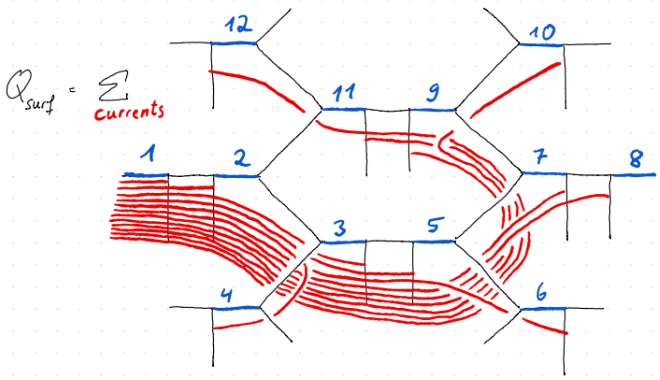

Figure 4.5: The surface charge $Q^{(\phi)}_{\text{surf}} = \sum_v J^{(\phi)}_v$ is the sum of all currents $J^{(\phi)}_v$ terminating at the vertical legs v of the honeycomb lattice.

However, a subtle issue arises: to commute with Hamiltonian terms away from their endpoints, the current operators must act from above, like symmetry lines. In contrast, the endpoint conservation condition (4.54) requires them to act from below. This apparent contradiction is resolved in Kitaev's honeycomb model. There, the black edges under-crossed by the current line are labeled by σ and do not correspond to physical degrees of freedom. As a result, the distinction between over- and under-crossing amounts to a global braiding phase. One can verify that the surface charge $Q^{(\phi)}_{\text{surf}}$ indeed commutes with Kitaev's honeycomb Hamiltonian along the critical line $J_x + J_y = J_z$, which marks the phase transition between the A and B phases. This mirrors the situation in the 1+1d models, where current conservation similarly signals criticality.

In the $\mathbb{Z}_N$ generalization, the distinction between over- and under-crossing becomes crucial, and no conserved surface charge exists: due to the G-crossed braiding, currents change direction when they under-cross σ edges, but not when they over-cross. In fusion surface models not derived from Tambara–Yamagami categories, all planar edges correspond to dynamical degrees of freedom. In such cases, a conserved surface charge of the form shown in Fig. 4.5 can only exist if the object ϕ labeling the current braids symmetrically with all objects $\alpha \in \mathcal{B}$, meaning the braiding phase $R^{\phi\alpha}_{\beta}$ must be a real number ±1 so that over- and under-crossings become indistinguishable. However, all known examples from [126] that satisfy the conservation condition (4.51) involve currents with fractional topological spin $\Delta_\phi \notin \mathbb{Z}$, which enters the braiding phases as

$$R^{\alpha\beta}_{\gamma} = \nu^{\alpha\beta}_{\gamma}, e^{i\pi(\Delta_\alpha + \Delta_\beta - \Delta_\gamma)},$$

where $\nu^{\alpha\beta}_{\gamma}$ is a sign factor. For such currents, the braiding $R^{\phi\rho}_{\rho} = \nu^{\phi\rho}_{\rho} e^{i\pi\Delta_\phi}$ is not real when Δ_ϕ is not an integer. This indicates that conserved surface charges of the type shown in Fig. 4.5 are unlikely to arise in 2+1d fusion models beyond Kitaev's honeycomb model.

5

Dualities between 2+1d fusion surface models

Contents

Dualities are ubiquitous in statistical mechanics and condensed matter physics, starting with the seminal 1941 work of Kramers and Wannier [4]. The exploration of duality mappings beyond Kramers-Wannier likely began with the work of Temperley and Lieb [5] and Baxter, Kelland, and Wu [9], who established an equivalence between the q-state Potts model and the six-vertex model. As this example highlights, dualities can connect systems with different Hilbert spaces and symmetries while preserving the energy gap in the thermodynamic limit.

More recently, dualities in 1+1d spin chains and anyon chains have been formalized using the language of discrete gauging and module categories over fusion categories [23, 24, 27, 28, 153, 154], as reviewed in Section 2.3.2. Extending this understanding to 2+1d remains an open challenge, although progress has been made using approaches grounded in tensor networks and higher-category theory [52, 155–158].

This chapter explores dualities in 2+1d fusion surface models built from braided fusion categories, introduced in the previous chapter. Unlike earlier constructions that begin with systems with global invertible 0-form symmetries [52, 155–157], our approach starts from models with categorical 1-form symmetries. Dualities in this setting arise by gauging some or all of these categorical 1-form symmetries. The resulting models can conserve independent 0-form symmetries and realize symmetry-enriched topological orders, thereby expanding the known landscape of fusion surface models. Notably, this framework includes familiar systems such as the spin-$\frac{1}{2}$ XXZ model on honeycomb or square lattices.

5.1 Extended fusion surface model construction from module tensor categories and braided fusion categories

This section develops a systematic framework for constructing 2+1d fusion surface models that are dual to those built from a braided fusion category $\mathcal{B}$. The central mathematical ingredient is a module tensor category $\mathcal{M}$ over $\mathcal{B}$—a module category endowed with its own tensor product structure [159]. In contrast to the 1+1d case, building the dual Hamiltonian in 2+1d requires additional data such as mixed $\tilde{F}$-symbols and half-braiding phases between objects in $\mathcal{M}$ and $\mathcal{B}$. A discussion of the resulting symmetry fusion 2-category is deferred to the final section.

The Hilbert space of the dual models is spanned by states represented as fusion diagrams of the form

$$|\{M_i, M_{ijk}, v_{ijk}\}\rangle = \qquad (5.1)$$

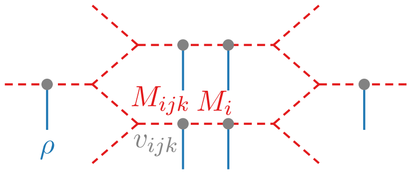

Here, the planar red edges are labeled by the degrees of freedom M_i and M_{ijk} in $\mathcal{M}$. As before, vertical legs are labeled by a fixed object $\rho \in \mathcal{B}$ and gray vertices, where objects in $\mathcal{M}$ meet ρ, are assigned basis vectors $v_{ijk} \in \mathcal{V}^{M_i}_{\rho M_{ijk}}$, analogous to the 1+1d case reviewed in Section 2.3.2. These v_{ijk} vertex degrees of freedom do not appear in the standard fusion surface model derived from a multiplicity-free braided fusion category $\mathcal{B}$ (cf. (4.1)). The primary distinction between the 1+1d case (cf. (2.12)) and the 2+1d one is the presence of trivalent vertices where three objects in $\mathcal{M}$ meet. These vertices necessitate an intrinsic tensor product of the module category $\mathcal{M}$.

We use the same local Hamiltonian $H_p^{(\lambda)}$ as in (4.3), defined for a label $\lambda \in \mathcal{B}$ and a plaquette p. Its action on the state (5.1) is illustrated as

$$H_p^{(\lambda)} : -J_x$$

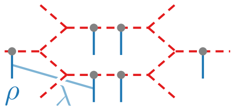

$$-J_y$$

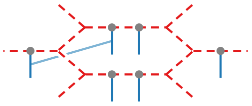

$$-J_z$$

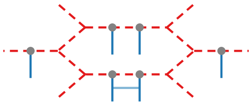

(5.2)

As in 1+1d, it is evident from the pictorial representation that the algebra generated by the local terms in the Hamiltonian remains invariant under changing the module tensor category $\mathcal{M}$. The full Hamiltonian is given by

$$H = \sum_p C_p \sum_{\lambda \in \mathcal{B}} A_\lambda H_p^{(\lambda)} \quad \text{with } C_p, A_\lambda \in \mathbb{R}. \tag{5.3}$$

The z-link term corresponds directly to the local anyon chain Hamiltonian (2.13). For the x-link term, the Hamiltonian line $\lambda \in \mathcal{B}$ is fused to the lattice using the orthogonality relations (2.6),

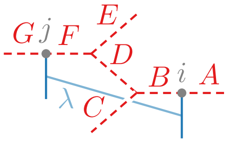

$$= \sum_{B',C',D',F'} \sum_{k,l,m,n} \sqrt{\frac{d_{B'} d_{C'} d_{D'} d_{F'}}{d_B d_C d_D d_F d_h^4}}$$

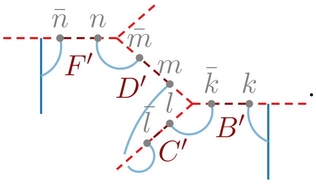

. (5.4)

To evaluate the diagram on the right hand side of (5.4), a new type of mixed F-symbol $\tilde{F}$ is required. This mixed $\tilde{F}$-symbol is well-defined only for module categories with an intrinsic tensor product structure,

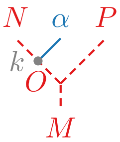

$$= \sum_Q \sum_i [\tilde{F}^{N\alpha P}_M]^{O,k}_{Q,i}$$

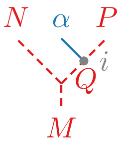

(5.5)

Additionally, half-braiding phases between objects in $\mathcal{M}$ and $\mathcal{B}$ are needed [60, 159]:

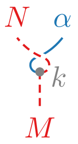

$$= \Omega^{N\alpha}_{M,k}$$

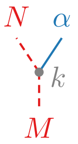

(5.6)

The mixed $\tilde{F}$-symbols (5.5) have to satisfy consistency conditions that resemble the pentagon equation, involving $\tilde{F}$, ${}^{\triangleleft}F$ and ${}^{\triangleright}F$ symbols. Similarly, the half-braiding phases Ω are constrained by hexagon-like equations. We expect that both the $\tilde{F}$-symbols and Ω phases can be determined explicitly by solving these consistency conditions. Using the ${}^{\triangleleft}F$, $\tilde{F}$ and Ω symbols, the x-link term (5.4) evaluates to

$$\sum_{\substack{B',C'\\D',F'}} \sum_{\substack{i',j'\\k,l,m,n}} [{}^{\triangleleft}F^{\rho\lambda B'}_{A}]^{B,k,i}_{\rho,i'}\, [\tilde{F}^{B\lambda C'}_{D}]^{C,l}_{B',k}\, [\tilde{F}^{C'\lambda D'}_{B'}]^{D,m}_{C,l} [\tilde{F}^{D\lambda F'}_{E}]^{F,n}_{D',m}\, [{}^{\triangleleft}F^{F\lambda\rho}_{G}]^{\rho,j}_{F',j',n}\, \Omega^{C\lambda}_{C,\bar{l}}\sqrt{d_\lambda}$$

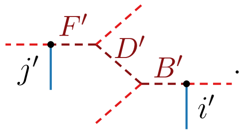

$$.$$

(5.7)

The y-link term can be computed analogous to the x-link term. The regular $\mathcal{M}=\mathcal{B}$ fusion surface model has categorical 1-form symmetries corresponding to objects in $\mathcal{B}$, see Section 4.1. The fusion 2-categorical symmetries of models with $\mathcal{M}\neq\mathcal{B}$ are discussed in the last section.

For these dual fusion surface models, we expect a similar phase diagram as the one depicted in Fig. 4.1 for the standard fusion surface models. As discussed below, the anisotropic limits $A_{x,y,z}$ are characterized by non-chiral $\mathcal{Z}(\mathcal{M})$ topological order. In phase B, the presence of additional 0-form symmetries allows for the possibility for symmetry-enriched topological order.

In the extreme limit $J_x = J_y = 0$, the ground state of the honeycomb model (5.2) becomes the simultaneous ground state of all z-link Hamiltonians. As in Section 4.2, we choose the z-link Hamiltonian to be the projector onto the identity object, $H^z = -J_z P^{(0)}$, which allows for straightforward identification of its ground state. This projector can be depicted as follows:

$$\sqrt{d_\rho}P^{(0)} :$$

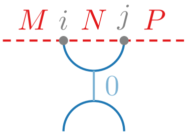

$$= \delta_{M,P}\,\delta_{i,j}\sum_{k,N'}\sqrt{\frac{d_{N'}d_N}{d_M^2}}$$

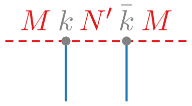

(5.8)

Here we used the orthogonality and resolution of identity relations (2.6). Because of the two delta functions in (5.8), only those states with $M = P$ and $i = j$ have nonzero eigenvalue under the projector and qualify as ground states of $H^z = -J_z P^{(0)}$. The energy does not depend on the basis vector i since the projector maps each state $|M, i, N, i, M\rangle$ to the superposition $\sum_{i',N'} \sqrt{d_{N'}}\, |M, i', N', i', M\rangle$. Hence, the superposition $\sum_{i',N'} \sqrt{d_{N'}}\, |M, i', N', i', M\rangle$ is the unique +1 ground state for a given M. Therefore, we expect one ground state for each element $M \in \mathcal{M}$, and the ground state subspace is a $\mathcal{M}$ string-net.

Because the perturbation theory Hamiltonian has to generate the same bond algebra as the regular $\mathcal{M} = \mathcal{B}$ perturbation theory Hamiltonian derived in Section 4.2, it has to act as

$H_p^{\text{eff}, \lambda}$:

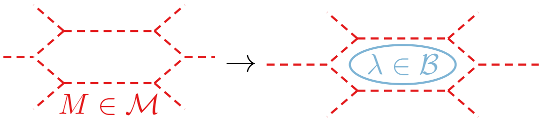

(5.9)

The $\mathcal{B}$-loop acting on the $\mathcal{M}$ string-net can be resolved into $\mathcal{M}$-loops,

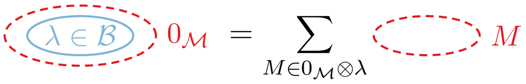

Here $0_{\mathcal{M}}$ denotes the identity object of $\mathcal{M}$ and the equality follows from the orthogonality relations (2.6). Therefore, the effective model in perturbation theory is a $\mathcal{M}$ string-net with a commuting plaquette operator Hamiltonian, exhibiting $\mathcal{Z}(\mathcal{M})$ topological order.

5.2 Example: XXZ honeycomb model and Rep(S_3) fusion surface model

This section extends the 1+1d Rep(S_3) example from Section 3.3.2 to one dimension higher. The first model, built from the trivial module category, corresponds to the well-known XXZ model on a honeycomb lattice. The second, derived from the regular module category, has a constrained Hilbert space and a Rep(S_3) 1-form symmetry. Since the duality ought to preserve the distinction between gapped and gapless phases, we can leverage known results about the XXZ honeycomb model to deduce properties of its dual Rep(S_3) model.

5.2.1 XXZ honeycomb model from $\mathcal{M}$ = Vec

We begin by selecting the trivial module category $\mathcal{M} = \text{Vec}$ over the fusion category $\mathcal{B} = \text{Rep}(S_3)$ with symmetric braiding. The resulting fusion surface model has a tensor product Hilbert space of qubits $v_{ijk} \in \mathbb{Z}_2$ located at the trivalent vertices involving ρ. All planar red edges are labeled by the unique object $\underline{0} \in \text{Vec}$.

$$|\{v_{ijk}\}\rangle = \tag{5.10}$$

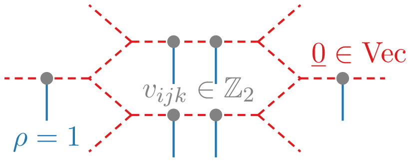

The x-link and y-link terms in this model are identical to the z-link term, identified as the spin-$\frac{1}{2}$ XXZ Hamiltonian in Section 3.3.2, provided the couplings in (5.2) are chosen as $A_0 = -A_2 = \Delta/\sqrt{2}$ and $A_1 = \sqrt{2}$. With this choice, the full Hamiltonian becomes the XXZ model on a honeycomb lattice:

$$\begin{aligned} H = J_x \sum_{i,j\in\text{x-link}} (X_iX_j + Y_iY_j + \Delta Z_iZ_j) + J_y \sum_{i,j\in\text{y-link}} (X_iX_j + Y_iY_j + \Delta Z_iZ_j) \\ + J_z \sum_{i,j\in\text{z-link}} (X_iX_j + Y_iY_j + \Delta Z_iZ_j) \end{aligned} \tag{5.11}$$

This model preserves a $U(1) \rtimes \mathbb{Z}_2$ 0-form symmetry generated by $\sum_j Z_j$ and $\prod_j X_j$, but no 1-form symmetries. This symmetry structure is consistent with theoretical expectations: gauging the Rep(S_3) 1-form symmetry of the dual model described in the next subsection produces an S_3 0-form symmetry, which is a finite subgroup of the full $U(1) \rtimes \mathbb{Z}_2$ 0-form symmetry.

Variants of the XXZ honeycomb model (5.11) have been extensively explored in the condensed matter literature, particularly in the isotropic case ($J_x = J_y = J_z$) and with additional nearest and next-nearest neighbor interactions stabilizing spin-liquid phases [160–163]. We note that the XXZ model on a square lattice can also be realized as a fusion surface model by omitting every other vertical leg in (5.10):

$$\sum_{\lambda\in\text{Rep}(S_3)} A_\lambda$$

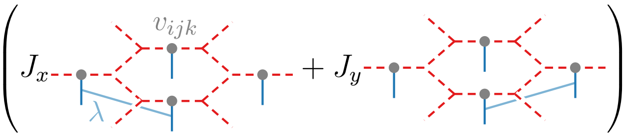

At the isotropic point $J_x = J_y = J_z$, the 2d XXZ model with $\Delta > 0$ is known to possess antiferromagnetic order, both on the square lattice [164–166] and on the honeycomb lattice [167, 168]. The Néel-ordered ground states are aligned along the z-axis for $\Delta > 1$ and within the xy-plane for $0 < \Delta < 1$. In the latter case, the $U(1)$ symmetry is spontaneously broken, leading to gapless Goldstone modes. At the Heisenberg point $\Delta = 1$, the full $SU(2)$ symmetry is spontaneously broken, again resulting in gapless Goldstone excitations over the Néel-ordered ground states.

We now analyze the phase diagram of the XXZ honeycomb model (5.11) away from the isotropic point, guided by two analytically tractable limits. First, in the anisotropic $J_z \gg J_x, J_y$ limit at $\Delta = 1$, the model reduces to a $\mathcal{Z}(\mathcal{M}) = \mathrm{Vec}$ trivial string-net in perturbation theory (see (5.9)), resulting in a trivially gapped phase. This trivial phase is expected to persist for other values of $\Delta > -1$, provided the z-link term retains a unique ground state. Second, when $J_x = 0$ and $J_y = J_z$, the model reduces to decoupled XXZ spin chains. These chains are critical and described by a free boson CFT in the regime $-1 < \Delta \leq 1$. The schematic phase diagram of the antiferromagnetic $\Delta > 0$ XXZ honeycomb model is illustrated below:

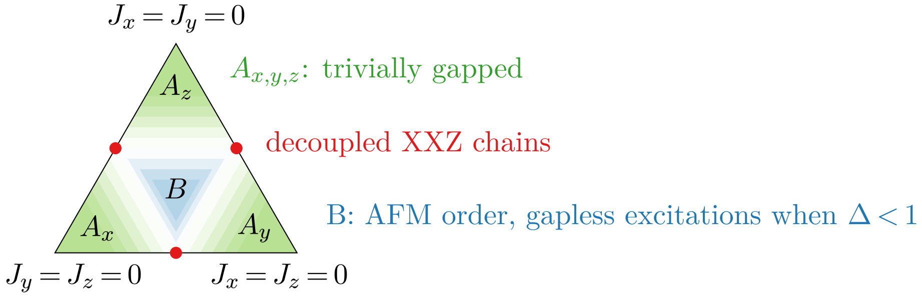

A second-order transition between the antiferromagnetic phase around the isotropic point and the trivial phase in the anisotropic limit has been observed numerically in the honeycomb XXZ model at $\Delta = 0$ [169]. We perform infinite DMRG simulations on the honeycomb Hamiltonian (5.11) with nonzero Δ, fixing $J_y = J_z = 1$, and varying the rung coupling J_x. Calculations were performed using the TeNPy Library [135]. Figure 5.1 shows the results for $\Delta = 1$. To quantify quantum correlations both along the XXZ chain direction and around the short circumference of the cylinder, we measure the concurrence, as defined in [169].

$$C_{ij} = 2 \max \left\{0, |Z_{ij}| - \sqrt{X_{ij}^{+} X_{ij}^{-}}\right\},$$

$$\text{where } Z_{ij} = \langle S_{ij}^{+} S_{ij}^{-} \rangle \text{ and } X_{ij}^{\pm} = \langle \left(\tfrac{1}{2} - S_i^z\right) \left(\tfrac{1}{2} \pm S_j^z\right) \rangle.$$

At large J_x, only the rung-direction concurrence C_x is nonzero, consistent with a unique ground state of dimers aligned along the rungs. As J_x decreases, the concurrences in both directions become nonzero, as expected for antiferromagnetic ground states in two spatial dimensions. The second derivative of the ground state energy peaks at the transition between these two regimes, signaling a critical phase transition. Around $J_x = 0$, zero concurrence along the rung hints that the system is effectively described by decoupled critical XXZ chains. However, no phase transition from this decoupled chains regime to the antiferromagnetic phase is observed in the energy derivatives, suggesting that the decoupled chains regime does not represent a distinct quantum phase. In summary, our findings support the qualitative phase diagram presented above and provide evidence that the second-order transition observed in [169] persists for nonzero $\Delta > 0$.

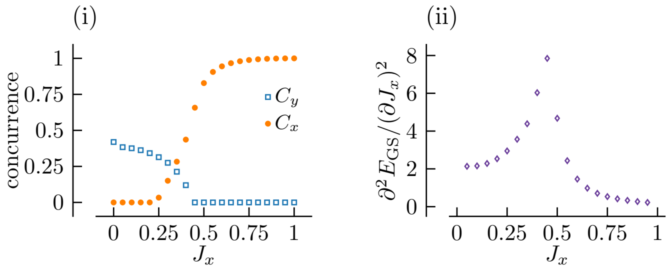

Figure 5.1: (i) Concurrences C_x, C_y of the XXZ honeycomb model (5.11) and (ii) second derivative of the ground state energy, computed with infinite DMRG on a $L_y = 4$ cylinder with bond dimension $D = 800$. The plots are for fixed $J_y = J_z = (J_x - 1)/2$ and $\Delta = 1$.

5.2.2 Fusion surface model from $\mathcal{M} = \mathbf{Rep}(S_3)$

The regular $\mathcal{B} = \mathrm{Rep}(S_3)$ fusion surface model features a constrained Hilbert space in which the fusion rules enforce $\Gamma_{ijk} \in \Gamma_i \otimes 1$ and $\Gamma_{ijk} \in \Gamma_j \otimes \Gamma_k$,

$$|\{\Gamma_i, \Gamma_{ijk}\}\rangle =$$

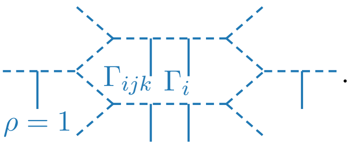

. (5.12)

The Hamiltonian (5.2) is invariant under a $\mathrm{Rep}(S_3)$ 1-form symmetry and the corresponding mutually commuting plaquette operators, cf. (4.5). Time-reversal symmetry is preserved since all braiding phases and F-symbols are real. We choose the same parametrization as for the XXZ Hamiltonian, namely $A_0 = -A_2 = \Delta/\sqrt{2}$ and $A_1 = \sqrt{2}$ in (5.3).

This fusion surface model has the following two analytically tractable limits: In the anisotropic limit $J_z \gg J_x, J_y$ and $\Delta = 1$, the model simplifies to a $\text{Rep}(S_3)$ string-net exhibiting non-chiral $\mathcal{Z}(\text{Rep}(S_3)) = D(S_3)$ topological order [170]. The $\Delta = 1$ condition ensures that the z-link term acts as a projector matrix, which is used in the computation (5.9). As noted previously for the XXZ model, we expect this result to be robust around $\Delta = 1$, as long as the z-link term has the same number of ground states. A similar $D(S_3)$ topologically ordered phase is expected when J_x or J_y dominate.

When $J_x = 0$ and $J_y = J_z$, the 2+1d model effectively reduces to a stack of $\text{Rep}(S_3)$ anyon chains summed over boundary conditions [170]. The $\text{Rep}(S_3)$ anyon chain, also known as the integrable Rydberg-blockade ladder, is critical in the regime $-1 \leq \Delta \leq 1$; see Section 3.5. The phase B in the center of the diagram is likely non-chiral, given that the Hamiltonian preserves time-reversal symmetry – unlike the chiral examples studied in the previous Sections 4.5, 4.6. Leveraging the duality to the XXZ model, we expect gapless excitations in this phase for $|\Delta| \leq 1$, akin to the Goldstone excitations seen in the XXZ model. We leave a further study of this phase for future work, as the constrained Hilbert space makes numerical simulations more challenging. Moreover, unlike the corresponding 1+1d anyon chain, this Hilbert space lacks a physical interpretation in terms of Rydberg-blockade atoms. The simplest phase diagram for fixed $\Delta > 0$ consistent with the above considerations is schematically

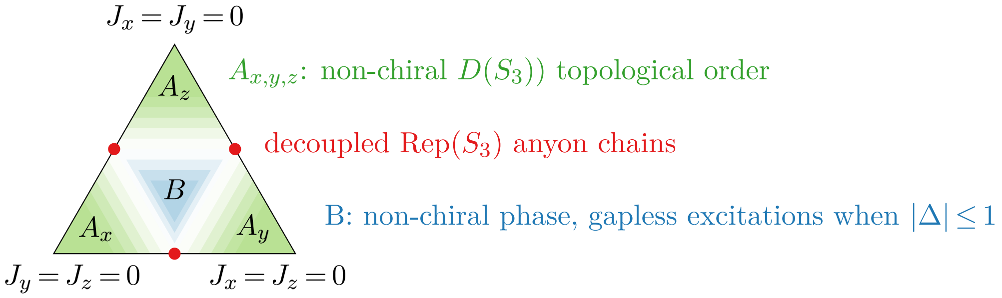

5.3 Example: Kitaev bilayer and XXZ-Ising honeycomb model

Next, we investigate a pair of models based on the $\mathcal{B} = \text{Ising} \boxtimes \overline{\text{Ising}}$ category. The regular module category gives rise to a bilayer Kitaev honeycomb model with $\mathbb{Z}_2 \boxtimes \overline{\mathbb{Z}_2}$ 1-form symmetries. Its dual counterpart, built from the $\mathcal{M} = \text{Ising}$ module category, resembles a honeycomb XXZ model augmented by additional link qubits with Ising interactions. This XXZ-Ising model preserves both $\mathbb{Z}_2$ 0-form and 1-form symmetries. Through perturbation theory and insights from the bilayer model, we explore the phase diagrams of these systems, identifying non-chiral topologically ordered phases and regions characterized by 0-form symmetry breaking.

5.3.1 Kitaev honeycomb bilayer from $\mathcal{M} = \text{Ising} \boxtimes \overline{\text{Ising}}$

The input for constructing the fusion surface model is $\mathcal{B} = \text{Ising} \times \overline{\text{Ising}}$, where the objects in the $\overline{\text{Ising}}$ category have opposite braiding phases. For the regular module category $\mathcal{M} = \mathcal{B}$, the Hilbert space consists of two qubits on each orange dotted link $\Gamma_{ijk} \in \{0\bar{0}, 1\bar{0}, 0\bar{1}, 1\bar{1}\}$:

$$|\{\Gamma_{ijk}\}\rangle =$$

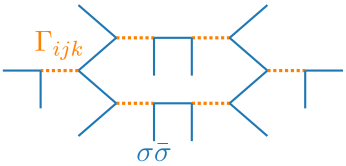

All blue links are fixed and labeled by the $\sigma\bar{\sigma}$ object. The Hamiltonian $H_p^{(\lambda)}$ for $\lambda = 1\bar{0}$ is unitarily equivalent to Kitaev's honeycomb model Hamiltonian (cf. Section 4.4.1), acting only on the first layer of qubits. Similarly, $\lambda = 0\bar{1}$ acts on the second layer, while $\lambda = 1\bar{1}$ corresponds to the product of the two local Hamiltonians, as $0\bar{1} \otimes 1\bar{0} = 1\bar{1}$. Up to a unitary transformation, the total Hamiltonian is given by:

$$\begin{aligned} H = J_x \sum_{i,j \in \text{x-link}} \left(\sigma_i^x \sigma_j^x - \tau_i^x \tau_j^x + \Delta \sigma_i^x \sigma_j^x \tau_i^x \tau_j^x\right) + J_y \sum_{i,j \in \text{y-link}} \left(\sigma_i^y \sigma_j^y - \tau_i^y \tau_j^y + \Delta \sigma_i^y \sigma_j^y \tau_i^y \tau_j^y\right) \\ + J_z \sum_{i,j \in \text{z-link}} \left(\sigma_i^z \sigma_j^z - \tau_i^z \tau_j^z + \Delta \sigma_i^z \sigma_j^z \tau_i^z \tau_j^z\right). \end{aligned} \tag{5.13}$$

where σ^α and τ^α act on the first and second qubit layer, respectively, and Δ is the interlayer coupling. The abelian objects in $\mathcal{B}$ give rise to a fermionic $\mathbb{Z}_2 \boxtimes$

$\overline{\mathbb{Z}_2}$ 1-form symmetry, including commuting plaquette operators for each layer. The non-abelian objects do not generate 1-form symmetries, as they change the Hilbert space; see Section 4.4.3.

We chose the signs of the coupling constants in (5.13) to match the convention in Hwang [171], who numerically studied this Hamiltonian at isotropic couplings $J_x = J_y = J_z = 1$. Their results yield the following phase diagram:

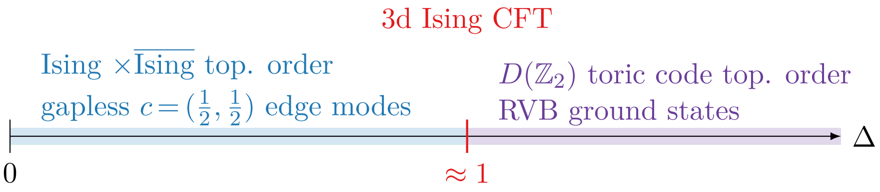

Here we summarize their main findings: At $\Delta = 0$, the system consists of two decoupled gapless Kitaev honeycomb models. Introducing a small Δ induces chiral Ising topological order in both layers, but with opposite chiralities. Hence, this topologically ordered phase is described by the Ising $\boxtimes$ $\overline{\text{Ising}}$ unitary modular tensor category, which served as input for our fusion surface model construction. This phase supports non-chiral, gapless edge modes characterized by the full Ising conformal field theory with central charge $c = (\frac{1}{2}, \frac{1}{2})$. In the large Δ limit, the system reduces, via perturbation theory, to a quantum dimer model on a kagome lattice with resonating valence bond ground states. This model is known to display toric code topological order $D(\mathbb{Z}_2)$ [172]. The second-order phase transition near $\Delta = 1$ can be interpreted as an anyon condensation transition between the Ising $\boxtimes$ $\overline{\text{Ising}}$ and $D(\mathbb{Z}_2)$ topologically ordered phases, driven by the condensation of the bosonic $1\bar{1}$ anyon. The critical behavior at the transition point is believed to fall into the 3D Ising CFT universality class [173, 174].

Next, we discuss the phases of the bilayer model away from the isotropic point $J_x = J_y = J_y = 1$. In the regime where J_z dominates over J_x and J_y with $\Delta > 0$, the system reduces to a bilayer toric code in perturbation theory, cf. (5.9). In this limit, the interlayer coupling Δ corresponds to the product of local terms from the two individual toric codes. A similar bilayer toric code model, albeit featuring a different Ising-like interlayer coupling, was analyzed in [175]. The authors identified a critical phase transition between a double toric code topological phase and a single toric code topological phase. An analogous transition is likely to occur in the anisotropic regime of our model when Δ is increased. When $J_x = 0$ and $J_y = J_z$, the bilayer model reduces to a stack of decoupled Ashkin-Teller chains, which are critical when $|\Delta| \leq 1$. Altogether, the triangular phase diagram of our bilayer Kitaev honeycomb model is expected to have the following structure for small $0 \leq \Delta \leq 1$:

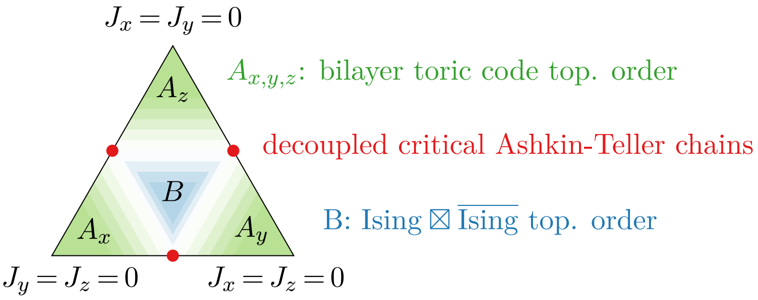

5.3.2 XXZ-Ising model from $\mathcal{M}$ = Ising

Next, we select the module tensor category $\mathcal{M} = \text{Ising}$ over $\mathcal{B}$ [176]. The resulting Hilbert space consists of qubits $\Gamma_i \in \{0,1\}$ on the trivalent vertices connected to ρ, and additional qubits $\Sigma_{ij} \in \{0,1\}$ on the red edges:

$$|\{\Gamma_i\},\{\Sigma_{i,j}\}\rangle = \tag{5.14}$$

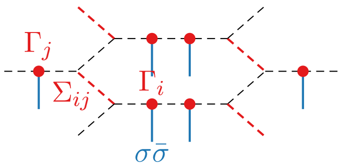

The dashed black lines are labeled by σ, while the blue vertical legs are labeled by $\sigma\bar{\sigma}$.

The Hamiltonian is derived by resolving each $\sigma\bar{\sigma}$ leg into two separate σ and $\bar{\sigma}$ legs and applying the standard F- and R-symbols of the Ising category. For example, the z-link term with $\lambda = 1\bar{0}$ can be computed as

$$H^{z,(1\bar{0})}_{i,j} : \quad = Y_i Z_j. \tag{5.15}$$

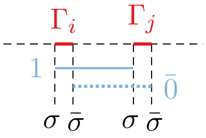

Following this procedure, the z-link terms corresponding to $\lambda = 0\bar{1}$ and $\lambda = 1\bar{1}$ can be derived similarly,

$$H^{z,(0\bar{1})}_{i,j} = Z_i Y_j, \quad H^{z,(1\bar{1})}_{i,j} = X_i X_j.$$

As before, the $1\bar{1}$-term is the product of the other two terms. With appropriate coupling constants and after a unitary rotation of the first qubit around the x-axis, the z-link Hamiltonian with all three terms is equal to the local XXZ Hamiltonian [23].

The x-link and y-link terms can be computed analogously. To render the Hamiltonian real, a unitary rotation U is applied to the Γ_i qubits on sublattice A of the bipartite honeycomb lattice and to all Σ_{ij} qubits,

$$U = \prod_{i \in A} e^{i\pi\sigma_i^x/4} \prod_{ij} e^{i\pi\sigma_{ij}^z/4}. \tag{5.16}$$

After this rotation, the entire Hamiltonian takes the form (with the same choice of signs as in (5.13)):

$$\begin{aligned} H = J_z \sum_{\substack{i,j \\ \in \text{z-link}}} (Z_i Z_j - Y_i Y_j - \Delta X_i X_j) + J_x \sum_{\substack{i,ik,k \\ \in \text{x-link}}} (Y_i X_{ik} Y_k - Z_i X_{ik} Z_k - \Delta X_i X_k) \\ + J_y \sum_{\substack{k,ik,lm,l \\ \in \text{y-link}}} \Big(Y_k Z_{ik} Z_{lm} Y_l - Z_k Z_{ik} Z_{lm} Z_l - \Delta X_k X_l \Big). \end{aligned} \tag{5.17}$$

This Hamiltonian resembles an XXZ model on the honeycomb lattice, but with additional qubits placed on certain links, coupled by Ising interactions. It is real and therefore preserves time-reversal symmetry.

By resolving all $\sigma\bar{\sigma}$ legs into separate σ and $\bar{\sigma}$ legs, as shown in (5.15), the model can also be interpreted as a regular $\mathcal{M} = \mathcal{B} =$ Ising fusion surface model, but defined on a different geometry and with longer-range interaction terms. Consequently, it preserves a $\mathbb{Z}_2$ 1-form symmetry, acting along the vertical incontractible loops as $\prod_{ij} X_{ij}$ and along the horizontal loops as $\prod_{ij} Z_{ij} \prod_i X_i$ (after the unitary rotation (5.16)). Since this 1-form symmetry is fermionic – and thus anomalous – it must be broken in all gapped phases (see Sections 5.1 and 4.5.2). In addition to the 0-form symmetries $\prod_{ij} X_{ij}$ and $\prod_i X_i$ generated by products of 1-form symmetry loops, we find an independent $\mathbb{Z}_2$ 0-form symmetry $\prod_i Z_i$ by inspection.

In the following, we provide arguments supporting the following phase diagram of the Hamiltonian (5.17):

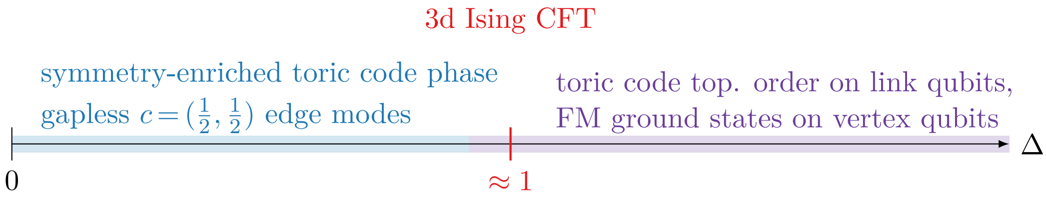

In the $\Delta \to \infty$ limit, the vertex qubits form two ferromagnetic ground states $\langle X_i \rangle = \pm 1$ which break the $\prod_i Z_i$ 0-form symmetry, while the link qubits fluctuate freely. The lowest order effective Hamiltonian acting on this ground state subspace appears at sixth order and is equal to the conserved plaquette operator (analogous to the perturbation theory analysis in [171] for the dual bilayer model),

$$H_p^{(\mathrm{eff})} \propto -\frac{J_x^2 J_y^2 J_z^2}{\Delta^5}$$

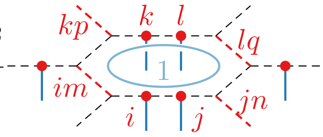

$$\xrightarrow{\text{unitary rotation (5.16)}} Y_{im} Z_{kp} Y_{lq} Z_{jn} (X_i X_j X_k X_l).$$

Since the product over the four X_i operators is always equal to $+1$ in the ferromagnetic ground states, this effective Hamiltonian is essentially the toric code Hamiltonian (in Wen's convention [177]) acting on the link qubits. Therefore, the large Δ phase has $D(\mathbb{Z}_2)$ topological order as well as a broken $\mathbb{Z}_2$ 0-form symmetry.

Characterizing the small Δ phase is more challenging, as it appears to resist analysis via standard perturbation theory. Based on the gauging analysis in [52], it is plausible that this phase corresponds to toric code topological order enriched by the unbroken $\mathbb{Z}_2$ 0-form symmetry. Their approach starts with a topological phase described by a UMTC $\mathcal{C}$ that also preserves an invertible 0-form symmetry G. Its symmetry-enriched class is described by a G-crossed braided tensor category $\mathcal{C}_G^X$, which incorporates both the anyons of $\mathcal{C}$ and extrinsic $\mathbf{g}$-defects (like the twist defects in Kitaev's honeycomb model reviewed in Section 4.4.3) that may permute the anyon types. Gauging G promotes these defects to deconfined excitations, resulting in a new topological order described by the equivariantization $(\mathcal{C}_G^X)^G$. The data of $(\mathcal{C}_G^X)^G$ can be derived mathematically from $\mathcal{C}_G^X$, independent of specific microscopic realizations.

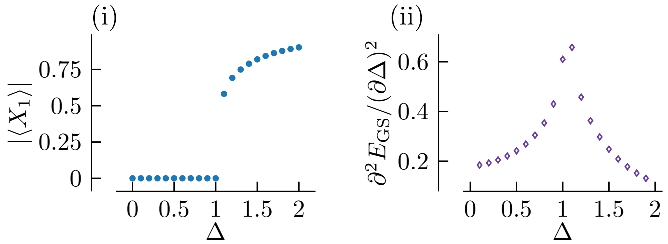

Figure 5.2: (i) Ferromagnetic order parameter $|\langle X_1\rangle|$ of the XXZ-Ising model (5.17) and (ii) second derivative of the ground state energy, computed with infinite DMRG on a $L_y = 2$ cylinder with bond dimension $D = 200$. The plots are for fixed $J_y = J_z = J_x = 1$.

In our case, $(\mathcal{C}_G^X)^G = \text{Ising} \boxtimes \overline{\text{Ising}}$ characterizes the topological order of the bilayer Kitaev honeycomb model at small Δ. This phase can arise from gauging a $\mathcal{C} = D(\mathbb{Z}_2)$ toric code phase with a $G = \mathbb{Z}_2$ symmetry that permutes the bosonic e and m anyons (see Section I.2 in [52]). We therefore conjecture that this $D(\mathbb{Z}_2)$ phase enriched by the $\mathbb{Z}_2$ symmetry $G = \prod_i Z_i$ describes the XXZ-Ising model at small Δ. The same phase has been realized in symmetry-enriched toric codes [178, 179]. On an open manifold, the XXZ-Ising model at small Δ must exhibit gapless non-chiral $c = (\frac{1}{2}, \frac{1}{2})$ edge modes to match the Ising edge modes of the dual bilayer model.

Since the $D(\mathbb{Z}_2)$ topological order remains unchanged across the critical point at $\Delta \approx 1$, this transition corresponds to spontaneous breaking of the $\mathbb{Z}_2$ 0-form symmetry. It should be governed by the 3d Ising CFT, just as the anyon condensation transition in the dual bilayer model. Numerical evidence for the critical transition is presented in Fig. 5.2, which shows the ferromagnetic order parameter alongside the second derivative of the ground-state energy. The DMRG algorithm spontaneously converges to one of the two ferromagnetic ground states, chosen at random. Consequently, we plot the expectation value $|\langle X_1\rangle|$ at the first site rather than a connected two-point correlation function.

Finally, we turn to the triangular phase diagram of the XXZ-Ising model away from the isotropic point. When J_z is dominant and $\Delta \geq 0$, vertex qubits on the same z-link form a unique dimer ground state $\frac{1}{\sqrt{2}}(|\uparrow\uparrow\rangle - |\downarrow\downarrow\rangle)$, minimizing the local interaction energy. The remaining degrees of freedom, represented by the link qubits, fluctuate. The effective Hamiltonian obtained via perturbation theory corresponds to a toric code Hamiltonian acting on these link qubits.

Although both the anisotropic and isotropic regimes are believed to host the same $D(\mathbb{Z}_2)$ topological order, they correspond to distinct phases, separated by a transition similar to that in the dual bilayer model between the Ising $\boxtimes\,\overline{\text{Ising}}$ and bilayer toric code phases. In the anisotropic regime, vertex qubits are frozen into z-link dimers and only link qubits contribute to the toric code order. Near the isotropic point however, both vertex and link qubits contribute to the toric code topological order. Gapless edge modes are expected in the isotropic phase, as in the bilayer Kitaev model, while the anisotropic regime is likely fully gapped. The simplest phase diagram consistent with this analysis for $0 \leq \Delta \leq 1$ is shown schematically in:

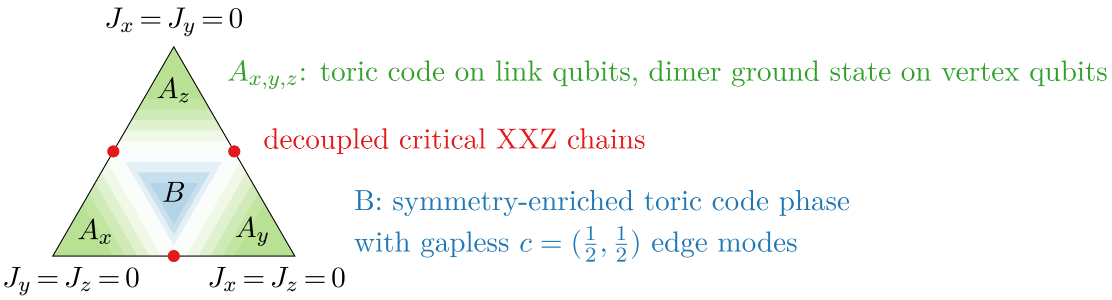

5.4 Symmetry fusion 2-category of dual models

We now discuss the 0-form and 1-form symmetries of dual fusion surface models using a higher Morita theory for fusion 2-categories. While regular $\mathcal{M} = \mathcal{B}$ fusion surface models conserve only 1-form symmetries and their condensation defects (as discussed in Section 4.1), the dual models with $\mathcal{M} \neq \mathcal{B}$ can support additional, independent 0-form symmetries. Identifying these 0-form symmetries and their lattice action is rather technical and has recently been investigated in [158].

We begin by reviewing a few mathematical facts about module tensor categories that will be useful for the subsequent symmetry analysis. Module tensor categories $\mathcal{M}$ over a braided fusion category $\mathcal{B}$ are also referred to as $\mathcal{B}$-enriched or $\mathcal{B}$-central tensor categories. For a detailed exposition, see [159, 180–183]. Following [159], a tensor category $\mathcal{M}$ becomes a module tensor category over a braided category $\mathcal{B}$ if it admits a braided functor

$$F^{\mathcal{Z}} : \mathcal{B} \to \mathcal{Z}(\mathcal{M}). \tag{5.18}$$

This functor equips $\mathcal{M}$ with the structure of a $\mathcal{B}$-module category through the action $b \triangleleft m \equiv F(b) \otimes m$ for $b \in \mathcal{B}$, $m \in \mathcal{M}$. Here, F is the composition of $F^{\mathcal{Z}}$ with the forgetful functor from $\mathcal{Z}(\mathcal{M})$ to $\mathcal{M}$. The functor $F^{\mathcal{Z}}$ also induces a half-braiding between objects in $\mathcal{B}$ and objects in $\mathcal{M}$.

In the physics literature, module tensor categories over braided fusion categories have been used to study boundaries of 3+1d Walker-Wang models [184] and $\mathcal{B}$-enriched string-nets [62, 185, 186]. Related mathematical structures known as orbifold data [187, 188] were employed in [189] to define so-called internal Levin-Wen models. Both the enriched string-nets and the internal Levin-Wen models are capable of realizing chiral topological order, in contrast to standard Levin-Wen string-nets.

An important class of examples are module tensor categories constructed from a commutative algebra object $A \in \mathcal{B}$ [159]. These are algebra objects (cf. (2.8)) that additionally satisfy the condition

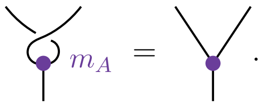

In this case, the category of A-modules in $\mathcal{B}$, denoted $\mathcal{M} = \mathrm{Mod}_{\mathcal{B}}(A)$, forms a module tensor category over $\mathcal{B}$. For instance, in Section 5.3.2, we used the module tensor category $\mathcal{M} = \mathrm{Ising}$ over $\mathcal{B} = \mathrm{Ising}\boxtimes\overline{\mathrm{Ising}}$, constructed from the commutative algebra object $A = 0\bar{0}\oplus 1\bar{1} \in \mathcal{B}$. When A is not commutative, the category $\mathrm{Mod}_{\mathcal{B}}(A)$ is still a valid module category, but not a tensor category itself. The free module functor $F : \mathcal{B} \to \mathcal{M} : F(x) = A \otimes x$ serves as the braided central functor in this construction. Commutative algebra objects in multiplicity-free modular fusion categories of rank up to 9 have been classified in [176, 190–192].

By analogy with 1+1d systems, the symmetry of the dual $(\mathcal{M}, \mathcal{B})$ fusion surface model is conjectured to correspond to the Morita dual of the fusion 2-category $\mathrm{Mod}(\mathcal{B})$ with respect to its module 2-category $\mathrm{Mod}(\mathcal{B})$ [23, 155, 193]. Formally, the Morita dual fusion 2-category is defined as [194, 195]:

$$\mathrm{Mod}(\mathcal{B})^{*}_{\mathrm{Mod}(\mathcal{M})} = \mathrm{End}_{\mathrm{Mod}(\mathcal{B})}(\mathrm{Mod}(\mathcal{M})). \tag{5.19}$$

Because braided fusion categories are known to be fully dualizable [181, 196], this fusion 2-category is guaranteed to exist. For 1-categories, the Morita dual $\mathcal{C}^*_{\mathcal{M}} = \mathrm{End}_{\mathcal{C}}(\mathrm{Mod}_{\mathcal{C}}(A))$ can be regarded as the category $\mathrm{Bimod}_{\mathcal{C}}(A)^{\mathrm{mop}}$ of A-A bimodules in $\mathcal{C}$, with "mop" indicating the multiplication opposite. Analogously, the dual fusion 2-category (5.19) is equivalent to [181, 194, 195]

$$\mathrm{Mod}(\mathcal{B})^*_{\mathrm{Mod}(\mathcal{M})} \simeq \mathrm{Bimod}_{\mathrm{Mod}(\mathcal{B})}(\mathcal{M})^{\mathrm{mop}}. \tag{5.20}$$

The fusion 2-category on the right-hand side represents the 2-category of $\mathcal{B}$-centered $\mathcal{M}$-$\mathcal{M}$-bimodule 1-categories [193]. This structure is discussed in Sections 3.5 and 3.6 of [181] and Section 3.4 of [197]. Its objects are $\mathcal{B}$-centered $\mathcal{M}$-$\mathcal{M}$-bimodules and 1-morphisms are functors between these bimodules. The term "$\mathcal{B}$-centered" implies the existence of an isomorphism $\eta : n \otimes b \simeq b \otimes n$ between objects n in the $\mathcal{M}$-$\mathcal{M}$-bimodule and objects $b \in \mathcal{B}$, subject to certain coherence conditions.

The 1-form symmetries of the lattice model correspond to the bimodule endofunctors of the monoidal unit of $\mathrm{Bimod}_{\mathrm{Mod}(\mathcal{B})}(\mathcal{M})^{\mathrm{mop}}$. The monoidal unit is $\mathcal{M}$ itself, equipped with its canonical $\mathcal{B}$-centered $\mathcal{M}$-$\mathcal{M}$-bimodule structure. By Lemma 3.2.1 in [194], its endomorphism 1-category is equivalent to

$$\mathrm{Bimod}_{\mathrm{Mod}(\mathcal{B})}(\mathcal{M})^0 \simeq \mathrm{Mod}\left(\overline{\mathcal{Z}_{\mathcal{B}}(\mathcal{M})}\right), \tag{5.21}$$

where the overline denotes the braiding opposite. The fusion 1-category $\mathcal{Z}_{\mathcal{B}}(\mathcal{M})$ is the subcategory of $\mathcal{Z}(\mathcal{M})$ consisting of objects that braid trivially with the image of $\mathcal{B}$ under the functor $F^{\mathcal{Z}}$ defined in (5.18). Physically, this condition implies that the 1-form symmetries can be deformed freely across the lattice [193].

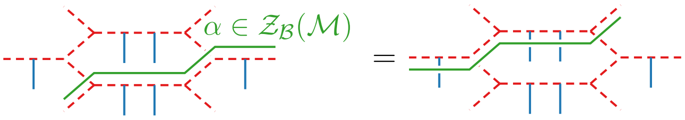

When $\mathcal{B}$ is non-degenerate, the Drinfeld center of $\mathcal{M}$ factorizes as [198]

$$\mathcal{Z}(\mathcal{M}) = \mathcal{B}^{\mathrm{mop}} \boxtimes \mathcal{Z}_{\mathcal{B}}(\mathcal{M}), \tag{5.22}$$

making the computation of $\mathcal{Z}_{\mathcal{B}}(\mathcal{M})$ straightforward.

If and only if the functor $\mathcal{F}^{\mathcal{Z}}$ is fully faithful, the symmetry fusion 2-category is connected and described by (5.21) (Corollaries 3.1.5 and 3.2.6 in [194]). In this case, there are no 0-form symmetries beyond the condensation defects associated with the 1-form symmetries in $\mathcal{Z}_{\mathcal{B}}(\mathcal{M})$. The fully faithfulness of $\mathcal{F}^{\mathcal{Z}}$ is assumed in the enriched string-net construction in [62, 186].

However, in general, $\mathcal{F}^{\mathcal{Z}}$ is not fully faithful. In such situations, the connected components of the symmetry fusion 2-category (5.20), corresponding to 0-form symmetries modulo condensation defects, remain incompletely understood and are only known in specific examples (cf. Remark 3.1.6 in [194]). Nonetheless, it is known that any fusion 2-category is Morita dual to a connected fusion 2-category $\mathrm{Mod}(\mathcal{B})$ (Theorem 4.2.2 in [194]). This means that any fusion 2-categorical symmetry can be realized as the symmetry of a ($\mathcal{M}$, $\mathcal{B}$) fusion surface model.

Next, we discuss some specific examples tied to the lattice models from earlier sections. For instance, when $\mathcal{B} = \mathrm{Rep}(G)$ and $\mathcal{M} = \mathrm{Vec}$, the dual fusion 2-category is

$$\mathrm{Bimod}_{\mathrm{Mod}(\mathcal{B})}(\mathcal{M}) \simeq 2\mathrm{Vect}_G, \tag{5.23}$$

which has $|G|$ connected components (see Example 5.1.9 in [195]). The XXZ honeycomb model, corresponding to $\mathcal{B} = \mathrm{Rep}(S_3)$ and $\mathcal{M} = \mathrm{Vec}$, realizes such a dual S_3 0-form symmetry.

For the XXZ-Ising model built from ($\mathcal{B} = \mathrm{Ising} \boxtimes \overline{\mathrm{Ising}}$, $\mathcal{M} = \mathrm{Ising}$), the symmetry fusion 2-category analysis above suggests the absence of both 0-form and 1-form symmetries: The functor $\mathcal{F}^{\mathcal{Z}} : \mathcal{B} \to \mathcal{Z}(\mathcal{M})$ is fully faithful since $\mathcal{B} \simeq \mathcal{Z}(\mathcal{M})$, implying a connected symmetry fusion 2-category $\mathrm{Mod}(\mathcal{Z}_{\mathcal{B}}(\mathcal{M}))$, which excludes independent 0-form symmetries. Moreover, $\mathcal{B}$ is non-degenerate and so the factorization of the Drinfeld center (5.22) implies $\mathcal{Z}_{\mathcal{B}}(\mathcal{M}) \simeq \mathrm{Vec}$, ruling out 1-form symmetries. The apparent discrepancy with the observed 1-form and 0-form symmetries (cf. Section 5.3.2) likely arises from the special nature of Ising fusion surface models. Specifically, certain planar edges in the Hilbert space are fixed to σ instead of being treated as dynamical degrees of freedom.

6

Conclusions

6.1 Summary of results

In this thesis, we have discussed how interesting quantum lattice models can be systematically constructed from fusion categories, and how this framework provides powerful tools to analyze their gapless, symmetry-broken, and topologically ordered phases.

We began with a detailed study of a particular 1+1d anyon chain, whose constrained Hilbert space admits a physical interpretation in terms of Rydberg-blockade atoms on a square ladder. Two ingredients were essential in understanding the physics of this integrable model: first, a duality mapping to the well-known spin-$\frac{1}{2}$ XXZ chain showed that the anyon chain is critical for $|\Delta| \leq 1$; second, the existence of a non-invertible self-duality symmetry, which is spontaneously broken for $\Delta > 1$, explained the degeneracy of three seemingly unrelated ground states. We then introduced perturbations to the Hamiltonian that explicitly break both integrability and the self-duality symmetry. Remarkably, a non-invertible remnant of the XXZ chain's $U(1)$ symmetry survives these perturbations and distinguishes two distinct $\mathbb{Z}_3$ density-wave phases in the Rydberg ladder. By establishing a correspondence between lattice and CFT operators, we predicted a narrow critical region near $\Delta = -1$. In a different parameter regime, our DMRG simulations indicate that the phase transition between the $\mathbb{Z}_3$ ordered and disordered phase likely belongs to the chiral clock model universality class, in agreement with earlier findings in the Rydberg chain.

Building on these 1+1d results, we turned to the fusion surface model construction introduced by Inamura and Ohmori [51] to systematically generalize Kitaev's honeycomb model using braided fusion categories. The resulting models possess categorical 1-form symmetries and mutually commuting conserved plaquette operators. Their phase diagrams are qualitatively similar to Kitaev's original model: in the anisotropic limit, they reduce to Levin-Wen string-net models, while in the isotropic limit, they are described by weakly coupled anyon chains and may realize chiral topological order. Kitaev's honeycomb model itself, both with and without a magnetic field perturbation, can be understood as a fusion surface model built from the Ising category. We recovered the $\mathbb{Z}_N$ generalization of Kitaev's model proposed by Barkeshli et al. [49] as the $\mathbb{Z}_N$ Tambara-Yamagami fusion surface model. The entanglement spectrum of the $\mathbb{Z}_3$ model in its isotropic phase, computed via infinite-cylinder DMRG, suggests chiral parafermion topological order. This is in agreement with the coupled-wire analysis in [49] for a related $\mathbb{Z}_3$ honeycomb model with fine-tuned interactions. Taking the Fibonacci category as input yields a novel honeycomb model with a non-invertible 1-form symmetry and explicit time-reversal breaking. In the anisotropic limit, this model realizes doubled Fibonacci topological order, while the isotropic phase—expected to be governed by weakly coupled critical Fibonacci chains—remains an open problem for further investigation.

The final chapter extends the fusion surface model framework to incorporate dualities between 2+1d quantum lattice models, which amount to gauging the categorical 1-form symmetries. The extended construction is closely inspired by analogous dualities in 1+1d anyon chains, where dual models arise from choosing different module categories – defining the Hilbert space – over a fixed fusion category that encodes the bond algebra of the Hamiltonian. In 2+1d, this generalizes to choosing different module tensor categories, i.e., module categories equipped with an intrinsic tensor product, over a given braided fusion category. Module tensor categories other than the original braided fusion category can lead to models with independent 0-form symmetries and potentially symmetry-enriched topological order. We examined two classes of examples. The first is a 2+1d analogue of the 1+1d example discussed previously, revealing a duality between an XXZ model on the honeycomb lattice and a constrained model with a $\mathrm{Rep}(S_3)$ 1-form symmetry. Unlike the 1+1d case, this constrained Hilbert space lacks a straightforward physical interpretation in terms of Rydberg-blockade atoms. The second example establishes a duality between a bilayer Kitaev honeycomb model and a spin-$\frac{1}{2}$ system with XXZ- and Ising-type interactions. This dual model supports both 0-form and 1-form $\mathbb{Z}_2$ symmetries and appears to realize a symmetry-enriched toric code phase.

6.2 Future directions

While our work represents a meaningful step toward enlarging the landscape of tractable 2+1d lattice models with non-commuting terms, several promising directions remain to be explored.

One direction for further exploration is the impact of generalized symmetries on quantum dynamics. One striking phenomenon is the presence of quantum scars: nonthermal eigenstates embedded within an otherwise thermalizing spectrum. These were first observed experimentally in a chain of Rydberg atoms, where certain initial states showed long-lived revivals [33]. The Rydberg chain can be theoretically described by the PXP model, a constrained bosonic system that forbids adjacent excitations [31, 67, 199] and is closely related to the Fibonacci anyon chain. A systematic study of scar states in anyon chains with integrability-breaking couplings remains an open challenge. In two spatial dimensions, spin-$\frac{1}{2}$ XXZ models on cubic lattices have been shown to exhibit exact spin-helix eigenstates, both theoretically [200–202] and experimentally [200]. More recently, a different class of quantum scars with spatially localized spin excitations has been identified in 2+1d XXZ models and via a duality mapping also in $\mathbb{Z}_2$ gauge theories [203]. It would be interesting to investigate whether these scar states persist under the duality mapping to the

Rep(S_3) fusion surface model. This may offer an example of dualities generating new examples of quantum scars, especially in higher-dimensional systems.

Second, the fusion surface model framework offers several opportunities for exploring aspects of 3d criticality. One such direction is the investigation of 2+1d self-dual points. In 1+1d anyon chains, self-dualities often serve as a useful guide for locating critical points. Extending this idea to 2+1d is appealing but more intricate: self-dualities now involve both 0-form and 1-form symmetries, which are exchanged under gauging. While a few examples of self-dual 2+1d lattice models have recently been identified [157, 204], the question of whether such self-dualities can signal criticality in 2+1d remains largely unexplored. A promising starting point might be the Tambara–Yamagami fusion 2-categories introduced in [205], which can serve as input data for fusion surface models. Another direction is to study phase transitions between different topological phases. These transitions are often driven by anyon condensation, a process in which a subset of anyons in a parent topological phase condenses to yield a phase with fewer anyonic excitations. In many known examples, these transitions are believed to be described by the 3d Ising CFT [52]—for example, the transition between the doubled Ising and toric code phases in the bilayer Kitaev honeycomb model (see Section 5.3.1). However, field theory descriptions of more exotic condensation transitions involving anyons with non-integer quantum dimensions as proposed in [206, 207] are still lacking. Studying these transitions in concrete lattice models, both analytically and numerically, may provide valuable new insights.

Finally, applying the categorical tools developed for topological phases in condensed matter to quantum error correction offers a promising avenue for future research. In dynamical Floquet codes, logical gates can be implemented by moving invertible domain walls across the system, corresponding to automorphisms of the underlying non-chiral topological order. This process can be regarded as an adiabatic path of gapped, topologically ordered Hamiltonians [208]. A prominent example is the honeycomb Floquet code of Hastings and Haah [209], which traces a continuous path in the phase diagram of a variant of Kitaev's model with bonds arranged in a Kekulé pattern [210, 211]. This Kekulé-modified model can also be written as an Ising fusion surface model with a slightly altered geometry. It might be interesting to explore Kekulé-patterned models built from other fusion categories, as a step toward constructing dynamical codes for non-abelian topological orders. Only recently have such non-abelian orders been employed in dynamic error-correcting codes to realize non-Clifford logical gates [212, 213].

Appendices

A

Rydberg-blockade ladder appendix

A.1 Perturbation theory calculations

Here we give a little more detail on the perturbation theory we use to correct the location of the phase transitions found by going to various extreme limits.

A.1.1 Ising^2 transition between D_4 and $\mathbb{Z}_2$ order

The Ising^2 Hamiltonian arises by neglecting creation and annihilation of + bosons, the first term in (3.5). Because the Ising Hamiltonian can be mapped on to a free-fermion model, its phase transitions can be located exactly. In our conventions, they are where the coefficient of the n_j^- term is half the magnitude of the $s_{j-1}s_{j+1}$ term. The best way to find the leading-order effect of the creation/annihilation term is thus to compute how it renormalizes the couplings while remaining in the Ising^2 Hilbert space. Acting with p_j moves out of this space, increasing the energy by $2(\Delta+t)$. Returning to the original Hilbert space by acting with $p_j^\dagger$ then results in an extra term $-p^\dagger p_j(1-w)^2/(2(\Delta+t))$ in the Hamiltonian. In this restricted Hilbert space, $p^\dagger p_j = (1-n_j^-)$. No other terms occur at order $(\Delta+t)$, so (3.21) is corrected to

$$\sum_{j=1}^{L}\left((1+w)s_{j-1}s_{j+1}+\left(\Delta-2t+\frac{(1-w)^2}{2(\Delta+t)}\right)n_j^-\right) \ .$$

The transition thus happens at (3.22).

To see how close the transition is this perturbative result , we use the level-crossing method (also used in e.g. [67]) to locate the Ising transition with exact diagonalization. The energy gap close to the transition is computed for L and $L-4$ and it is checked at which t the curves $L(\Delta E)_L$ and $(L-4)(\Delta E)_{L-4}$ cross for a given w and Δ. The numerical results for the locations of the Ising^2 transitions and the perturbation theory results (3.22) are plotted together in Fig. 3.5 for $w=0$.

A.1.2 First order transition between the $\mathbb{Z}_3$ phases

The correction to the first-order transitions we study is found simply by computing the corrections to the ground-state energies in the corresponding extreme limit. For $\Delta+t$ large and positive, the leading contributions to the energies of the $\mathbb{Z}_3^+$ ground state $|{+ee+ee}\ldots\rangle$ and $\mathbb{Z}_3^-$ ground state $|{-ee-ee}\ldots\rangle$ are

$$\epsilon_0^{3^+} = \frac{2L}{3}(\Delta+t) \ , \qquad \epsilon_0^{3^-} = L\Delta \ . \tag{A.1}$$

The $\mathbb{Z}_3^-$ ground states are exact, so they do not receive perturbative corrections. The leading correction to the $|{+ee+ee}\ldots\rangle$ is at second order through the annihilation and subsequent creation of a plus boson,

$$\epsilon_2^{3^+} = \frac{L}{3}\frac{(1-w)^2}{2(\Delta+t)}, \tag{A.2}$$

Hence the energy difference between the $\mathbb{Z}_3^+$ and $\mathbb{Z}_3^-$ ground states is

$$\epsilon_0^{3^+} + \epsilon_2^{3^+} - \epsilon_0^{3^-} = \frac{L}{3}\left(\Delta - 2t - \frac{(1-w)^2}{2(\Delta+t)}\right). \tag{A.3}$$

The transition occurs when this difference vanishes up to corrections of order $(\Delta+t)^2$, yielding the first of (3.25).

A.1.3 First-order transition between $\mathbb{Z}_3^-$ and $\mathbb{Z}_2$ phases

The $\mathbb{Z}_3^-$ and Z_2 phases both can occur as $\Delta \to -\infty$ and $t \to +\infty$. In this limit, the $\mathbb{Z}_2$-phase ground state is $|{-e-e}\ldots\rangle$, with zeroth order energy

$$\epsilon_0^{2^-} = \frac{L}{2}(\Delta - 2t). \tag{A.4}$$

The first order correction to the energy vanishes, but the second-order correction due to flipping a minus boson to a plus boson and back is given by

$$\epsilon_2^{2^-} = \frac{L}{2}\frac{(1+2w)^2}{2(\Delta-2t)}, \tag{A.5}$$

The energy difference between this ground state and the ground state of the $\mathbb{Z}_3^-$ phase is therefore

$$\epsilon_0^{3^-} - \left(\epsilon_0^{2^-} + \epsilon_2^{2^-}\right) = L\left(\frac{\Delta}{2} + t - \frac{(1+2w)^2}{4(\Delta-2t)}\right).$$

Requiring this vanish yields the second part of (3.25) for $t \approx -\Delta/2$. In fact, we find that the formula holds even when $|\Delta|$ becomes order one, as apparent in Fig. 3.2. Pushing it even further, setting $t=0$ we obtain $w \approx (\sqrt{2}\Delta - 1)/2$, which agrees well with the numerical results in Fig. 3.7(i).

A.1.4 First-order transition between the $\mathbb{Z}_2$ ordered and disordered phases

The spontaneously broken self-duality along the integrable $w=t=0$ line for $\Delta > 1$ results in a first-order phase transition between the $\mathbb{Z}_2$ ordered phase and the disordered phase. We here show how the location of this transition changes for non-vanishing w and t. We assume both $\Delta - 2t$ and $\Delta + t$ large and positive so that the off-diagonal terms in H in the ± basis are small relative to the diagonal terms. In this limit, the $\mathbb{Z}_2$ ground states are $|{+e+e\dots}\rangle$ and its translation, while the disordered ground state is $|e\,e\,e\,\dots\rangle$. Both have energy zero at leading order. Second-order corrections to the latter are

$$\epsilon_2^{\mathrm{dis}} = -L\frac{(1-w)^2}{2(\Delta+t)}\ . \tag{A.6}$$

while contributions to the former come from both off-diagonal terms

$$\epsilon_2^{+} = -\frac{L}{2}\frac{(1+2w)^2}{2(\Delta-2t)} - \frac{L}{2}\frac{(1-w)^2}{2(\Delta+t)}\ . \tag{A.7}$$

At the first-order transition $\epsilon_2^{\mathrm{dis}} = \epsilon_2^{2^+}$ yielding

$$\frac{(1+2w)^2}{\Delta-2t} = \frac{(1-w)^2}{\Delta+t}\ . \tag{A.8}$$

Solving for t gives (3.27).

The assumption in deriving (A.8) was that all terms in $\epsilon_2^{\mathrm{dis}}$ and $\epsilon_2^{2^+}$ remain small in magnitude. However, when comparing with our numerics in Fig. 3.6, we saw that agreement is good even when the denominators in (A.6) and (A.7) vanish. The reason is that in setting $\epsilon_2^{\mathrm{dis}} = \epsilon_2^{2^+}$ to obtain (A.8), we force the numerators to vanish at these points as well. Thus at these special points $(t,\, w) = (-\Delta, 1)$ and $(\Delta/2, -1/2)$, the values of each side of (A.8) are still order $1/\Delta$ (they are $3/\Delta$ and $3/(2\Delta)$ respectively). Thus at large enough Δ, the curve (3.27) should still accurately describe the location of the transition. We found even $\Delta = 2.5$ works reasonably well, cf. Fig. 3.6.

A.2 The quantum Ashkin-Teller model

A.2.1 Mapping to the XXZ chain

The Ashkin-Teller model describes two Ising models on the same lattice coupled across each of the bonds. The quantum Hamiltonian is built from two sets of Pauli matrices acting on each site of the chain. We include a symmetry interchanging the two chains, so the Hamiltonian is

$$H_{\mathrm{AT}} = -\sum_{j=1}^{L} \Big(\sigma_j^z \sigma_{j+1}^z + \beta \sigma_j^x + \tau_j^z \tau_{j+1}^z + \beta \tau_j^x - \Delta (\sigma_j^z \sigma_{j+1}^z \tau_j^z \tau_{j+1}^z + \beta \sigma_j^x \sigma_{j+1}^x) \Big). \tag{A.9}$$

The ensuing D_4 symmetry generators include both spin-flip symmetries

$$F_\sigma = \prod_{j=1}^{L} \sigma_j^x \ , \quad F_\tau = \prod_{j=1}^{L} \tau_j^x \ , \tag{A.10}$$

along with chain exchange. At the self-dual point $\beta = 1$, the Hamiltonian (A.9) can be split up as

$$H_{\mathrm{AT}} = -\sum_{k=1}^{2L} \left(S_k + \Delta P_k \right) \ , \tag{A.11}$$

where the $2L$ operators

$$\begin{aligned} S_{2j} &= \tfrac{1}{2} \left(\sigma_j^x + \tau_j^x \right), \quad & S_{2j+1} &= \tfrac{1}{2} \left(\sigma_j^z \sigma_{j+1}^z + \tau_j^z \tau_{j+1}^z \right), \\ P_{2j} &= \tfrac{1}{2} \left(\mathbb{I} - \sigma_j^x \tau_j^x \right), \quad & P_{2j+1} &= \tfrac{1}{2} \left(\mathbb{I} - \sigma_j^z \sigma_{j+1}^z \tau_j^z \tau_{j+1}^z \right). \end{aligned}$$

satisfy the same algebra (3.9) as the local terms (3.8) in the XXZ chain.

Since their generators obey the same algebra, we expect that there exists a non-invertible duality between the Ashkin-Teller and XXZ chains. This duality is found by orbifolding a 4-state height-model version of the 6-vertex model with $2L$ sites [84]. The height model has four heights $h_j \in \{1,2,3,4\}$ on each site $j = 1,\dots,2L$ that obey the constraint $h_{j+1} = h_j \pm 1$. The two domain walls between adjacent heights correspond to the XXZ degrees of freedom. Orbifolding by the $\mathbb{Z}_2$ symmetry $2 \leftrightarrow 4$ in the height model yields the Ashkin-Teller model:

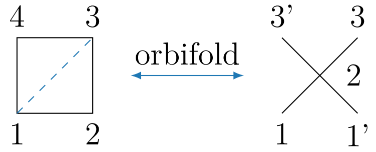

(A.12)

The Ashkin-Teller adjacency diagram requires that every state $s_j \in \{1,1',3,3'\}$ is adjacent to a state $s_{j+1} = 2$. Hence effectively, the sublattice with the $s_{2j} = 2$ states can be neglected, and the Ashkin-Teller model can be defined on the sublattice $s_{2j+1} \in \{1,1',3,3'\}$. The states 1, $1'$, 3, $3'$ are identified with the σ^z, τ^z eigenstates in the quantum model:

$$\begin{aligned} 1 &\to |0\rangle_\sigma |0\rangle_\tau , \quad & 1' &\to |1\rangle_\sigma |1\rangle_\tau , \\ 3 &\to |0\rangle_\sigma |1\rangle_\tau , \quad & 3' &\to |1\rangle_\sigma |0\rangle_\tau . \end{aligned} \tag{A.13}$$

This orbifold mapping from XXZ to Ashkin-Teller is equivalent to applying Kramers-Wannier duality to one sublattice [89]. The map then can be written as a matrix-product operator, with weights given by

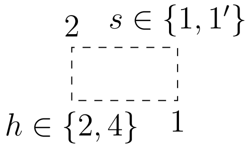

$$= 2^{-1/4}(-1)^{\delta_{h4}\delta_{s1}},$$

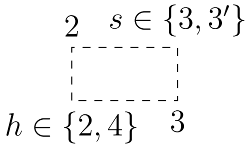

$$= 2^{-1/4}(-1)^{\delta_{h4}\delta_{s3}}.$$

(A.14)

It is useful to consider the combinations $|\pm\rangle_1$ and $|\pm\rangle_3$ which are simultaneous eigenstates of $\sigma^x_j\tau^x_j$ and $\sigma^z_j\tau^z_j$:

$$\begin{aligned}\left|\pm\right\rangle_1 &= \frac{1}{\sqrt{2}}\Big(\left|0\right\rangle_\sigma \left|0\right\rangle_\tau \pm \left|1\right\rangle_\sigma \left|1\right\rangle_\tau \Big),\\ \left|\pm\right\rangle_3 &= \frac{1}{\sqrt{2}}\Big(\left|0\right\rangle_\sigma \left|1\right\rangle_\tau \pm \left|1\right\rangle_\sigma \left|0\right\rangle_\tau \Big).\end{aligned} \tag{A.15}$$

Knowing three successive heights (h_{j-1}, h_j, h_{j+1}) in the 4-state height model gives the state s_j in the quantum Ashkin-Teller model via

$$\begin{aligned}&\{\left|BAB\right\rangle, \left|DAD\right\rangle\} \to \left|+\right\rangle_1, \ \{\left|BCB\right\rangle, \left|DCD\right\rangle\} \to \left|+\right\rangle_3,\\ &\{\left|BAD\right\rangle, \left|DAB\right\rangle\} \to \left|-\right\rangle_1, \ \{\left|BCD\right\rangle, \left|DCB\right\rangle\} \to \left|-\right\rangle_3.\end{aligned}$$

When $\beta \neq 1$, applying the Kramers-Wannier transformation to the τ spins in the Ashkin-Teller model, followed by applying it to both σ and τ spins yields the staggered XXZ chain [89],

$$H = \sum_{j=1}^{L} \left(1 + (-1)^j\right) \left(\sigma^x_j\sigma^x_{j+1} + \sigma^y_j\sigma^y_{j+1} + \Delta\sigma^z_j\sigma^z_{j+1}\right). \tag{A.16}$$

A.2.2 Non-invertible symmetries

We expect that as in the Rydberg ladder, the square of the $U(1)$ charge of the XXZ height model can be mapped to the Ashkin-Teller model. We find this non-invertible charge to be

$$\mathcal{Q}_{\mathrm{AT}} = \frac{1}{2}\left(1 + F_\sigma F_\tau\right) \sum_{j=1}^{L}\sum_{k=0}^{L-1} (-1)^{k+1} \prod_{l=0}^{k} \left(\sigma^x_{j+l}\tau^x_{j+l}\right) . \tag{A.17}$$

The charge $\mathcal{Q}_{\mathrm{AT}}$ is non-vanishing only in half the Hilbert space, as $F_\sigma F_\tau \mathcal{Q}_{\mathrm{AT}} = \mathcal{Q}_{\mathrm{AT}}$.

Applying Kramers-Wannier duality to both σ and τ spins gives rise to a duality under which $\beta \to 1/\beta$. This is reminiscent of the $w \to -w$, $t \to -t$ duality in the Rydberg ladder.

A.2.3 Ground states and symmetry breaking

In the limit $\Delta \to -\infty$, the two ground states of (A.9) have eigenvalue -1 under $\sigma^x_j\tau^x_j$ and $\sigma^z_j\sigma^z_{j+1}\tau^z_j\tau^z_{j+1}$ for all j, and so are

$$\left|-_1 -_3 -_1 -_3 \ldots\right\rangle, \quad \left|-_3 -_1 -_3 -_1 \ldots\right\rangle. \tag{A.18}$$

These states are exact eigenstates of the Hamiltonian, and so they persist for any finite $\Delta < -1$. They spontaneously break $\mathbb{Z}_2$ translation symmetry, and they have the maximal charge $\mathcal{Q}_{\mathrm{AT}} = L$ under the non-invertible $U(1)$ symmetry (A.17).

For $\Delta \to \infty$, the two ground states of (A.9) instead have eigenvalue 1 under these operators, and so are

$$|+_1 +_1 +_1 +_1 \ldots\rangle \,, \quad |+_3 +_3 +_3 +_3 \ldots\rangle \,. \tag{A.19}$$

These two ground states are mixed by the symmetry generators F_σ and F_τ, and so the D_4 symmetry is thus spontaneously broken in this phase. Translation symmetry, however, is preserved.

A.2.4 Field theory of the quantum Ashkin-Teller chain

To understand the transition between the D_4-broken phase and the $\mathbb{Z}_2$-broken phases here, we study the effective field theory outside of the critical regime. Using the mapping to the staggered XXZ chain, this field theory can be derived with the Coulomb-gas approach [89]. We here restate these results in the CFT language. The critical regime of the Ashkin-Teller model is described by a free-boson orbifold CFT with radius [214]

$$\Delta = -\cos\left(\frac{\pi r^2}{2}\right), \tag{A.20}$$

which is twice the radius of the corresponding XXZ chain. In the region near its critical line, the effective field theory describing the continuum limit of the Ashkin-Teller chain in the region near the critical line can be written as a perturbed CFT. The only operators invariant under both translation and the non-invertible $U(1)$ symmetry are $C_{0,2n}$, so the resulting effective Hamiltonian is

$$H_{\mathrm{CFT}} + \int dx\, \Big(\lambda_1 C_{0,2}(x) + \lambda_2 C_{0,4}(x)\Big). \tag{A.21}$$

The critical line extends into a critical fan when both perturbations are irrelevant, as with our Rydberg-blockade ladder. Here that occurs when $r^2 < 1/2$ ($\Delta < -1/\sqrt{2}$). At larger values of Δ, $1/2 < r^2 < 2$ ($-1/\sqrt{2} < \Delta < 1$), the operator $C_{2,0}$ is relevant and the model is critical only at $\beta = 1$. At $r^2 = 2$ ($\Delta = 1$), the operator $C_{0,4}$ with scaling dimension $4/r^2$ becomes relevant and drives a KT transition.

B

Fusion surface models appendix

B.1 Unitary mapping of the J_x–J_z chain to the Ising anyon chain with twisted boundary conditions

Here we work out the unitary transformation described in (4.14), (4.12), (4.13) for the Ising input category. The terms in the J_x–J_z chain have the form

$-J_y$

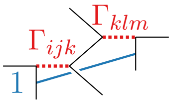

$-J_z$

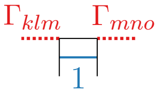

so the Hamiltonian for a $L = 4$ chain is

$$H = -J_y Y_1 X_2 - J_z Z_2 Z_3 - J_y Y_3 X_4 - J_z Z_4 Z_1. \tag{B.1}$$

The Hamiltonian (B.1) shares the same bond algebra as the periodic $L = 2$ Ising chain,

$$H^{\text{Ising}} = X_1 + Z_1 Z_2 + X_2 + Z_2 Z_1,$$

and so has the same spectrum. Note, however that it acts on four qubits, and so each level must have degeneracies. Indeed, the Ising chain has no symmetries beyond the usual spin-flip symmetry generated by $X_1 X_2$. The one-form symmetries of (B.1) yield three $\mathbb{Z}_2$ conserved charges, namely $Z_1 Z_2$, $Z_3 Z_4$ and $Y_1 X_2 Y_3 X_4$.

We apply the unitary transformation (4.12) to move one of the additional σ-legs to the right:

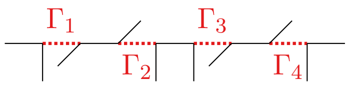

$$\xrightarrow{U_{\Gamma_2\Gamma_{2'}}=[F_\sigma^{\sigma\sigma\sigma}]_{\Gamma_2\Gamma'_2}}$$

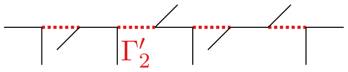

The Hamiltonian (B.1) therefore transforms to

$$U_2HU_2^\dagger = J_yY_1Z_2 + J_zX_2Z_3 + J_yY_3X_4 + J_zZ_4Z_1 \quad \text{with } U_2 = \frac{1}{\sqrt{2}}\begin{pmatrix}1 & 1\\ 1 & -1\end{pmatrix} \tag{B.2}$$

where here and below the matrices are written in the Z-diagonal basis on the corresponding site(s). The same σ-leg is moved to the right once more,

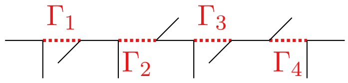

$$\xrightarrow{U_{\Gamma_2\Gamma_3}=[F_\sigma^{\Gamma_2\sigma\Gamma_3}]_{\sigma\sigma}}$$

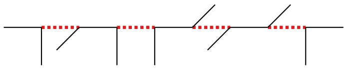

This transforms the Hamiltonian (B.2) to

$$U_{23}U_2HU_2^\dagger U_{23}^\dagger = J_yY_1Z_2 + J_zX_2 + J_yZ_2Y_3X_4 + J_zZ_4Z_1 \quad \text{with } U_{23} = \begin{pmatrix}1 & & & \\ & 1 & & \\ & & 1 & \\ & & & -1\end{pmatrix}. \tag{B.3}$$

Next, the other σ-leg is moved to the right,

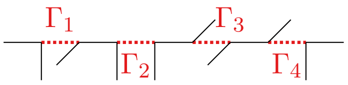

$$\xrightarrow{U_{\Gamma_1\Gamma_2}=[F_\sigma^{\Gamma_1\sigma\Gamma_2}]_{\sigma\sigma}R_\sigma^{\sigma\Gamma_2}(R_{\Gamma_3}^{\sigma\sigma})^{-1}}$$

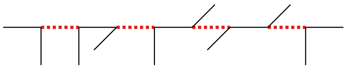

transforming the Hamiltonian (B.3) to

$$\begin{aligned} U_{12}U_{23}U_2HU_2^\dagger U_{23}^\dagger U_{12}^\dagger &= J_yX_1 + J_zZ_1Y_2 + J_yZ_2Y_3X_4 + J_zZ_4Z_1 \\ \text{with } U_{12} = e^{i\pi/8}&\begin{pmatrix}1 & & & \\ & i & & \\ & & i & \\ & & & 1\end{pmatrix}. \end{aligned} \tag{B.4}$$

This σ-leg is moved to the right once more,

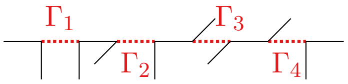

$$\xrightarrow{U_{\Gamma_2\Gamma'_2}=[F_\sigma^{\sigma\sigma\sigma}]_{\Gamma_2\Gamma'_2}R_\sigma^{\sigma\Gamma_2}(R_{\Gamma'_2}^{\sigma\sigma})^{-1}}$$

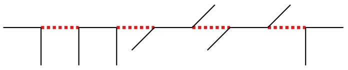

The transforms the Hamiltonian (4.13) to

$$\begin{aligned} U_2U_{12}U_{23}U_2HU_2^\dagger U_{23}^\dagger U_{12}^\dagger U_2^\dagger &= J_yX_1 + J_zZ_1Z_2 + J_yY_2Y_3X_4 + Z_4Z_1 \\ \text{with } U_2 = e^{i\pi/8}&\begin{pmatrix}1 & i\\ i & 1\end{pmatrix}. \end{aligned} \tag{B.5}$$

The spectrum of course remains the same as that of the $L=2$ Ising chain, and the three $\mathbb{Z}_2$ symmetries are generated by Y_3, Z_2Z_4, and $X_1X_2Y_4$. As demonstrated in the main text, the extras are the remnants of the plaquette 1-form symmetries.

B.2 Derivation of the Ising fusion surface model

In the Ising category, the quantum dimensions of the objects are $d_1 = d_0 = 1$ and $d_\sigma = \sqrt{2}$ and the non-trivial F-symbols and R-symbols are

$$[F_1^{\sigma 1 \sigma}]_{\sigma\sigma} = [F_\sigma^{1\sigma 1}]_{\sigma\sigma} = -1,\ F_\sigma^{\sigma\sigma\sigma} = \frac{1}{\sqrt{2}}\begin{pmatrix} 1 & 1 \\ 1 & -1 \end{pmatrix},$$
$$R_0^{11} = -1,\ R_\sigma^{1\sigma} = R_\sigma^{\sigma 1} = -i,\ R_0^{\sigma\sigma} = e^{\frac{-i\pi}{8}},\ R_1^{\sigma\sigma} = e^{\frac{3\pi i}{8}}.$$

The z-link term in the Hamiltonian (4.18) can be evaluated by fusing the 1-line to the horizontal edge, using F-moves, and removing bubbles:

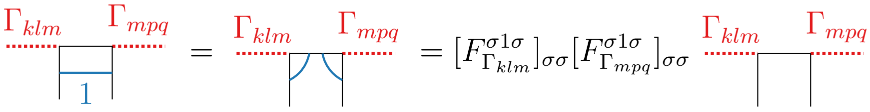

In operator form, this is

$$H^z_{klm,mpq} = Z_{klm}Z_{mpq}.$$

The x-link term can be evaluated similarly,

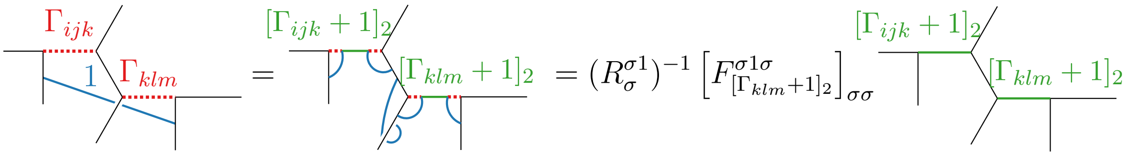

Here $[\cdot]_2$ denotes addition modulo 2, and only the non-trivial F-symbols are written down. As an operator,

$$H^x_{ijk,klm} = iZ_{klm}X_{klm}X_{ijk} = -Y_{klm}X_{ijk}.$$

Analogous to the x-link term, the y-link term yields

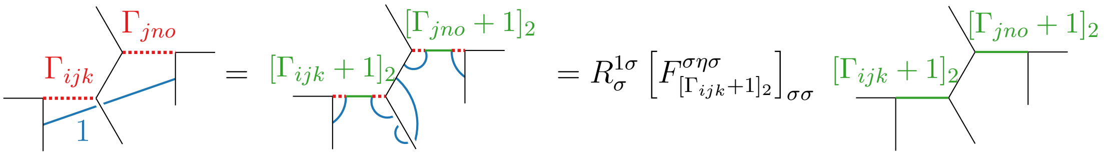

In operator form,

$$H^{y}_{ijk,jno} = (-i) Z_{ijk} X_{ijk} X_{jno} = Y_{ijk} X_{jno}.$$

The entire Hamiltonian is then

$$H = -J_x \sum_{b,a \in \text{x-link}} (-Y_b X_a) - J_y \sum_{a,c \in \text{y-link}} Y_a X_c - J_z \sum_{b,d \in \text{z-link}} Z_b Z_d,$$

with the vertices of the honeycomb lattice now labeled by single letters $a, b, \ldots$ for brevity.

B.3 Square lattice $\mathbb{Z}_3$ model in the fusion category framework

The $\mathbb{Z}_3$ symmetric lattice model studied in [131] is believed to realize chiral parafermion topological order $\mathbb{Z}_3 \boxtimes \text{Fib}$ in its triangular lattice limit. In terms of lattice parafermions, it can be expressed as

$$\begin{aligned} H = \sum_{n=1}^{L_y} H^{(n)}_{\text{1d}} + \sum_{n} H^{(n,n+1)}_{\text{inter}}, \text{ with } H^{(n)}_{\text{1d}} &= -t_3 \sum_j \left(\omega \hat{\alpha}^{(n)\dagger}_{R,j+1} \hat{\alpha}^{(n)}_{R,j} + \text{h.c.} \right) \text{ and} \\ H^{(n,n+1)}_{\text{inter}} &= -\sum_j \left(t_1 \omega \hat{\alpha}^{(n)\dagger}_{L,j} \hat{\alpha}^{(n+1)}_{R,j} + t_2 \omega \hat{\alpha}^{(n)\dagger}_{L,j} \hat{\alpha}^{(n+1)}_{R,j-1} + \text{h.c.} \right). \end{aligned} \tag{B.6}$$

The 1d Hamiltonians are decoupled Potts models, and their lattice parafermions are known in the fusion category framework, cf. (4.32). The complex phases in (B.6) are necessary to have charge conjugation symmetry. The triangular lattice limit corresponds to choosing $t_1 = t_2$ in (B.6), so that the field theory expansion of the inter-chain coupling only contains the parafermion operator $\bar{\psi}^\dagger \psi$, cf. (4.35). Writing down the Hamiltonian (B.6) in operator form requires choosing a parafermion path. We take the same path that was used for the numerical simulations in [131], depicted in Fig. 20 in [131], and also fix $L_y = 4$ and open boundary conditions in the y-direction. With the parafermion definitions in [131], one unit cell of the Hamiltonian (B.6) can then be written as

$$\begin{aligned} H = {} & t_1 \left(\tau_1 + \sigma_2 \sigma_1^\dagger + \tau_2 \right) + t_2 \left(\sigma_1 \tau_2 \sigma_3^\dagger + \sigma_2 \tau_2 \tau_3^\dagger \sigma_3^\dagger + \sigma_2 \tau_3^\dagger \sigma_4^\dagger \right) \\ & + t_3 \left(\omega \sigma_1 \tau_1 \tau_2 \sigma_3^\dagger + \omega^2 \sigma_1 \tau_2 \tau_3^\dagger \sigma_3^\dagger + \omega \sigma_2 \tau_2 \tau_3^\dagger \sigma_4^\dagger + \omega^2 \sigma_2 \tau_3^\dagger \tau_4^\dagger \sigma_4^\dagger \right) + \text{h.c.} \end{aligned} \tag{B.7}$$

Using the graphical expressions (4.32) for the parafermions, the unit cell Hamiltonian (B.6) can be depicted as follows:

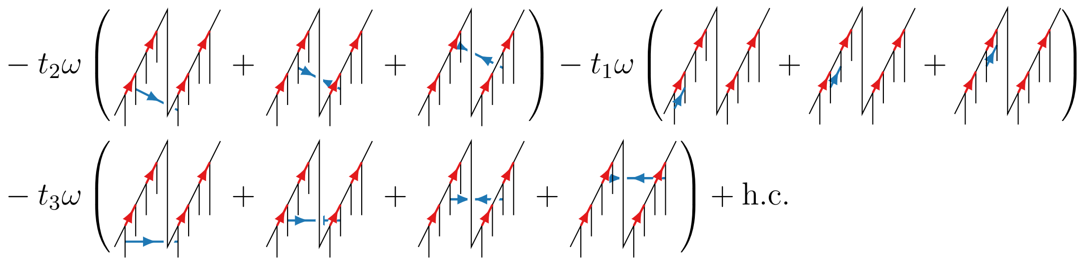

So the Hamiltonian (B.6) can be regarded as an anyon chain with long range interactions. Unlike the fusion surface models, such anyon chain models do not have conserved plaquette operators. An anyon chain model very similar to (B.6) but with coupling

$$-t_4\omega\sum_j\left(\hat{\alpha}^{(n)}_{L,2j-1}\hat{\alpha}^{(n+1)\dagger}_{R,2j}+\text{h.c.}\right)=-t_4\omega\sum_j$$

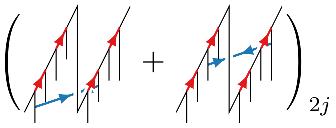

$$+\ \text{h.c.}$$

corresponding to the parafermion coupling (4.34) has the same energies as the $\mathbb{Z}_3$ fusion surface model (4.26) (but smaller degeneracies).

B.4 Details on the DMRG simulations of the $\mathbb{Z}_3$ models

We use Tenpy [134, 135] for infinite DMRG simulations on the cylinder. Before computing the entanglement spectra of the $\mathbb{Z}_3$ honeycomb model (4.30), we reproduce the entanglement spectra of the $\mathbb{Z}_3$ square lattice model (B.7) studied in [131] to ensure that our numerical methods are reliable. For the square lattice model (B.7), the DMRG unit cell is $L_x = 2$ and $\mathbb{Z}_3$ symmetry is conserved in the simulation (note that the conservation of energies can influence which entanglement energies appear in the spectrum [215]). The results are shown in Fig. B.2 for (i) $t_3 = 1$ and (ii) $t_3 = -1$, both with different $t_1 = t_2$. While the values of the entanglement energies vary with $t_1 = t_2$, their degeneracies remain the same. When $t_3 = 1$, the degeneracy pattern $(1, 2, 2, 1, \dots)$ is consistent with chiral parafermion order, see (4.38). When $t_3 = -1$, the pattern $(1, 2, 1, 4, \dots)$ is consistent with

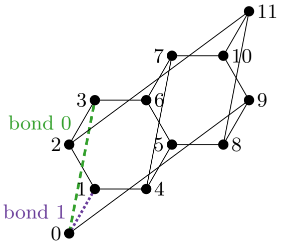

Figure B.1: The geometry of the MPS used in our Tenpy infinite DMRG simulations for $L_x = 3$ and $L_y = 2$. The entanglement spectra are computed across bond 0 (dashed green line) and across bond 1 (dotted violet line) for even and odd L_y respectively.

chiral $U(1)_6$ topological order. The presence of chiral $U(1)_6$ topological order is not surprising because the square lattice model with negative t_3 reduces to decoupled antiferromagnetic Potts models described by the $U(1)_6$ CFT when $t_1 = t_2 = 0$. In the chiral $U(1)_6$ phase, there are two ground states with different entanglement energies [131], so randomizing the initial state is essential to find the ground state that gives rise to the $(1, 2, 1, 4, \dots)$ pattern.

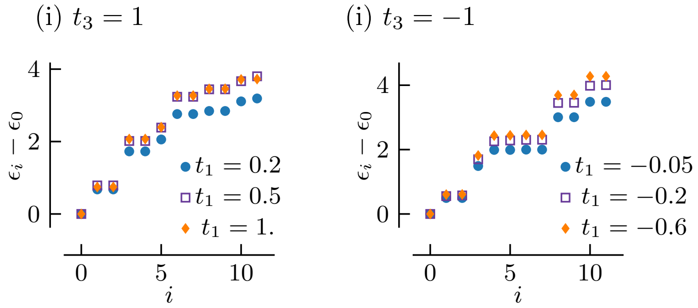

Figure B.2: Entanglement energies ϵ_i of the $\mathbb{Z}_3$ square lattice model (B.7) with (i) $t_3 = 1$ (chiral parafermion phase) and (ii) $t_3 = -1$ (chiral $U(1)_6$ phase) and different $t_1 = t_2$ on an infinite cylinder with bond dimension $D = 400$.

Next we simulate the the $\mathbb{Z}_3$ honeycomb model and choose a unit cell of $L_x = 3$ following [95]. First we checked that the fusion surface models (4.29) with $N = 3$, $p = 1$ and $p = 2$ have the same energies and entanglement spectrum as the model (4.30) on an infinite cylinder (albeit having slightly different finite-size energies). Therefore we focus on the Hamiltonian (4.30) in subsequent simulations. Its entanglement spectrum at the isotropic point is shown in Fig. 4.3, and it shows the $(1, 2, 2, 1, \dots)$ degeneracies characteristic of chiral parafermion topological order. On the $L_y = 2$ and $L_y = 4$ cylinder, the entanglement cut is across bond 0, which is the canonical choice, but on the $L_y = 3$ cylinder, the cut goes across bond 1 in order to recover the same degeneracies, see Fig. B.1. This is probably due to an even vs. odd effect of the honeycomb model on an infinite cylinder. The entanglement spectra for $L_y = 3$, $J_y = J_z = 1$ and different J_x are shown in Fig. B.3(i). Also, we show the entanglement spectra for $L_y = 4$ and $J_y = J_z = -1$ in Fig. B.3(ii) and observe that the degeneracies follow the $(1, 2, 1, 4, \dots)$ pattern expected for $U(1)_6$ (though $U(1)_{12}$ has very similar degeneracies $(1, 2, 1, 2, 2, \dots)$ and cannot be ruled out).

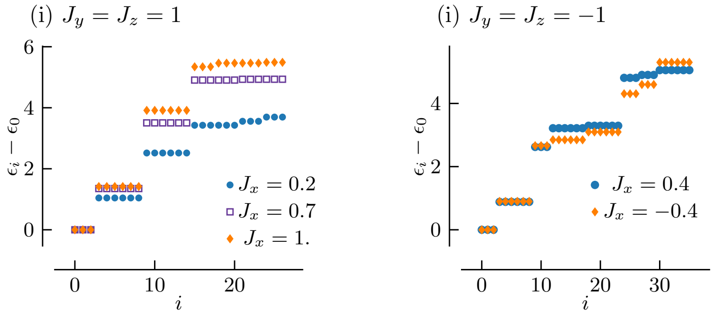

Figure B.3: Entanglement energies ϵ_i of the $\mathbb{Z}_3$ honeycomb model (4.30) with (i) $J_y = J_z = 1$ (likely chiral parafermion phase), $D = 800$, $L_y = 3$ and the entanglement cut across bond 1, (ii) $J_y = J_z = -1$ (likely chiral $U(1)_6$), $D = 1000$, $L_y = 4$, entanglement cut across bond 0.

B.5 Derivation of the Fibonacci fusion surface model

To derive the Hamiltonian explicitly, we use the F-symbols and R-symbols of the Fibonacci category,

$$F_\tau^{\tau\tau\tau} = \begin{pmatrix} \phi^{-1} & \phi^{-1/2} \\ \phi^{-1/2} & -\phi^{-1} \end{pmatrix} = \left(F_\tau^{\tau\tau\tau}\right)^{-1}, \; R_1^{\tau\tau} = e^{-4\pi i/5}, \; R_\tau^{\tau\tau} = e^{3\pi i/5}, \; d_\tau = \phi,$$

where $\phi = (1 + \sqrt{5})/2$ is the golden ratio. In addition, we define the following matrix operators in the $\{1, \tau\}$ basis,

$$\sigma^x = \begin{pmatrix} 0 & 1 \\ 1 & 0 \end{pmatrix}, \; n = \begin{pmatrix} 0 & 0 \\ 0 & 1 \end{pmatrix}, \; \tilde{n} = \begin{pmatrix} 1 & 0 \\ 0 & 0 \end{pmatrix}, \; \sigma^- = \begin{pmatrix} 0 & 1 \\ 0 & 0 \end{pmatrix}, \; \sigma^+ = \begin{pmatrix} 0 & 0 \\ 1 & 0 \end{pmatrix}.$$

The z-link term of the Fibonacci fusion surface model (4.39) can be depicted as

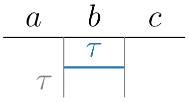

$$= \sum_{b'} \sqrt{\frac{d_{b'}}{d_b d_\tau}}$$

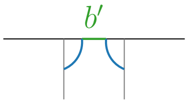

$$= \sum_{b'} [F_a^{b'\tau\tau}]_{b\tau} [F_c^{\tau\tau b}]_{\tau b'} \sqrt{d_\tau} \tag{B.8}$$

Here we denote the degrees of freedom by single arabic letters a, b, …instead of Γ_i, Γ_{ijk} as previously to avoid cluttering notation. Evaluating the above fusion diagram using the F-symbls and R-symbols of the Fibonacci category shows that the z-link term acting on the constrained Hilbert space is equal to

$$H^z = \phi^{1/2} \tilde{n}_a n_b \tilde{n}_c - \phi^{-1/2} (\tilde{n}_a n_b n_c + n_a n_b \tilde{n}_c) + n_a n_c (\sigma_b^x + \phi^{-3/2} n_b). \tag{B.9}$$

Up to an additive and a multiplicative constant, the z-link Hamiltonian (B.9) is the same as the golden chain Hamiltonian [18]. The x-link Hamiltonian can be depicted as

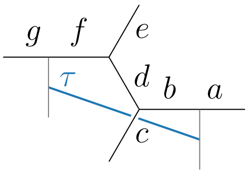

$$= \sum_{b',c',d',f'} \sqrt{\frac{d_{b'} d_{c'} d_{d'} d_{f'}}{d_x^4 d_b d_c d_d d_f}}$$

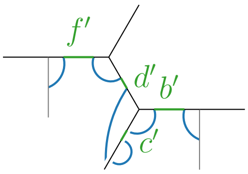

$$= \sum_{b',c',d',f'} (R_{c'}^{c\tau})^* [F_a^{\tau x b}]_{\tau b'} [F_d^{b' x c}]_{b c'} [F_{b'}^{c x d}]_{c' d'} [F_e^{d' x f}]_{d f'} [F_g^{f' x \tau}]_{f \tau} \sqrt{d_\tau}$$

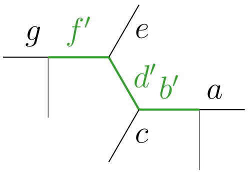

(B.10)

Here the factors from bubble removal essentially cancel the factors from fusing the τ-line to the lattice. The Hamiltonian is diagonal in a, c, e and g, and so decomposes into separate blocks for fixed a, c, e, g. We will use the identities

$$R_1^{\tau\tau} + R_\tau^{\tau\tau} \phi^{-1} = -1, \; R_\tau^{\tau\tau} + R_1^{\tau\tau} \phi^{-1} = R_1^*, \; (R_1 - R_\tau) \phi^{-1} = R_\tau^*.$$

When we fix $c = e = 1$ in (B.10), it is enforced that $b = d = f$ and so we recover the z-link Hamiltonian (B.9).

$$\tilde{n}_c \tilde{n}_e H^x = n_a n_g \left(\sigma_b^x + \phi^{-3/2} n_b \right) + \phi^{1/2} \tilde{n}_a \tilde{n}_g n_b - \phi^{-1/2} \left(\tilde{n}_a n_g + n_a \tilde{n}_g \right) n_b.$$

When $c = 1$ and $e = \tau$ in (B.10), it is enforced that $b = d$, and we get the Hamiltonian

$$\begin{aligned} \tilde{n}_c n_e H^x = &- \phi^{-1/2} \tilde{n}_a \tilde{n}_g n_b n_f + \tilde{n}_a n_g n_b \left(\sigma_f^x + \phi^{-3/2} n_f \right) + n_a \tilde{n}_g n_f \left(\sigma_b^x + \phi^{-3/2} n_b \right) \\ &+ n_a n_g \Big(\phi^{-1/2} \left(\sigma_b^+ \sigma_f^- + \sigma_b^- \sigma_f^+ \right) - \phi^{-1} \left(\sigma_b^x n_f + n_b \sigma_f^x \right) - \phi^{-5/2} n_b n_f \Big) \end{aligned}$$

For $c = \tau$ and $e = 1$, it is enforced that $d = f$, and the Hamiltonian is

$$\begin{aligned} n_c\tilde{n}_e H^x = &- \phi^{-1/2}\tilde{n}_a\tilde{n}_g n_b n_d + \tilde{n}_a n_g \left(R_\tau n_b \sigma_d^+ + R_\tau^* n_b \sigma_d^- + \phi^{-3/2} n_b n_d\right) \\ &+ n_a\tilde{n}_g \left(R_\tau \sigma_b^- n_d + R_\tau^* \sigma_b^+ n_d + \phi^{-3/2} n_b n_d\right) \\ &+ n_a n_g \Big(R_1 \phi^{-1/2} \sigma_b^- \sigma_d^+ + R_1^* \phi^{-1/2} \sigma_b^+ \sigma_d^- - R_\tau^* \phi^{-1}(\sigma_b^+ n_d + n_b \sigma_b^-) \\ &- R_\tau \phi^{-1}(\sigma_b^- n_d + n_b \sigma_d^+) - \phi^{-5/2} n_b n_d\Big). \end{aligned}$$

Lastly, the Hamiltonian for $c = e = \tau$ is

$$\begin{aligned} n_c n_e H = &\tilde{n}_a\tilde{n}_g \left(R_\tau \sigma_d^+ + R_\tau^* \sigma_d^- + \phi^{-3/2} n_d\right) n_b n_f + \tilde{n}_a n_g \Big(R_\tau \phi^{-1/2} n_b \sigma_d^+ \sigma_f^- \\ &+ R_\tau^* \phi^{-1/2} n_b \sigma_d^- \sigma_f^+ - \phi^{-1} n_b n_d \sigma_f^x - \phi^{-5/2} n_b n_d n_f - R_\tau \phi^{-1} \sigma_d^+ n_b n_f - R_\tau^* \phi^{-1} \sigma_d^- n_b n_f\Big) \\ &+ n_a \tilde{n}_g \Big(R_1 \phi^{-1/2} \sigma_b^- \sigma_d^+ n_f + R_1^* \phi^{-1/2} \sigma_b^+ \sigma_d^- n_f - \phi^{-5/2} n_b n_d n_f \\ &- R_\tau \phi^{-1}(\sigma_b^- n_d + n_b \sigma_d^+) n_f - R_\tau^* \phi^{-1}(\sigma_b^+ n_d + n_b \sigma_d^-) n_f\Big) + n_a n_g \Big(R_1^* \phi^{-1} \sigma_b^+ \sigma_d^- \sigma_f^+ \\ &+ R_1 \phi^{-1} \sigma_b^- \sigma_d^+ \sigma_f^- + \phi^{-2} n_b n_d \sigma_f^x + \phi^{-7/2} n_b n_d n_f + R_\tau^* \phi^{-1/2}(\sigma_b^+ \sigma_f^+ + \sigma_b^+ \sigma_f^-) n_d \\ &+ R_\tau \phi^{-1/2}(\sigma_b^- \sigma_f^- + \sigma_b^- \sigma_f^+) n_d + R_\tau^* \phi^{-2}(\sigma_b^+ n_d + n_b \sigma_d^-) n_f \\ &+ R_\tau \phi^{-2}(\sigma_b^- n_d + n_b \sigma_d^+) n_f - R_1^* \phi^{-3/2} \sigma_b^+ \sigma_d^- - R_1 \phi^{-3/2} \sigma_b^- \sigma_d^+ \\ &- R_\tau^* \phi^{-3/2} \sigma_d^- \sigma_f^+ - R_\tau \phi^{-3/2} \sigma_d^+ \sigma_f^-\Big). \end{aligned}$$

It can be checked numerically that the x-link Hamiltonian has the same eigenvalues as the z-link Hamiltonian, but larger degeneracies. Finally, the y-link Hamiltonian is

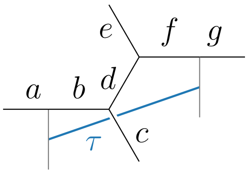

$$= \sum_{b',c',d',f'} \sqrt{\frac{d_{b'} d_{c'} d_{d'} d_{f'}}{d_x^4 d_b d_c d_d d_f}}$$

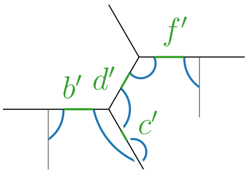

$$= \sum_{b',c',d',f'} (R_{c'}^{ch})^* [F_a^{b'\tau\tau}]_{b\tau} [F_{d'}^{c\tau b}]_{c'b'} [F_b^{d'\tau c}]_{dc'} [F_e^{f'\tau d}]_{fd'} [F_g^{\tau\tau f}]_{\tau f'} \sqrt{d_\tau}$$

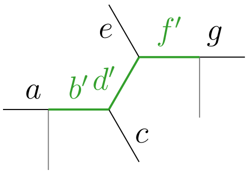

(B.11)

As discussed in Section 4.6, y-link and x-link are related by combined parity symmetry and time-reversal acting as complex conjugation. This implies that the matrix elements of the y-link Hamiltonian are equal to the complex conjugated matrix elements of the x-link Hamiltonian,

$$H^y_{abcdefg} = (H^x_{abcdefg})^*.$$

References

[1] W Lenz. “Beitrag zum Verständnis der magnetischen Erscheinungen in festen Körpern”. In: *Z. Phys.* 21 (1920), pp. 613–615. URL: `https://cds.cern.ch/record/460663`.

[2] E Ising. “Beitrag zur Theorie des Ferromagnetismus”. In: *Z. Phys.* 31 (1925), pp. 253–258. URL: `https://cds.cern.ch/record/429052`.

[3] David Aasen, Paul Fendley, and Roger SK Mong. “Topological defects on the lattice: dualities and degeneracies”. In: *arXiv preprint arXiv:2008.08598* (2020).

[4] H. A. Kramers and G. H. Wannier. “Statistics of the Two-Dimensional Ferromagnet. Part I”. In: *Phys. Rev.* 60 (3 Aug. 1941), pp. 252–262. URL: `https://link.aps.org/doi/10.1103/PhysRev.60.252`.

[5] H. N. V. Temperley, Elliott H Lieb, and Samuel Frederick Edwards. “Relations between the ‘percolation’ and ‘colouring’ problem and other graph-theoretical problems associated with regular planar lattices: some exact results for the ‘percolation’ problem”. In: *Proceedings of the Royal Society of London. A. Mathematical and Physical Sciences* 322.1549 (1971), pp. 251–280. eprint: `https://royalsocietypublishing.org/doi/pdf/10.1098/rspa.1971.0067`.

[6] V. F. R. Jones. “On knot invariants related to some statistical mechanical models”. In: *Pacific J. Math.* 137 (1989), pp. 311–334.

[7] V. F. R. Jones. “Notes on subfactors and statistical mechanics”. In: *Int. J. Mod. Phys. A* 5 (1990), pp. 441–460.

[8] Miki Wadati, Tetsuo Deguchi, and Yasuhiro Akutsu. “Exactly Solvable Models and Knot Theory”. In: *Phys. Rept.* 180 (1989), p. 247.

[9] R J Baxter, S B Kelland, and F Y Wu. “Equivalence of the Potts model or Whitney polynomial with an ice-type model”. In: *Journal of Physics A: Mathematical and General* 9.3 (Mar. 1976), p. 397. URL: `https://dx.doi.org/10.1088/0305-4470/9/3/009`.

[10] G. E. Andrews, R. J. Baxter, and P. J. Forrester. “Eight vertex SOS model and generalized Rogers-Ramanujan type identities”. In: *J. Statist. Phys.* 35 (1984), pp. 193–266.

[11] R. J. Baxter. *Exactly solved models in statistical mechanics.* Academic, 1982.

[12] F. Y. Wu. “Knot theory and statistical mechanics”. In: *Rev. Mod. Phys.* 64 (4 Oct. 1992), pp. 1099–1131. URL: `https://link.aps.org/doi/10.1103/RevModPhys.64.1099`.

[13] Gregory W. Moore and Nathan Seiberg. “Classical and Quantum Conformal Field Theory”. In: *Commun. Math. Phys.* 123 (1989), p. 177.

[14] Roger E. Behrend, Paul A. Pearce, and Jean-Bernard Zuber. “Integrable boundaries, conformal boundary conditions and A-D-E fusion rules”. In: *J. Phys. A* 31 (1998), pp. L763–L770. arXiv: `hep-th/9807142`.

[15] Roger E. Behrend and Paul A. Pearce. “Integrable and conformal boundary conditions for sl(2) A-D-E lattice models and unitary minimal conformal field theories”. In: *J. Statist. Phys.* 102 (2001), p. 577. arXiv: `hep-th/0006094`.

[16] Jurg Frohlich et al. “Duality and defects in rational conformal field theory”. In: *Nucl. Phys. B* 763 (2007), pp. 354–430. arXiv: `hep-th/0607247`.

[17] Jurg Frohlich et al. “Defect Lines, Dualities and Generalised Orbifolds”. In: *16th International Congress on Mathematical Physics.* 2010, pp. 608–613. arXiv: `0909.5013 [math-ph]`.

[18] Adrian Feiguin et al. “Interacting Anyons in Topological Quantum Liquids: The Golden Chain”. In: *Phys. Rev. Lett.* 98 (16 Apr. 2007), p. 160409. URL: `https://link.aps.org/doi/10.1103/PhysRevLett.98.160409`.

[19] Charlotte Gils et al. “Collective States of Interacting Anyons, Edge States, and the Nucleation of Topological Liquids”. In: *Phys. Rev. Lett.* 103 (7 Aug. 2009), p. 070401. URL: `https://link.aps.org/doi/10.1103/PhysRevLett.103.070401`.

[20] C. Gils et al. “Anyonic quantum spin chains: Spin-1 generalizations and topological stability”. In: *Phys. Rev. B* 87.23 (2013), p. 235120. arXiv: `1303.4290 [cond-mat.str-el]`.

[21] Matthew Buican and Andrey Gromov. “Anyonic Chains, Topological Defects, and Conformal Field Theory”. In: *Commun. Math. Phys.* 356.3 (2017), pp. 1017–1056. arXiv: `1701.02800 [hep-th]`.

[22] Kansei Inamura. “On lattice models of gapped phases with fusion category symmetries”. In: *JHEP* 03 (2022), p. 036. arXiv: `2110.12882 [cond-mat.str-el]`.

[23] Laurens Lootens et al. “Dualities in One-Dimensional Quantum Lattice Models: Symmetric Hamiltonians and Matrix Product Operator Intertwiners”. In: *PRX Quantum* 4 (2 June 2023), p. 020357. arXiv: `2112.09091 [quant-ph]`. URL: `https://link.aps.org/doi/10.1103/PRXQuantum.4.020357`.

[24] Laurens Lootens, Clement Delcamp, and Frank Verstraete. “Dualities in One-Dimensional Quantum Lattice Models: Topological Sectors”. In: *PRX Quantum* 5 (1 Mar. 2024), p. 010338. URL: `https://link.aps.org/doi/10.1103/PRXQuantum.5.010338`.

[25] Lakshya Bhardwaj et al. “Categorical Landau Paradigm for Gapped Phases”. In: *Phys. Rev. Lett.* 133 (16 Oct. 2024), p. 161601. URL: `https://link.aps.org/doi/10.1103/PhysRevLett.133.161601`.

[26] Wenjie Ji and Xiao-Gang Wen. “Categorical symmetry and noninvertible anomaly in symmetry-breaking and topological phase transitions”. In: *Phys. Rev. Res.* 2 (3 Sept. 2020), p. 033417. URL: `https://link.aps.org/doi/10.1103/PhysRevResearch.2.033417`.

[27] Lakshya Bhardwaj et al. “Illustrating the categorical Landau paradigm in lattice models”. In: *Phys. Rev. B* 111 (5 Feb. 2025), p. 054432. URL: `https://link.aps.org/doi/10.1103/PhysRevB.111.054432`.

[28] Arkya Chatterjee, Ömer M. Aksoy, and Xiao-Gang Wen. “Quantum phases and transitions in spin chains with non-invertible symmetries”. In: *SciPost Phys.* 17 (2024), p. 115. URL: `https://scipost.org/10.21468/SciPostPhys.17.4.115`.

[29] Paul Fendley, K. Sengupta, and Subir Sachdev. “Competing density-wave orders in a one-dimensional hard-boson model”. In: *Phys. Rev. B* 69 (7 Feb. 2004), p. 075106. URL: `https://link.aps.org/doi/10.1103/PhysRevB.69.075106`.

[30] Christopher J Turner et al. “Weak ergodicity breaking from quantum many-body scars”. In: *Nature Physics* 14.7 (2018), pp. 745–749. arXiv: `1711.03528`.

[31] Igor Lesanovsky and Hosho Katsura. “Interacting Fibonacci anyons in a Rydberg gas”. In: *Phys. Rev. A* 86 (4 Oct. 2012), p. 041601. URL: `https://link.aps.org/doi/10.1103/PhysRevA.86.041601`.

[32] Luisa Eck and Paul Fendley. “From the XXZ chain to the integrable Rydberg-blockade ladder via non-invertible duality defects”. In: *SciPost Phys.* 16 (2024), p. 127. URL: `https://scipost.org/10.21468/SciPostPhys.16.5.127`.

[33] Hannes Bernien et al. “Probing many-body dynamics on a 51-atom quantum simulator”. In: *Nature* 551.7682 (2017), pp. 579–584. arXiv: `1707.04344`.

[34] Giulia Semeghini et al. “Probing topological spin liquids on a programmable quantum simulator”. In: *Science* 374.6572 (2021), p. 1242. arXiv: `2104.04119 [quant-ph]`.

[35] X. G. Wen. “Topological Order in Rigid States”. In: *Int. J. Mod. Phys. B* 4 (1990), p. 239.

[36] Xiao-Gang Wen. “Topological orders and edge excitations in FQH states”. In: *Adv. Phys.* 44.5 (1995), pp. 405–473. arXiv: `cond-mat/9506066`.

[37] Edward Witten. “Quantum Field Theory and the Jones Polynomial”. In: *Commun. Math. Phys.* 121 (1989). Ed. by Asoke N. Mitra, pp. 351–399.

[38] Gregory W. Moore and N. Read. “Nonabelions in the fractional quantum Hall effect”. In: *Nucl. Phys. B* 360 (1991), pp. 362–396.

[39] Alexei Kitaev. “Anyons in an exactly solved model and beyond”. In: *Annals of Physics* 321.1 (2006), pp. 2–111.

[40] D. Arovas, J. R. Schrieffer, and Frank Wilczek. “Fractional Statistics and the Quantum Hall Effect”. In: *Phys. Rev. Lett.* 53 (1984), pp. 722–723.

[41] Xiao-Gang Wen. “Theory of the edge states in fractional quantum Hall effects”. In: *Int. J. Mod. Phys. B* 6 (1992), pp. 1711–1762.

[42] T Yokoi et al. “Half-integer quantized anomalous thermal Hall effect in the Kitaev material candidate α-RuCl3”. In: *Science* 373.6554 (2021), pp. 568–572.

[43] Y Kasahara et al. “Majorana quantization and half-integer thermal quantum Hall effect in a Kitaev spin liquid”. In: *Nature* 559.7713 (2018), pp. 227–231.

[44] Peter Czajka et al. “Planar thermal Hall effect of topological bosons in the Kitaev magnet α-RuCl3”. In: *Nature Materials* 22.1 (Jan. 2023), pp. 36–41. URL: `https://doi.org/10.1038/s41563-022-01397-w`.

[45] Chetan Nayak et al. “Non-Abelian anyons and topological quantum computation”. In: *Reviews of Modern Physics* 80.3 (2008), pp. 1083–1159.

[46] Eric Dennis et al. “Topological quantum memory”. In: *J. Math. Phys.* 43 (2002), pp. 4452–4505. arXiv: `quant-ph/0110143`.

[47] A. Yu. Kitaev. “Fault tolerant quantum computation by anyons”. In: *Annals Phys.* 303 (2003), pp. 2–30. arXiv: `quant-ph/9707021`.

[48] Michael A. Levin and Xiao-Gang Wen. “String-net condensation: A physical mechanism for topological phases”. In: *Phys. Rev. B* 71 (4 Jan. 2005), p. 045110. URL: `https://link.aps.org/doi/10.1103/PhysRevB.71.045110`.

[49] Maissam Barkeshli et al. “Generalized Kitaev Models and Extrinsic Non-Abelian Twist Defects”. In: *Phys. Rev. Lett.* 114 (2 Jan. 2015), p. 026401. URL: `https://link.aps.org/doi/10.1103/PhysRevLett.114.026401`.

[50] Julio C. Magdalena de la Fuente et al. “Topological stabilizer models on continuous variables”. In: (Nov. 2024). arXiv: `2411.04993 [quant-ph]`.

[51] Kansei Inamura and Kantaro Ohmori. “Fusion surface models: 2+ 1d lattice models from fusion 2-categories”. In: *arXiv preprint arXiv:2305.05774* 3 (2023), pp. 33–34.

[52] Maissam Barkeshli et al. “Symmetry fractionalization, defects, and gauging of topological phases”. In: *Phys. Rev. B* 100 (11 Sept. 2019), p. 115147. URL: `https://link.aps.org/doi/10.1103/PhysRevB.100.115147`.

[53] Alexei Kitaev and Liang Kong. “Models for Gapped Boundaries and Domain Walls”. In: *Commun. Math. Phys.* 313.2 (2012), pp. 351–373. arXiv: `1104.5047 [cond-mat.str-el]`.

[54] Tian Lan and Xiao-Gang Wen. “Topological quasiparticles and the holographic bulk-edge relation in $(2+1)$-dimensional string-net models”. In: *Phys. Rev. B* 90 (11 Sept. 2014), p. 115119. URL: `https://link.aps.org/doi/10.1103/PhysRevB.90.115119`.

[55] Chien-Hung Lin and Michael Levin. “Generalizations and limitations of string-net models”. In: *Phys. Rev. B* 89 (19 May 2014), p. 195130. URL: `https://link.aps.org/doi/10.1103/PhysRevB.89.195130`.

[56] Alexander Hahn and Ramona Wolf. “Generalized string-net model for unitary fusion categories without tetrahedral symmetry”. In: *Phys. Rev. B* 102 (11 Sept. 2020), p. 115154. URL: `https://link.aps.org/doi/10.1103/PhysRevB.102.115154`.

[57] Ethan Lake and Yong-Shi Wu. “Signatures of broken parity and time-reversal symmetry in generalized string-net models”. In: *Phys. Rev. B* 94 (11 Sept. 2016), p. 115139. URL: `https://link.aps.org/doi/10.1103/PhysRevB.94.115139`.

[58] Yuting Hu, Spencer D. Stirling, and Yong-Shi Wu. “Ground-state degeneracy in the Levin-Wen model for topological phases”. In: *Phys. Rev. B* 85 (7 Feb. 2012), p. 075107. URL: `https://link.aps.org/doi/10.1103/PhysRevB.85.075107`.

[59] Yuting Hu, Nathan Geer, and Yong-Shi Wu. “Full dyon excitation spectrum in extended Levin-Wen models”. In: *Phys. Rev. B* 97 (19 May 2018), p. 195154. URL: `https://link.aps.org/doi/10.1103/PhysRevB.97.195154`.

[60] Chien-Hung Lin, Michael Levin, and Fiona J Burnell. "Generalized string-net models: A thorough exposition". In: *Physical Review B* 103.19 (2021), p. 195155.

[61] P. I. (Pavel I.) Etingof et al. *Tensor categories*. Mathematical surveys and monographs ; Volume 205. Providence, Rhode Island: American Mathematical Society, 2015.

[62] Peter Huston et al. "Composing topological domain walls and anyon mobility". In: *SciPost Phys.* 15 (2023), p. 076. URL: `https://scipost.org/10.21468/SciPostPhys.15.3.076`.

[63] C. Gils et al. "Anyonic quantum spin chains: Spin-1 generalizations and topological stability". In: *Phys. Rev. B* 87.23 (2013), p. 235120. arXiv: `1303.4290 [cond-mat.str-el]`.

[64] Luisa Eck and Paul Fendley. "From the XXZ chain to the integrable Rydberg-blockade ladder via non-invertible duality defects". In: *SciPost Phys.* 16 (2024), p. 127. URL: `https://scipost.org/10.21468/SciPostPhys.16.5.127`.

[65] Antoine Browaeys and Thierry Lahaye. "Many-body physics with individually controlled Rydberg atoms". In: *Nature Physics* 16.2 (Feb. 2020), pp. 132–142. arXiv: `2002.07413`.

[66] Sepehr Ebadi et al. "Quantum phases of matter on a 256-atom programmable quantum simulator". In: *Nature* 595.7866 (2021), pp. 227–232. arXiv: `2012.12281 [quant-ph]`.

[67] Paul Fendley, K. Sengupta, and Subir Sachdev. "Competing density-wave orders in a one-dimensional hard-boson model". In: *Phys. Rev. B* 69 (7 Feb. 2004), p. 075106. arXiv: `cond-mat/0309438`.

[68] Rhine Samajdar et al. "Numerical study of the chiral Z3 quantum phase transition in one spatial dimension". In: *Phys. Rev. A* 98.2 (2018), p. 023614. arXiv: `1806.01867 [cond-mat.str-el]`.

[69] Natalia Chepiga and Frédéric Mila. "Floating Phase versus Chiral Transition in a 1D Hard-Boson Model". In: *Phys. Rev. Lett.* 122.1 (2019), p. 017205. arXiv: `1808.08990 [cond-mat.str-el]`.

[70] G. Giudici et al. "Diagnosing Potts criticality and two-stage melting in one-dimensional hard-core boson models". In: *Phys. Rev. B* 99 (9 Mar. 2019), p. 094434. arXiv: `1901.10850`.

[71] Xue-Jia Yu et al. "Fidelity susceptibility as a diagnostic of the commensurate-incommensurate transition: A revisit of the programmable Rydberg chain". In: *Phys. Rev. B* 106 (16 Oct. 2022), p. 165124. arXiv: `2207.08337`.

[72] Mikheil Tsitsishvili et al. "Phase diagram of Rydberg-dressed atoms on two-leg square ladders: Coupling supersymmetric conformal field theories on the lattice". In: *Phys. Rev. B* 105.15 (2022), p. 155159. arXiv: `2112.10421 [cond-mat.stat-mech]`.

[73] Pierre Fromholz et al. "Phase diagram of Rydberg-dressed atoms on two-leg triangular ladders". In: *Phys. Rev. B* 106.15 (2022), p. 155411. arXiv: `2207.00385 [cond-mat.stat-mech]`.

[74] Madhumita Sarkar et al. “Quantum order-by-disorder induced phase transition in Rydberg ladders with staggered detuning”. In: *SciPost Phys.* 14 (2023), p. 004. arXiv: `2204.12515`.

[75] Ruben Verresen, Mikhail D. Lukin, and Ashvin Vishwanath. “Prediction of Toric Code Topological Order from Rydberg Blockade”. In: *Phys. Rev. X* 11.3 (2021), p. 031005. arXiv: `2011.12310 [cond-mat.str-el]`.

[76] Kevin Slagle et al. “Quantum spin liquids bootstrapped from Ising criticality in Rydberg arrays”. In: (2022). arXiv: `2204.00013`.

[77] Peter E. Finch. “From spin to anyon notation: The XXZ Heisenberg model as a D(3) (or su(2)(4)) anyon chain”. In: *J. Phys. A* 46 (2013), p. 055305. arXiv: `1201.4470 [math-ph]`.

[78] Natalia Braylovskaya, Peter E. Finch, and Holger Frahm. “Exact solution of the D_3 non-Abelian anyon chain”. In: *Phys. Rev. B* 94.8 (2016), p. 085138. arXiv: `1606.00793 [cond-mat.str-el]`.

[79] Jie Ren. *EDKit.jl*. `https://github.com/jayren3996/EDKit.jl`. 2022.

[80] Ryan Thorngren and Yifan Wang. “Fusion category symmetry. Part II. Categoriosities at c = 1 and beyond”. In: *JHEP* 07 (2024), p. 051. arXiv: `2106.12577 [hep-th]`.

[81] Po-Shen Hsin, Ryohei Kobayashi, and Carolyn Zhang. “Fractionalization of coset non-invertible symmetry and exotic Hall conductance”. In: *SciPost Phys.* 17.3 (2024), p. 095. arXiv: `2405.20401 [cond-mat.str-el]`.

[82] Sahand Seifnashri, Shu-Heng Shao, and Xinping Yang. “Gauging non-invertible symmetries on the lattice”. In: (Mar. 2025). arXiv: `2503.02925 [cond-mat.str-el]`.

[83] Weiguang Cao, Yuan Miao, and Masahito Yamazaki. “Global symmetries of quantum lattice models under non-invertible dualities”. In: (Jan. 2025). arXiv: `2501.12514 [cond-mat.str-el]`.

[84] P. Fendley and P. Ginsparg. “Non-critical orbifolds”. In: *Nuclear Physics B* 324.3 (1989), pp. 549–580. URL: `https://www.sciencedirect.com/science/article/pii/0550321389905208`.

[85] H. W. J. Blöte, John L. Cardy, and M. P. Nightingale. “Conformal invariance, the central charge, and universal finite-size amplitudes at criticality”. In: *Phys. Rev. Lett.* 56 (7 Feb. 1986), pp. 742–745.

[86] Ian Affleck. “Universal term in the free energy at a critical point and the conformal anomaly”. In: *Phys. Rev. Lett.* 56 (7 Feb. 1986), pp. 746–748. URL: `https://link.aps.org/doi/10.1103/PhysRevLett.56.746`.

[87] Matthew Fishman, Steven R. White, and E. Miles Stoudenmire. “The ITensor Software Library for Tensor Network Calculations”. In: *SciPost Phys. Codebases* (2022), p. 4. URL: `https://scipost.org/10.21468/SciPostPhysCodeb.4`.

[88] Lars Onsager. “Crystal statistics. 1. A Two-dimensional model with an order disorder transition”. In: *Phys. Rev.* 65 (1944), pp. 117–149.

[89] Mahito Kohmoto, Marcel den Nijs, and Leo P. Kadanoff. “Hamiltonian studies of the $d = 2$ Ashkin-Teller model”. In: *Phys. Rev. B* 24 (9 Nov. 1981), pp. 5229–5241. URL: `https://link.aps.org/doi/10.1103/PhysRevB.24.5229`.

[90] Pasquale Calabrese and John L. Cardy. "Entanglement entropy and quantum field theory". In: *J. Stat. Mech.* 0406 (2004), P06002. arXiv: `hep-th/0405152`.

[91] Ivo A Maceira, Natalia Chepiga, and Frédéric Mila. "Conformal and chiral phase transitions in Rydberg chains". In: (2022). arXiv: `2203.01163`.

[92] P Peter Stavropoulos, D Pereira, and Hae-Young Kee. "Microscopic mechanism for a higher-spin Kitaev model". In: *Physical review letters* 123.3 (2019), p. 037203.

[93] Kiyu Fukui et al. "Ground-state phase diagram of spin-S Kitaev-Heisenberg models". In: *Phys. Rev. B* 106 (17 Nov. 2022), p. 174416. URL: `https://link.aps.org/doi/10.1103/PhysRevB.106.174416`.

[94] Changsong Xu et al. "Possible Kitaev Quantum Spin Liquid State in 2D Materials with $S = 3/2$". In: *Phys. Rev. Lett.* 124 (8 Feb. 2020), p. 087205. URL: `https://link.aps.org/doi/10.1103/PhysRevLett.124.087205`.

[95] Li-Mei Chen et al. "Chiral spin liquid in a $\mathbb{Z}_3$ Kitaev model". In: *Phys. Rev. B* 109 (15 Apr. 2024), p. 155161. URL: `https://link.aps.org/doi/10.1103/PhysRevB.109.155161`.

[96] Abolhassan Vaezi. "Z_3 generalization of the Kitaev's spin-1/2 model". In: *Phys. Rev. B* 90 (7 Aug. 2014), p. 075106. URL: `https://link.aps.org/doi/10.1103/PhysRevB.90.075106`.

[97] Christopher L. Douglas and David J. Reutter. "Fusion 2-categories and a state-sum invariant for 4-manifolds". In: (Dec. 2018). arXiv: `1812.11933 [math.QA]`.

[98] Davide Gaiotto and Theo Johnson-Freyd. "Condensations in higher categories". In: (May 2019). arXiv: `1905.09566 [math.CT]`.

[99] Wenjie Xi et al. "On a class of fusion 2-category symmetry: condensation completion of braided fusion category". In: (Dec. 2023). arXiv: `2312.15947 [hep-th]`.

[100] Gen Yue, Longye Wang, and Tian Lan. "Condensation Completion and Defects in 2+1D Topological Orders". In: (Feb. 2024). arXiv: `2402.19253 [cond-mat.str-el]`.

[101] Liang Kong et al. "Algebraic higher symmetry and categorical symmetry: A holographic and entanglement view of symmetry". In: *Phys. Rev. Res.* 2 (4 Oct. 2020), p. 043086. URL: `https://link.aps.org/doi/10.1103/PhysRevResearch.2.043086`.

[102] Davide Gaiotto et al. "Generalized global symmetries". In: *Journal of High Energy Physics* 2015.2 (2015), pp. 1–62.

[103] Po-Shen Hsin, Ho Tat Lam, and Nathan Seiberg. "Comments on one-form global symmetries and their gauging in 3d and 4d". In: *SciPost Phys.* 6 (2019), p. 039. URL: `https://scipost.org/10.21468/SciPostPhys.6.3.039`.

[104] Chi-Ming Chang et al. "Topological Defect Lines and Renormalization Group Flows in Two Dimensions". In: *JHEP* 01 (2019), p. 026. arXiv: `1802.04445 [hep-th]`.

[105] Ryan Thorngren and Yifan Wang. "Fusion category symmetry. Part I. Anomaly in-flow and gapped phases". In: *JHEP* 04 (2024), p. 132. arXiv: `1912.02817 [hep-th]`.

[106] Kansei Inamura. *Fusion surface models: 2+1d lattice models from fusion 2-categories.* `https://www.youtube.com/watch?v=6XQ6LWlbpNs&t=35s`. 2023.

[107] Konstantinos Roumpedakis, Sahand Seifnashri, and Shu-Heng Shao. "Higher Gauging and Non-invertible Condensation Defects". In: *Commun. Math. Phys.* 401.3 (2023), pp. 3043–3107. arXiv: `2204.02407 [hep-th]`.

[108] Davide Gaiotto and Theo Johnson-Freyd. "Condensations in higher categories". In: *arXiv preprint arXiv:1905.09566* (2019).

[109] Yichul Choi et al. "Noninvertible duality defects in 3+1 dimensions". In: *Phys. Rev. D* 105.12 (2022), p. 125016. arXiv: `2111.01139 [hep-th]`.

[110] Jeffrey CY Teo and CL Kane. "From Luttinger liquid to non-Abelian quantum Hall states". In: *Physical Review B* 89.8 (2014), p. 085101.

[111] Roger SK Mong et al. "Universal topological quantum computation from a superconductor-abelian quantum hall heterostructure". In: *Physical Review X* 4.1 (2014), p. 011036.

[112] Hong Yao and Steven A Kivelson. "Exact chiral spin liquid with non-abelian anyons". In: *Physical review letters* 99.24 (2007), p. 247203.

[113] H. Bombin. "Topological Order with a Twist: Ising Anyons from an Abelian Model". In: *Phys. Rev. Lett.* 105 (3 July 2010), p. 030403. URL: `https://link.aps.org/doi/10.1103/PhysRevLett.105.030403`.

[114] Olga Petrova, Paula Mellado, and Oleg Tchernyshyov. "Unpaired Majorana modes in the gapped phase of Kitaev's honeycomb model". In: *Phys. Rev. B* 88 (14 Oct. 2013), p. 140405. URL: `https://link.aps.org/doi/10.1103/PhysRevB.88.140405`.

[115] Olga Petrova, Paula Mellado, and Oleg Tchernyshyov. "Unpaired Majorana modes on dislocations and string defects in Kitaev's honeycomb model". In: *Phys. Rev. B* 90 (13 Oct. 2014), p. 134404. URL: `https://link.aps.org/doi/10.1103/PhysRevB.90.134404`.

[116] Yi-Zhuang You and Xiao-Gang Wen. "Projective non-Abelian statistics of dislocation defects in a ZN rotor model". In: *Physical Review B—Condensed Matter and Materials Physics* 86.16 (2012), p. 161107.

[117] Huaixiu Zheng, Arpit Dua, and Liang Jiang. "Demonstrating non-Abelian statistics of Majorana fermions using twist defects". In: *Phys. Rev. B* 92 (24 Dec. 2015), p. 245139. URL: `https://link.aps.org/doi/10.1103/PhysRevB.92.245139`.

[118] Daisuke Tambara and Shigeru Yamagami. "Tensor Categories with Fusion Rules of Self-Duality for Finite Abelian Groups". In: *Journal of Algebra* 209.2 (1998), pp. 692–707. URL: `https://www.sciencedirect.com/science/article/pii/S0021869398975585`.

[119] Pavel Etingof, Dmitri Nikshych, and Victor Ostrik. "Fusion categories and homotopy theory". In: *Quantum topology* 1.3 (2010), pp. 209–273.

[120] César Galindo. "Trivializing group actions on braided crossed tensor categories and graded braided tensor categories". In: *Journal of the Mathematical Society of Japan* 74.3 (2022), pp. 735–752.

[121] Tyler D Ellison et al. "Pauli topological subsystem codes from Abelian anyon theories". In: *Quantum* 7 (2023), p. 1137.

[122] Ruizhi Liu et al. "Symmetries and anomalies of Kitaev spin-S models: Identifying symmetry-enforced exotic quantum matter". In: *SciPost Phys.* 16.4 (2024), p. 100. arXiv: `2310.16839 [cond-mat.str-el]`.

[123] Kyle Kawagoe and Michael Levin. "Microscopic definitions of anyon data". In: *Physical Review B* 101.11 (2020), p. 115113.

[124] Ji-Yao Chen et al. "Simulating Bulk Gap in Chiral Projected Entangled-Pair States". In: (Feb. 2025). arXiv: `2502.20142 [cond-mat.str-el]`.

[125] Xiaoliang Qi. *A $\mathbb{Z}_N$ generalization of Kitaev's honeycomb model.* `https://scgp.stonybrook.edu/video_portal/video.php?id=732`. Simons Center for Geometry and Physics, 2013.

[126] Paul Fendley. "Integrability and braided tensor categories". In: *Journal of Statistical Physics* 182.2 (2021), p. 43.

[127] Denis Bernard and Giovanni Felder. "Quantum group symmetries in 2-D lattice quantum field theory". In: *Nucl. Phys. B* 365 (1991), pp. 98–120.

[128] Yacine Ikhlef and Robert Weston. "Discrete holomorphicity in the chiral Potts model". In: *Journal of Physics A: Mathematical and Theoretical* 48.29 (2015), p. 294001.

[129] Yacine Ikhlef and John Cardy. "Discretely holomorphic parafermions and integrable loop models". In: *Journal of Physics A: Mathematical and Theoretical* 42.10 (2009), p. 102001.

[130] Roger S. K. Mong et al. "Parafermionic conformal field theory on the lattice". In: *J. Phys. A* 47.45 (2014), p. 452001. arXiv: `1406.0846 [cond-mat.stat-mech]`.

[131] EM Stoudenmire et al. "Assembling Fibonacci anyons from a Z 3 parafermion lattice model". In: *Physical Review B* 91.23 (2015), p. 235112.

[132] Hui Li and F. D. M. Haldane. "Entanglement Spectrum as a Generalization of Entanglement Entropy: Identification of Topological Order in Non-Abelian Fractional Quantum Hall Effect States". In: *Phys. Rev. Lett.* 101 (1 July 2008), p. 010504. URL: `https://link.aps.org/doi/10.1103/PhysRevLett.101.010504`.

[133] L. Cincio and G. Vidal. "Characterizing Topological Order by Studying the Ground States on an Infinite Cylinder". In: *Phys. Rev. Lett.* 110 (6 Feb. 2013), p. 067208. URL: `https://link.aps.org/doi/10.1103/PhysRevLett.110.067208`.

[134] Johannes Hauschild and Frank Pollmann. "Efficient numerical simulations with tensor networks: Tensor Network Python (TeNPy)". In: *SciPost Physics Lecture Notes* (2018), p. 005.

[135] Johannes Hauschild et al. "Tensor network Python (TeNPy) version 1". In: *SciPost Phys. Codebases* (2024), p. 41. URL: `https://scipost.org/10.21468/SciPostPhysCodeb.41`.

[136] Kazuya Shinjo, Shigetoshi Sota, and Takami Tohyama. “Density-matrix renormalization group study of the extended Kitaev-Heisenberg model”. In: *Phys. Rev. B* 91 (5 Feb. 2015), p. 054401. URL: `https://link.aps.org/doi/10.1103/PhysRevB.91.054401`.

[137] Lukasz Fidkowski et al. “From string nets to nonabelions”. In: *Communications in Mathematical Physics* 287 (2009), pp. 805–827.

[138] Charlotte Gils et al. “Topology-driven quantum phase transitions in time-reversal-invariant anyonic quantum liquids”. In: *Nature Physics* 5.11 (2009), pp. 834–839.

[139] Marc Daniel Schulz et al. “Topological phase transitions in the golden string-net model”. In: *Physical review letters* 110.14 (2013), p. 147203.

[140] R. J. Baxter. “Rogers-Ramanujan identities in the hard hexagon model”. In: *Journal of Statistical Physics* 26.3 (Nov. 1981), pp. 427–452. URL: `https://doi.org/10.1007/BF01011427`.

[141] R J Baxter and P A Pearce. “Hard squares with diagonal attractions”. In: *Journal of Physics A: Mathematical and General* 16.10 (July 1983), p. 2239. URL: `https://dx.doi.org/10.1088/0305-4470/16/10/022`.

[142] Markus Hauru et al. “Topological conformal defects with tensor networks”. In: *Phys. Rev. B* 94 (11 Sept. 2016), p. 115125. URL: `https://link.aps.org/doi/10.1103/PhysRevB.94.115125`.

[143] Laurens Lootens et al. “Matrix product operator symmetries and intertwiners in string-nets with domain walls”. In: *SciPost Phys.* 10 (2021), p. 053. URL: `https://scipost.org/10.21468/SciPostPhys.10.3.053`.

[144] D A Huse. “Multicritical scaling in Baxter’s hard square lattice gas”. In: *Journal of Physics A: Mathematical and General* 16.18 (Dec. 1983), p. 4357. URL: `https://dx.doi.org/10.1088/0305-4470/16/18/035`.

[145] Didier Poilblanc et al. “Quantum spin ladders of non-Abelian anyons”. In: *Phys. Rev. B* 83 (13 Apr. 2011), p. 134439. URL: `https://link.aps.org/doi/10.1103/PhysRevB.83.134439`.

[146] Andreas WW Ludwig et al. “Two-dimensional quantum liquids from interacting non-Abelian anyons”. In: *New Journal of Physics* 13.4 (2011), p. 045014.

[147] Michael Lassig, Giuseppe Mussardo, and John L. Cardy. “The scaling region of the tricritical Ising model in two-dimensions”. In: *Nucl. Phys. B* 348 (1991), pp. 591–618.

[148] Tarun Grover, D. N. Sheng, and Ashvin Vishwanath. “Emergent Space-Time Supersymmetry at the Boundary of a Topological Phase”. In: *Science* 344.6181 (2014), pp. 280–283. arXiv: `1301.7449 [cond-mat.str-el]`.

[149] Chengshu Li et al. “Coupled wire construction of a topological phase with chiral tricritical Ising edge modes”. In: *Phys. Rev. B* 102 (16 Oct. 2020), p. 165123. URL: `https://link.aps.org/doi/10.1103/PhysRevB.102.165123`.

[150] Phillip Weinberg and Marin Bukov. “QuSpin: a Python package for dynamics and exact diagonalisation of quantum many body systems part I: spin chains”. In: *SciPost Phys.* 2 (2017), p. 003. URL: `https://scipost.org/10.21468/SciPostPhys.2.1.003`.

[151] Denis Bernard and Giovanni Felder. "Quantum group symmetries in two-dimensional lattice quantum field theory". In: *Nuclear Physics B* 365.1 (1991), pp. 98–120. URL: `https://www.sciencedirect.com/science/article/pii/055032139190608Z`.

[152] Seung-Moon Hong, Eric Rowell, and Zhenghan Wang. "On exotic modular tensor categories". In: *Communications in Contemporary Mathematics* 10.supp01 (2008), pp. 1049–1074.

[153] Weiguang Cao, Yuan Miao, and Masahito Yamazaki. "Global symmetries of quantum lattice models under non-invertible dualities". In: (Jan. 2025). arXiv: `2501.12514 [cond-mat.str-el]`.

[154] Salvatore D. Pace et al. "Gauging modulated symmetries: Kramers-Wannier dualities and non-invertible reflections". In: *SciPost Phys.* 18 (2025), p. 021. URL: `https://scipost.org/10.21468/SciPostPhys.18.1.021`.

[155] Clement Delcamp and Apoorv Tiwari. "Higher categorical symmetries and gauging in two-dimensional spin systems". In: *SciPost Phys.* 16 (2024), p. 110. URL: `https://scipost.org/10.21468/SciPostPhys.16.4.110`.

[156] Jutho Haegeman et al. "Gauging quantum states: from global to local symmetries in many-body systems". In: *Phys. Rev. X* 5.1 (2015), p. 011024. arXiv: `1407.1025 [quant-ph]`.

[157] Yichul Choi et al. "Non-invertible and higher-form symmetries in 2+1d lattice gauge theories". In: *SciPost Phys.* 18.1 (2025), p. 008. arXiv: `2405.13105 [cond-mat.str-el]`.

[158] Kansei Inamura et al. "(2+1)d Lattice Models and Tensor Networks for Gapped Phases with Categorical Symmetry". In: (June 2025). arXiv: `2506.09177 [cond-mat.str-el]`.

[159] Henriques, André and Penneys, David and Tener, James. "Categorified trace for module tensor categories over braided tensor categories". In: *Documenta Mathematica* 21.2016 (2016). arXiv: `1509.02937 [math.QA]`.

[160] JB Fouet, P Sindzingre, and C Lhuillier. "An investigation of the quantum J 1-J 2-J 3 model on the honeycomb lattice". In: *The European Physical Journal B-Condensed Matter and Complex Systems* 20 (2001), pp. 241–254. eprint: `0101421`.

[161] A. F. Albuquerque et al. "Phase diagram of a frustrated quantum antiferromagnet on the honeycomb lattice: Magnetic order versus valence-bond crystal formation". In: *Phys. Rev. B* 84 (2 July 2011), p. 024406. URL: `https://link.aps.org/doi/10.1103/PhysRevB.84.024406`.

[162] P. H. Y. Li et al. "Phase diagram of a frustrated Heisenberg antiferromagnet on the honeycomb lattice: The J_1-J_2-J_3 model". In: *Phys. Rev. B* 86 (14 Oct. 2012), p. 144404. URL: `https://link.aps.org/doi/10.1103/PhysRevB.86.144404`.

[163] Shou-Shu Gong et al. "Phase diagram of the spin-$\frac{1}{2}$ J_1-J_2 Heisenberg model on a honeycomb lattice". In: *Phys. Rev. B* 88 (16 Oct. 2013), p. 165138. URL: `https://link.aps.org/doi/10.1103/PhysRevB.88.165138`.

[164] Kenn Kubo and Tatsuya Kishi. “Existence of Long-Range Order in the XXZ Model”. In: *Phys. Rev. Lett.* 61 (22 Nov. 1988), pp. 2585–2587. URL: `https://link.aps.org/doi/10.1103/PhysRevLett.61.2585`.

[165] Tom Kennedy, Elliott H. Lieb, and B. Sriram Shastry. “The XY Model Has Long-Range Order for All Spins and All Dimensions Greater than One”. In: *Phys. Rev. Lett.* 61 (22 Nov. 1988), pp. 2582–2584. URL: `https://link.aps.org/doi/10.1103/PhysRevLett.61.2582`.

[166] V. S. Viswanath et al. “Ordering and fluctuations in the ground state of the one-dimensional and two-dimensional S=1/2 XXZ antiferromagnets: A study of dynamical properties based on the recursion method”. In: *Phys. Rev. B* 49 (14 Apr. 1994), pp. 9702–9715. URL: `https://link.aps.org/doi/10.1103/PhysRevB.49.9702`.

[167] Zheng Weihong, J. Oitmaa, and C. J. Hamer. “Second-order spin-wave results for the quantum XXZ and XY models with anisotropy”. In: *Phys. Rev. B* 44 (21 Dec. 1991), pp. 11869–11881. URL: `https://link.aps.org/doi/10.1103/PhysRevB.44.11869`.

[168] Masahiro Kadosawa et al. “Comparing quantum fluctuations in the spin-$\frac{1}{2}$ and spin-1 XXZ Heisenberg models on the square and honeycomb lattices”. In: *Phys. Rev. B* 110 (13 Oct. 2024), p. 134418. URL: `https://link.aps.org/doi/10.1103/PhysRevB.110.134418`.

[169] Sahar Satoori, Saeed Mahdavifar, and Javad Vahedi. “Entanglement and quantum correlations in the XX spin-1/2 honeycomb lattice”. In: *Sci. Rep.* 12.1 (2022), p. 17991. arXiv: `2204.07708 [cond-mat.str-el]`.

[170] Luisa Eck and Paul Fendley. “Generalizations of Kitaev’s honeycomb model from braided fusion categories”. In: *SciPost Phys.* 18 (2025), p. 170. URL: `https://scipost.org/10.21468/SciPostPhys.18.6.170`.

[171] Kyusung Hwang. “Anyon condensation and confinement transition in a Kitaev spin liquid bilayer”. In: *Phys. Rev. B* 109.13 (2024), p. 134412. arXiv: `2301.05721 [cond-mat.str-el]`.

[172] G. Misguich, D. Serban, and V. Pasquier. “Quantum dimer model with extensive ground-state entropy on the kagome lattice”. In: *Phys. Rev. B* 67 (21 June 2003), p. 214413. URL: `https://link.aps.org/doi/10.1103/PhysRevB.67.214413`.

[173] F. J. Burnell, Steven H. Simon, and J. K. Slingerland. “Condensation of achiral simple currents in topological lattice models: Hamiltonian study of topological symmetry breaking”. In: *Phys. Rev. B* 84 (12 Sept. 2011), p. 125434. URL: `https://link.aps.org/doi/10.1103/PhysRevB.84.125434`.

[174] F J Burnell, Steven H Simon, and J K Slingerland. “Phase transitions in topological lattice models via topological symmetry breaking”. In: *New Journal of Physics* 14.1 (Jan. 2012), p. 015004. URL: `https://dx.doi.org/10.1088/1367-2630/14/1/015004`.

[175] R. Wiedmann et al. “Quantum critical phase transition between two topologically-ordered phases in the Ising toric code bilayer”. In: *Phys. Rev. B* 102.21 (2020), p. 214422. arXiv: `2010.05982 [cond-mat.str-el]`.

[176] Ken Kikuchi. “Classification of connected étale algebras in multiplicity-free modular fusion categories up to rank nine”. In: (Apr. 2024). arXiv: `2404.16125 [math.QA]`.

[177] Xiao-Gang Wen. “Quantum Orders in an Exact Soluble Model”. In: *Phys. Rev. Lett.* 90 (1 Jan. 2003), p. 016803. URL: `https://link.aps.org/doi/10.1103/PhysRevLett.90.016803`.

[178] Chris Heinrich et al. “Symmetry-enriched string nets: Exactly solvable models for SET phases”. In: *Phys. Rev. B* 94 (23 Dec. 2016), p. 235136. URL: `https://link.aps.org/doi/10.1103/PhysRevB.94.235136`.

[179] Meng Cheng et al. “Exactly solvable models for symmetry-enriched topological phases”. In: *Phys. Rev. B* 96 (11 Sept. 2017), p. 115107. URL: `https://link.aps.org/doi/10.1103/PhysRevB.96.115107`.

[180] Liang Kong and Hao Zheng. “The center functor is fully faithful”. In: *Advances in Mathematics* 339 (2018), pp. 749–779. arXiv: `1507.00503 [math.QA]`.

[181] Adrien Brochier, David Jordan, and Noah Snyder. “On dualizability of braided tensor categories”. In: *Compos. Math.* 157.3 (2021), pp. 435–483. arXiv: `1804.07538 [math.QA]`.

[182] Scott Morrison, David Penneys, and Julia Plavnik. “Completion for braided enriched monoidal categories”. In: (2018). eprint: `1809.09782`.

[183] Scott Morrison and David Penneys. “Monoidal categories enriched in braided monoidal categories”. In: *International Mathematics Research Notices* 2019.11 (2019), pp. 3527–3579. eprint: `1701.00567`.

[184] Jacob C. Bridgeman, Benjamin J. Brown, and Samuel J. Elman. “Boundary Topological Entanglement Entropy in Two and Three Dimensions”. In: *Commun. Math. Phys.* 389.2 (2022), pp. 1241–1276. arXiv: `2012.05244 [quant-ph]`.

[185] FJ Burnell, CW Von Keyserlingk, and SH Simon. “Phase transitions in three-dimensional topological lattice models with surface anyons”. In: *Physical Review B—Condensed Matter and Materials Physics* 88.23 (2013), p. 235120.

[186] David Green et al. “Enriched string-net models and their excitations”. In: *Quantum* 8 (Mar. 2024), p. 1301. URL: `https://doi.org/10.22331/q-2024-03-28-1301`.

[187] Vincentas Mulevičius and Ingo Runkel. “Constructing modular categories from orbifold data”. In: *Quantum Topol.* 13.3 (2023), pp. 459–523. arXiv: `2002.00663 [math.QA]`.

[188] Vincentas Mulevicius and Ingo Runkel. “Fibonacci-type orbifold data in Ising modular categories”. In: *J. Pure Appl. Algebra* 227 (2023), p. 107301. arXiv: `2010.00932 [math.QA]`.

[189] Vincentas Mulevičius, Ingo Runkel, and Thomas Voß. “Internal Levin-Wen models”. In: *SciPost Phys.* 17 (2024), p. 088. URL: `https://scipost.org/10.21468/SciPostPhys.17.3.088`.

[190] Ken Kikuchi. “Classification of connected étale algebras in pre-modular fusion categories up to rank three”. In: (Nov. 2023). arXiv: `2311.15631 [math.QA]`.

[191] Ken Kikuchi. “Classification of connected étale algebras in modular fusion categories up to rank five”. In: (Dec. 2023). arXiv: `2312.13353 [math.QA]`.

[192] Ken Kikuchi, Kah-Sen Kam, and Fu-Hsiang Huang. “Classification of connected étale algebras in multiplicity-free modular fusion categories at rank six”. In: (Feb. 2024). arXiv: `2402.00403 [math.QA]`.

[193] Kansei Inamura. “Symmetry of the dual fusion surface model”. unpublished notes, private communications. 2024.

[194] Thibault D Décoppet. “Drinfeld centers and Morita equivalence classes of fusion 2-categories”. In: (2022). arXiv: `2211.04917 [math.CT]`.

[195] Thibault D Décoppet. “The Morita theory of fusion 2-categories”. In: (2022). arXiv: `2208.08722 [math.CT]`.

[196] Christopher Douglas, Christopher Schommer-Pries, and Noah Snyder. *Dualizable tensor categories*. Vol. 268. 1308. American Mathematical Society, 2020. eprint: `1312.7188`.

[197] Robert Laugwitz. “The relative monoidal center and tensor products of monoidal categories”. In: *Communications in Contemporary Mathematics* 22.08 (2020), p. 1950068. eprint: `1803.04403`.

[198] Michael Müger. “On the Structure of Modular Categories”. In: *Proceedings of the London Mathematical Society* 87.2 (2003), pp. 291–308. eprint: `0201017`.

[199] C. J. Turner et al. “Quantum scarred eigenstates in a Rydberg atom chain: Entanglement, breakdown of thermalization, and stability to perturbations”. In: *Phys. Rev. B* 98 (15 Oct. 2018), p. 155134. URL: `https://link.aps.org/doi/10.1103/PhysRevB.98.155134`.

[200] Paul Niklas Jepsen et al. “Long-lived phantom helix states in Heisenberg quantum magnets”. In: *Nature Phys.* 18.8 (2022), pp. 899–904. arXiv: `2110.12043 [cond-mat.quant-gas]`.

[201] Paul A McClarty et al. “Disorder-free localization and many-body quantum scars from magnetic frustration”. In: *Physical Review B* 102.22 (2020), p. 224303.

[202] Felix Gerken et al. “All product eigenstates in Heisenberg models from a graphical construction”. In: *Phys. Rev. Res.* 7.1 (2025), p. L012008. arXiv: `2310.13158 [cond-mat.str-el]`.

[203] Yuan Miao et al. “Exact Quantum Many-Body Scars in 2D Quantum Gauge Models”. In: (May 2025). arXiv: `2505.21921 [cond-mat.str-el]`.

[204] Bram Vancraeynest-De Cuiper and Clement Delcamp. “Twisted gauging and topological sectors in (2+1)d abelian lattice gauge theories”. In: (Jan. 2025). arXiv: `2501.16301 [cond-mat.str-el]`.

[205] Thibault D. Décoppet and Matthew Yu. “Fiber 2-Functors and Tambara–Yamagami Fusion 2-Categories”. In: *Commun. Math. Phys.* 406.3 (2025), p. 64. arXiv: `2306.08117 [math.CT]`.

[206] Shawn Xingshan Cui, Modjtaba Shokrian Zini, and Zhenghan Wang. “On generalized symmetries and structure of modular categories”. In: *Science China Mathematics* 62 (2019), pp. 417–446.

[207] Vincentas Mulevicius. “Condensation inversion and Witt equivalence via generalised orbifolds”. In: *arXiv preprint arXiv:2206.02611* (2022).

[208] David Aasen, Zhenghan Wang, and Matthew B. Hastings. “Adiabatic paths of Hamiltonians, symmetries of topological order, and automorphism codes”. In: *Phys. Rev. B* 106.8 (2022), p. 085122. arXiv: `2203.11137 [quant-ph]`.

[209] Matthew B. Hastings and Jeongwan Haah. “Dynamically Generated Logical Qubits”. In: *Quantum* 5 (2021), p. 564. arXiv: `2107.02194 [quant-ph]`.

[210] Michael Kamfor et al. “Kitaev model and dimer coverings on the honeycomb lattice”. In: *J. Stat. Mech.* 1008 (2010), P08010. arXiv: `1005.5103 [cond-mat.other]`.

[211] Eoin Quinn, Subhro Bhattacharjee, and Roderich Moessner. “Phases and phase transitions of a perturbed Kekulé-Kitaev model”. In: *Physical Review B* 91.13 (2015), p. 134419.

[212] Sheng-Jie Huang and Yanzhu Chen. “Generating logical magic states with the aid of non-Abelian topological order”. In: (Feb. 2025). arXiv: `2502.00998 [quant-ph]`.

[213] Margarita Davydova et al. “Universal fault tolerant quantum computation in 2D without getting tied in knots”. In: (Mar. 2025). arXiv: `2503.15751 [quant-ph]`.

[214] Sung-Kil Yang. “Modular Invariant Partition Function of the Ashkin-teller Model on the Critical Line and $N = 2$ Superconformal Invariance”. In: *Nucl. Phys. B* 285 (1987), p. 183.

[215] Rui-Zhen Huang et al. “Emergent Conformal Boundaries from Finite-Entanglement Scaling in Matrix Product States”. In: *Phys. Rev. Lett.* 132 (8 Feb. 2024), p. 086503. URL: `https://link.aps.org/doi/10.1103/PhysRevLett.132.086503`.